THESIS FOR THE DEGREE OF LICENTIATE OF ENGINEERING

Modeling of a 4kW Axial Flux Machine - Measurements and 2D/3D Modeling

Considering the impact of end leakage flux

Vineetha Puttaraj

Department of Electrical Engineering
Chalmers University of Technology
Gothenburg, Sweden, 2025

Modeling of a 4kW Axial Flux Machine - Measurements and 2D/3D Modeling

Considering the impact of end leakage flux

Vineetha Puttaraj

Licentiate Thesis at Chalmers University of Technology

Department of Electrical Engineering
Chalmers University of Technology
SE-412 96 Gothenburg, Sweden
Phone: +46 (0)31 772 1000

Printed by Chalmers Reproservice
Gothenburg, Sweden, January 2025

To Ullas, Yaduveer and Yuvika.

Modeling of a 4kW Axial Flux Machine - Measurements and 2D/3D Modeling

Considering the impact of end leakage flux

Vineetha Puttaraj
Department of Electrical Engineering
Chalmers University of Technology

Abstract

Axial Flux Machines (AFMs) are emerging as a promising alternative to traditional Radial Flux Machines (RFMs) offering advantages in power density, compactness, and efficiency, especially for Electric Vehicles and other high-performance applications. This study investigates the modeling and analysis of AFMs using both Three-Dimensional (3D) and Two-Dimensional (2D) simulation approaches. A physical AFM was investigated and modeled with the 3D Finite Element Method (FEM), establishing a benchmark for accurate electromagnetic analysis. The 3D model was parameterized and transformed into an equivalent 2D model, with an extruded 2D model developed to enhance the comparison between the two approaches. A key focus of this work is the analysis of end leakage flux and end-turn leakage inductance, with results quantifying the 2D models' computational efficiency versus their inability to capture the edge effects that are accurately represented in the much more time-demanding 3D models.

The study found that a medium mesh density and 120 time-steps per electrical period of the fundamental voltage provide an ideal compromise between computational accuracy and efficiency. Although the 2D model cannot fully replicate the geometric complexities of the 3D model, it proves to be an effective approximation in specific applications where detailed edge effects are less critical. Several 3D and 2D models with varying core and magnet lengths were compared. Furthermore, a narrow core and magnet length model was analyzed across five sizes from full 3D to 2D. Results indicate that rotor magnet leakage becomes significant, necessitating a 3D model when a magnetically leading rotor core surrounds the magnets in the radial direction. Similarly, winding end leakage effects require 3D modeling when the stator core's radial thickness is small compared to the extent of the coil ends. For the investigated

double stator single rotor machine, the recommended ratio of the length of the magnet in the radial direction to the radius of the computational plane should be greater than 0.5. Further, it is found with FEM that the end-turn leakage inductances in the d- and q-directions are 33% and 25% of the total d- and q-axis inductance, respectively. The 11% difference of power between 3D and 2D at higher speeds is due to the leakage inductance. Two analytical methods suggested in literature for calculation of end-turn leakage inductance, one for RFMs, and one for AFMs are modified and analyzed. It is found that both methods fail to capture the end-turn inductance well, with the best guess yielding a 60% lower value compared to FEM simulations.

This work advances modeling methodologies for AFMs by offering insights into refining mesh density and time-steps, identifying the limitations of 2D models, and offering detailed insights into electromagnetic phenomena like end leakage flux. Failing to refine the mesh density and time-steps can result in reduced precision of simulation results in key parameters, such as flux density and torque, and may fail to capture critical phenomena like end leakage flux. The findings contribute to improving AFM design and simulation techniques, identifying areas for further enhancement in 2D modeling to balance computational efficiency and accuracy.

Keywords: Axial Flux Machines, Axial Flux Permanent Magnet Machine, Double Stator Single Rotor, Finite Element Method, 3D modeling, 2D modeling, Linear Machine Modeling Approach, End Leakage Flux, End-Turn Leakage Inductance

List of Publications

[1] **Vineetha Puttaraj**, Sonja Lundmark, Torbjörn Thiringer. "Moving from a 3D Axial Flux Machine Model to 2D Considering the Impact of End Leakage Flux", *Published in International Conference on Electrical Machines (ICEM)*, 2024.

[2] **Vineetha Puttaraj**, Sonja Lundmark, Torbjörn Thiringer. "Evaluation of Efficient 2D Axial Flux Motor Models with End Turn Leakage Inductance Consideration", submitted to *IET special issue on Opportunities and Challenges in Design and Optimisation of Axial-Flux Electric Machines*.

Acknowledgments

First and foremost, I would like to express my deepest gratitude to my main supervisor Associate Prof. Sonja Lundmark, my examiner Prof. Torbjörn Thiringer, and my co-supervisor Dr. Emma Grunditz, for their invaluable guidance, encouragement, and unwavering support. Your expertise and insightful feedback have been pivotal to the success of this work.

I would also like to extend my sincere thanks to Dr. Mikael Alatalo for the collaborative support, valuable insights, and assistance. I would also like to thank Xiaoliang Huang for his unwavering support in capturing the measurements.

I am particularly grateful to the Swedish Electromobility Center for providing the financial support that made the research possible. I extend my heartfelt gratitude to Chalmerska forskningsfonden and the K. G. Hallby's Fund for generously awarding me travel scholarships, which enabled me to attend conferences and summer schools abroad.

I would like to express my gratitude to VCC for providing the three axial flux machines and for their efforts in facilitating the disassembly process. I would also like to thank Dana Mezher for her valuable cooperation during her Master thesis work.

Finally, I owe my deepest gratitude to my husband, Ullas, and my parents for their unwavering love, support, and encouragement. I would like to thank my kids Yaduveer and Yuvika for being so cooperative. A special thanks to all my colleagues and friends at Chalmers. I would like to extend special thanks to colleagues in the reference group for being helpful and supportive.

Acronyms

2D	Two-Dimensional
3D	Three-Dimensional
AFM	Axial Flux Machine
AFPM	Axial Flux Permanent Magnet
AM	Additive Manufacturing
CW	Concentrated Winding
DRSS	Double Rotor Single Stator
DSSR	Double Stator Single Rotor
DW	Distributed Winding
EV	Electric Vehicle
FEA	Finite Element Analysis
FEM	Finite Element Method
ICEV	Internal Combustion Engine Vehicle
IRMA	Inner Rotor Modeling Approach
LMMA	Linear Machine Modeling Approach
ORMA	Outer Rotor Modeling Approach
PM	Permanent Magnet
RFM	Radial Flux Machine
SMC	Soft Magnetic Composite
SSSR	Single Stator Single Rotor
YASA	Yokeless And Segmented Armature

Mathematical symbols

A_c	Cross-section area of coil
A_s	Slot area
$A_{cu,w}$	Area of copper per layer per slot
A_{cu}	Area of copper in slot
$Bs0$	Stator slot opening width
C_s	Number of coils per slot
C_{ph}	Number of coils per phase
D_{is}	Inner stator diameter
FT_1	Half of the frame thickness
$Hs0$	Height of slot opening
$Hs2$	Slot height
ID_{mag}	Inner diameter of the magnet
ID_{rotor}	Inner diameter of the rotor core
K_M	Mutual phase cross coupling factor
K_P	End region permeable support factor
L	Overall length of the machine
L_1	Length of hollow section in half of the machine frame
L_2	Length excluding frame thickness on half of the machine
L_G	Total airgap in the machine
L_c	Average length of coil
L_{mag}	Length of the magnet in x-direction

L_{sc}	Length of single strand
L_{tooth}	Length of the stator tooth in x-direction
N_c	Number of coils per phase
N_l	Number of winding layers
N_p	Number of parallel branches
N_t	Number of turns in each layer
$N_{c,strand}$	Number of copper strands in each layer
N_{cc}	Number of conductors per coil
N_{strand}	Number of copper strands
OD_{mag}	Outer diameter of the magnet
OD_{rotor}	Outer diameter of the rotor core
PM_{th}	Magnet thickness
Q_s	Number of stator slots
RT	Rotor thickness
R_s	Stator winding resistance per phase
R_{DC}	DC Resistance
$R_{s(dc)}$	Measured DC resistance
R_{sc}	Resistance of single coil
R_{wp}	Radius of the workplane
ST_1	Stator thickness per stator
S_s	Number of slots per pole
S_α	Angle near the slot opening
S_{ph}	Number of slots per phase
T_{ph}	Turns per phase in series

Th_{magnet}	Thickness of the magnet
V_{cu}	Volume of the copper per coil
W_c	Width of coil
W_t	Average tooth width
$W_{mag,core}$	Core spacing between the magnets
W_{ss}	Width of stator slot
Z	Total number of conductors
Z_{agj}	Extra length in z-direction for geometrical intersection
ρ	Resistivity of the coil
ρ_{cu}	Resistivity of the copper at 20^oC
a_{cond}	Cross-section area of the coil (Analytical)
d_s	Depth of stator core
d_{ss}	Depth of stator slot
d_{strand}	Diameter of the copper strand
d_{sy}	Depth of stator yoke
h_c	Height of the coil
k_{slot}	Slot fill factor
l_c	Average length of the coil
l_g	Airgap per side
$l_{ew-bend}$	Span extension one side
l_{ext}	End winding extension
m	Number of phases
p	Number of pole pairs
q	Number of slots per pole per phase

r_c	Average coil radius

Contents

CHAPTER 1

Introduction

This chapter provides an overview of the general research problem and a short background. It outlines the key contributions and details of publications derived from the thesis work.

1.1 Problem Background

The journey towards electric cars started with the need to reduce dependency on fossil fuels, which would eventually reduce greenhouse gas emissions. The advancements in electric motor design, battery technology, and power electronic converters have made Electric Vehicles (EVs) more affordable, efficient, and accessible. Thus, the growing environmental concerns and advancements in charging infrastructure have driven the transition from conventional Internal Combustion Engine Vehicle (ICEV) towards EVs. Battery Electric cars have become the primary alternative to ICEV, with numerous automakers planning to electrify their fleets in the coming years.

As the electrification of cars continues to gain momentum, the focus is now shifting towards expanding this technology to larger, more demanding vehi-

cles, such as trucks, playing a crucial role in reducing emissions from heavy-duty transportation. The electrification of commercial vehicles, such as trucks, is gaining traction as the next major phase in transportation sustainability. Trucks, especially heavy-duty and long-haul vehicles, contribute significantly to carbon emissions, making their electrification essential for achieving broader climate goals. Electric trucks are being developed to reduce emissions, lower operational costs, and improve energy efficiency.

The electrification of cars is already well underway, trucks are starting to embrace electric technology, and the aviation industry, while still in its infancy, is beginning to explore electrification as part of its long-term sustainability goals. Each sector faces unique challenges, but the overall trend is toward reducing emissions, improving energy efficiency, and relying on renewable energy sources to power the future of transportation.

In this transition, electrical machine topologies, such as Axial Flux Machines (AFMs), are investigated with respect to compact size, high power density, and efficiency advantages over traditional Permanent Magnet (PM) Radial Flux Machine (RFM) designs. The AFM may be a good alternative, especially for electric trucks and aviation, where space, weight, and power-to-weight ratios are critical factors. If enabling more efficient and lightweight propulsion systems, AFMs would enhance the performance and sustainability of EVs across all transportation sectors.

A forecast of substantial growth in the next decade of AFMs, as well as in-wheel and switched reluctance motors, are expected in [1], stating that AFMs offer high peak power output with a relatively low mass, indicating their possible high-power density of up to $10kW/kg$ which should be related to an upper limit of $5kW/kg$ for RFMs (for similar power levels).

Building on the analysis of emerging motor technologies, modeling techniques like the Finite Element Method (FEM) is crucial for optimizing the design and performance of AFMs, enabling more precise predictions and improvements in their efficiency and integration within EVs. AFMs are often designed and analyzed using Three-Dimensional (3D) FEM models, which provide a more accurate representation of the motor's complex geometry and electro-

magnetic interactions compared to traditional Two-Dimensional (2D) FEM models (which are mostly used when modeling RFMs).

While 3D computations offer high accuracy, and are computationally expensive, especially while iterating multiple design variations (which are needed during design optimizations). In contrast, a 2D model provides a faster and more efficient alternative for initial motor design and analysis. Thus by simplifying the geometry and focusing on the key performance aspects such as flux distribution and torque generation, 2D models allow engineers to quickly assess and optimize designs before committing to more resource-intensive 3D simulations. This makes 2D models a valuable tool in the early stages of development, enabling quicker decision-making and reducing overall design time, offering useful insights into the motor performance.

A key disadvantage in the usage of 2D models for AFM design is, of course, their inability to accurately capture the edge effects, which are inherently present in 3D models, where the magnetic field and the electromagnetic interactions near the edges of the rotor and stator are fully accounted for. Since 2D models are unable to capture the complex effects at the boundaries, this can lead to inaccuracies in predicting performance, for example at higher speeds. Addressing this gap by developing more advanced 2D modeling techniques or hybrid models that integrate edge effects could significantly enhance the accuracy when predicting output performance and during early-stage motor design.

1.2 Purpose of Thesis and Contribution

The purpose of the work is to find accurate and efficient electromagnetic models of AFMs, that may be used for further studies such as investigations of when the AFM can perform better than the RFM, and how current solutions can be improved in terms of manufacturing, torque and power density, and regarding recycling/reuse aspects. In that respect, the purpose here is to model a physical AFM to validate simulation results and to perform a comparative analysis of 2D and 3D FEM modeling approaches including modeling resolution and sensitivity analysis.

This study thus aims to quantify the limitations of 2D FEM models in capturing the edge-related electromagnetic phenomena. Additionally, the work investigates the specific aspects and effects that are not included in 2D models, providing valuable insights for possible adaptations of the 2D models with analytical or empirical models that can be used in future design work or for control purposes.

The main contributions are the following:

- A physical AFM was analyzed, and measurements were acquired to develop a 3D FEM model of the machine. The validation of the 3D FEM no load and load test simulation results against the physical AFPM machine is presented. The 3D model was parameterized and subsequently transformed into a modified equivalent 2D model by parameterizing the dimensions for a single computational plane. The developed 2D model incorporating the Linear Machine Modeling Approach (LMMA) is demonstrated. Although the LMMA method is not new, the detailed description of the procedure, including the importance of the choice of work plane, is not found in literature and is believed to be very helpful for other researchers in the field.

- A comprehensive comparison between the 3D and 2D models was conducted, with the investigation primarily focusing on analyzing the end leakage flux, variations in mesh densities, and time steps. An extruded 2D model was built to deepen the comparison between 3D and 2D models with varying mesh density. Five distinct models were developed to quantify the end leakage flux in detail, considering its behavior along the magnets and the coils. Any differences in torque and loss components were also shown and explained. Such comprehensive comparison has not, to the authors' knowledge, been presented before for AFMs.

- The study was extended to investigate the end-turn leakage inductance in AFMs using both 3D and 2D modeling approaches together with analytical methods available in the literature that was modified by the author so that they may be suitable for Concentrated Winding (CW) AFMs. The work thus begins to fill a gap in the literature, regarding finding accurate formulas that can be used to incorporate analytical models of end-turn leakage-inductance combined with 2D FEM of

AFMs.

1.3 Thesis Outline

The structure of this thesis is designed to provide a comprehensive analysis of the modeling of AFMs, with a particular focus on end-turn inductance and end leakage flux. It begins with an introduction to the background and objectives of the study.

Chapter 2, provides an overview of the relevant background on AFM design, focusing on design variations related to electromagnetic principles. It also covers the transformation from 3D to 2D models, as well as key design aspects such as materials selection, manufacturing processes, and thermal and mechanical considerations.

Chapter 3, details the measurements taken from a $4kW$ AFM to build a reference model. It includes the process of gathering data on the physical machine's dimensional parameters, and electromagnetic characteristics, which are then used to develop an accurate reference model for further simulation and analysis.

Chapter 4, focuses on the development of both 3D and 2D models of the AFM through parameterization. This chapter outlines the process of constructing these models, detailing the dimensional parameters used for the 3D model and the transformation of the 3D model into an equivalent 2D model.

Chapter 5, presents a comparison between the 3D and 2D models of the AFM, focusing on variations in mesh density, time step, and end leakage flux. This chapter evaluates how different mesh densities and time steps affect the accuracy and computational efficiency of both models. Additionally, it investigates the differences in capturing end leakage flux, providing a deeper understanding of the impact of these factors on the performance of the 3D and 2D models.

Chapter 6, focuses on the calculation and analysis of end-turn leakage inductance in AFM. It compares different methods for calculating end-turn leakage inductance in 3D model. The chapter discusses the specific challenges in cal-

culating this inductance and evaluates the accuracy of the results obtained from each method, providing a deeper understanding of the approaches.

1.4 List of Publications

[1] **Vineetha Puttaraj**, Sonja Lundmark, Torbjörn Thiringer. "Moving from a 3D Axial Flux Machine Model to 2D Considering the Impact of End Leakage Flux", *Published in International Conference on Electrical Machines (ICEM)*, 2024.

[2] **Vineetha Puttaraj**, Sonja Lundmark, Torbjörn Thiringer. "Evaluation of Efficient 2D Axial Flux Motor Models with End Turn Leakage Inductance Consideration", submitted to *IET special issue on Opportunities and Challenges in Design and Optimisation of Axial-Flux Electric Machines*.

CHAPTER 2

Background of Axial Flux Machine Design

This chapter provides a review on AFM topologies, comparison between AFM and RFMs, electromagnetic designs, reviewing 3D and 2D transformation methodologies, thermal aspects with cooling systems and mechanical considerations and scaling effects with materials and manufacturing techniques of AFM design.

2.1 Axial Flux Machine Topologies

The AFM offers some structural and performance benefits compared to RFMs, but the main difference is that in AFMs, the magnetic flux flows parallel to the axis of rotation unlike the RFM where the flux runs perpendicular to the axis. This results in the disk-like structure of AFMs, where the stator and the rotor are arranged in parallel planes. The Axial Flux Permanent Magnet (AFPM) machine has sandwiched structures, often with either a rotor or a stator in the middle covered by two stator discs or two rotor discs, respectively. Some topologies have multiple stacks of stators and rotors.

A general classification of AFPM machines is described in [2], with five hier-

archical levels based on machine structure, core, slotting, winding, and PMs. The most common structures are categorized based on the number of stators and rotors. The single stator single rotor, or single-sided machine, serves as the fundamental structure from which both the double stator single rotor type (also known as the Kaman type) and Torus type machines are derived. The Torus type encompasses popular AFPM variants, including the coreless machine, the Yokeless And Segmented Armature (YASA) machine, and the toroidal winding machine. The machines are also classified based on core material. It can be with an iron or ironless core and the stator core materials could be steel lamination or non-traditional ferromagnetic materials such as Soft Magnetic Composite (SMC), amorphous metal, or charged polymers. Another classification is based on slotting and discriminates between the presence or absence of stator slots and this relates to machines with iron cores. Regarding windings, the drum winding (Distributed Winding (DW)) and the ring winding (Concentrated Winding (CW)) are the two classes of windings available and they differ in the design of the end connections. These end connections are placed circumferentially along the outer and inner radii, and they can be overlapping or non-overlapping. The PMs are mostly inset or surface-mounted magnets with magnetization along the axial direction, but a few examples exist where interior magnets are used with the magnetization in the circumferential direction, where the latter case yields some reluctance torque, additional to the alignment torque. The magnets may be placed so that opposing magnets have the same polarity or with opposite polarity.

Several comparisons of AFM topologies are found in the literature. For example, in [3], the Single Stator Single Rotor (SSSR), Double Stator Single Rotor (DSSR), and the YASA AFM configurations are compared for torque and power density, PM mass, manufacturing complexity, electromagnetic losses and cooling complexity. In this comparison the Double Rotor Single Stator (DRSS) (YASA) possess higher torque and power density, but have higher PMs mass, and have higher cooling complexity. Furthermore, the DSSR was found to have higher manufacturing complexity, require lower PM mass, and have lower cooling complexity whereas the SSSR topology had lower manufacturing complexity and lower electromagnetic losses, all according to [3].

2.2 Main Differences between Axial Flux and Radial Flux Machines

As mentioned, the main difference between RFMs and AFMs regards the direction of the magnetic flux, and this results in that the AFM benefit from a high diameter/length ratio. Therefore, the AFM can be good for applications with specific space limitations like automobiles. Such applications were investigated in [4], where conventional RFMs were compared with AFPM machines with a DRSS structure. The author concludes, based on optimization studies, that the torque density of the AFPMs depends on the axial length while the RFM torque density is independent of the axial length of the machine. Also, it was concluded in [4] that AFPM machines can have higher torque density than the RFM since the AFM geometry allows for larger slot spaces, provided the windings are efficiently packed with high fill factor to maximize the utilization of the additional slot space.

Also in [5], it was found that the AFM may achieve a better torque density, comparing an AFM with an external rotor RFM with concentrated stator windings and with a Hallbach array surface PM in the rotor. Both machines in [5] meet the specification of EV motors of 50 kW continuous power operating at a speed of 6500 rpm. It was found that PM retention is needed at high operating speeds for both the RFM and the AFM but here the external rotor RFM is advantageous over inner rotor machines (although the outer rotor radial RFM presents cooling challenges due to the placement of windings in the inner stator). The overall analysis of [5] indicates that both machines produce approximately the same torque with the AFM having lower active mass and slightly lower active volume than the RFM.

It should be noted that the difference in machine configuration between axial and radial flux machines leads to differences in terms of cooling efficiency. The active parts of the windings in RFMs are positioned in such a way that they are, via the stator core, in thermal contact with the machine's housing and cooling ducts whereas the end windings are more difficult to cool. However, in AFMs, depending on the design, the whole windings may be close to the housing, and therefore cooling the surface of the machine would influence the whole windings directly. Cooling was also a point of investigation

in [6], where the focus is on comparing the structure of the machines, electromagnetic losses, noise and vibration, and cooling. It is mentioned in [6] that when using rectangular windings, less conductive materials may be used for the slotting of the AFM iron core, which may reduce electromagnetic losses.

In [7], key geometrical parameters including the air gap are compared regarding the performance of RFMs and the axial flux YASA machine. Both these motor types are compared for torque density, overload capacity, and efficiency, using magnetic equivalent circuit and Finite Element Analysis (FEA) methods. A comparison of the electromagnetic properties, considering different air gap areas and air gap diameters, revealed that when the air gap is small, the weight power density is higher in RFMs. Conversely, as the air gap increases, the weight power density becomes higher in YASA machines. It was further concluded in [7] that the air gap is proportional to overload capacity and that YASA motors have greater overload capacity and are more efficient when overloaded, compared to the RFM.

Also in [8] the AFM seems to present a good choice, where, an AFPM with ferrite PMs and round copper wire is compared with an off-the-shelf RFM with Neodymium sintered PMs and rectangular copper wire. The comparison showed that the proposed AFPM machine realizes higher efficiency across a wide operating area and achieves the target torque at low cost with potential usage in traction applications.

2.3 Electromagnetic Designs

Electromagnetic design considerations of AFMs are quite similar to that of RFMs, in that respect that the magnetic and electric loadings should be balanced for the target specification. For example, the rotor PMs should give sufficient flux and withstand demagnetization fields, and the stator and the rotor core should lead the magnetic flux without causing saturation nor causing excessive leakage fields. Some of these design considerations were addressed in [8]. A rotor structure with a sufficiently large PM cross-section area and with carbon fiber reinforced plastic around the ferrite magnets, as shown in Figure2.1a, is claimed in [8] to achieve sufficient mechanical strength as well as

the target torque. A significant amount of work was also done in [8], investigating the suitable structure of the stator tooth tips. A parametric study was conducted with the tooth tip variable parameters as shown in Figure 2.1b and the corresponding magnetic flux with the tooth tip patterns with five models shown in Figure 2.1c. Shape 1 in Figure 2.1c has the lowest average torque because of the large amount of magnetic flux leaking between the tooth tips. This indicates that a large amount of magnetic flux does not contribute to generating torque. Shape 2 has a larger distance between teeth g, compared to shape 1, and achieves the required average torque. Shape 3 has a trapezoidal tooth tip due to a smaller tooth tip height t, and has a larger average torque compared to shape 1. Shape 4 has a smaller tooth tip than shape 5 which is used in the proposed model considering also that peak-to-peak torque ripple was lowest in shape 5. Furthermore, the eddy currents in the stator windings were evaluated when the machine operated at a high speed of $6800rpm$. Two patterns were used to evaluate the eddy currents with round copper conductors. The first pattern had a lower number of parallel paths and higher wire diameters than pattern 2, resulting in 60% and 81% lower losses than off-the-shelf RFMs.

2.4 Review on 3D to 2D Model Transformation Methodologies

The AFMs are 3D problems because of the 3D main flux distribution, unlike most conventional RFMs. Therefore, 3D Finite Element Method (FEM) models are required for accurate computations. However, modeling such complex geometries takes a significant amount of time compared with 2D FEA modeling and requires serious competency. Therefore, several attempts are made to reduce the 3D motor models into 2D models. One example of this is given in [9] where the transformation steps are clarified as described in this section.

The investigated approaches include the Inner Rotor Modeling Approach (IRMA), the Outer Rotor Modeling Approach (ORMA), and the Linear Machine Modeling Approach (LMMA), as shown in Figure 2.2. Each symmetric 3D problem is then sliced into 3D symmetry models. The 3D symmetry is approximated to several numbers of 2D motor models at different radii. Each 2D model represents a different radial cross-section. Contrary to 2D LMMA,

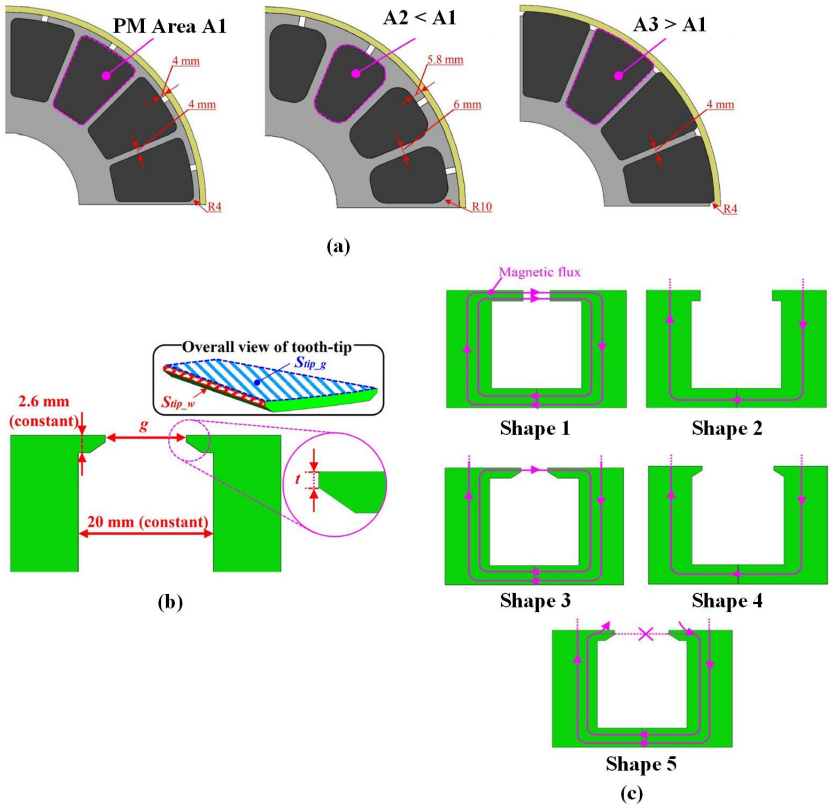

Figure 2.1: Rotor and stator design performed in [8] (a) Comparison of rotor models to enhance torque with Model-A as the first conventional model, Model-B as the second conventional model and Model-C is the proposed model, having the largest PM area; (b) Possible variable parameters in tooth tip; (c) Analytical models and magnetic flux under different t and g

2D IRMA and 2D ORMA motor models would have various inner-outer diameters according to the radius of the computational planes or cut-planes. The inner-outer diameters are determined by the radius of the air gap for each 2D IRMA and 2D ORMA motor models. The author in [9] investigated the reduction techniques of AFPM motors with fan-shaped magnets, triangular-shaped magnets, and coreless AFPM motors and concluded that 2D ORMA cannot be applied for fan-shaped and triangular shaped magnet motors, whereas complex PM shaped AFPM motors such as skewed magnets which have non-central symmetric magnet structures can be modeled in 2D IRMA and 2D LMMA.

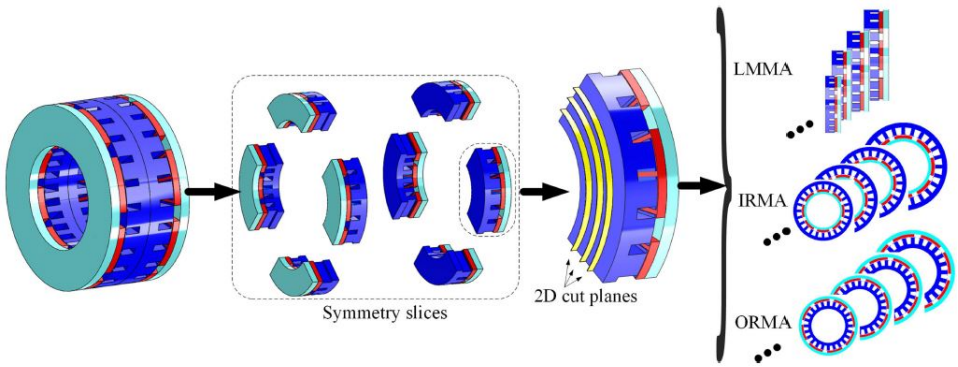

Figure 2.2: Reduction of a DRSS AFPM from a 3D motor model to 2D by using 2D symmetry modeling approaches [9]

2.5 Thermal Aspects Including Cooling Systems

In this section, some thermal aspects of AFMs are highlighted based on findings from literature. Effective thermal management is crucial in AFM design and operation, as excessive heat can impact the efficiency and performance of the machine. The compact design and high power density in AFMs are particularly susceptible to thermal challenges, requiring advanced cooling systems to maintain optimal operating conditions.

In [3], cooling approaches for stators and rotors are reviewed. The reviewed cooling approaches for rotors include ventilated rotors, surface-mounted pro-

truding magnets, rotor-embedded radial fins, and rotor liquid cooling. In Figure 2.3, different rotor carriers, such as flat rotor carriers and bladed rotor carriers are illustrated together with the mentioned magnet designs. The author concludes that rotor vents and protruding magnets in the same rotor, as seen in Figure 2.3c and 2.3f, reduce the magnet temperature significantly.

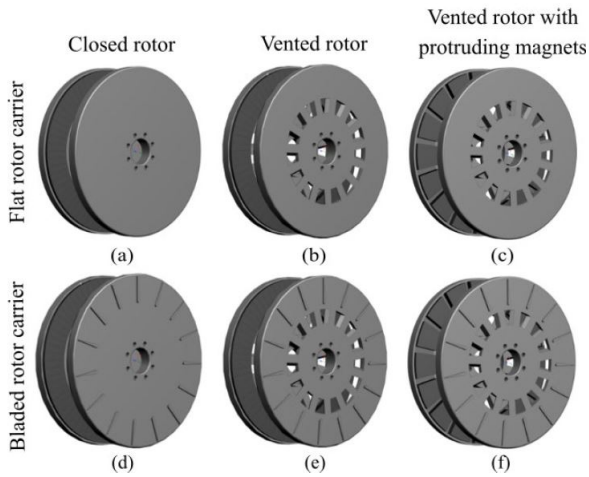

Figure 2.3: Rotor carrier geometry variations based on cooling features discussed in [3]

The stator winding cooling strategies reviewed in [3] included stator cooling jackets, heat transfer fins, internal flow channels, immersion coils, hollow coils, and heat pipes as illustrated in Figure 2.4. The stator cooling jackets are liquid cooling solutions that indirectly cool the copper coils since they are not in direct contact with the conductors. The cooling jackets can be on the outer diameter and the end cover of the machine. The outer diameter cooling jacket as shown in Figure 2.4a is used in single-stator and double-rotor configurations, while the end cover jackets as shown in Figure 2.4b are used in double-stator and single-rotor configurations. It should thus be noted that the cooling location depends on the machine's configuration.

The cooling performance of the cooling jackets can be improved by extended protrusions or fins. The addition of stator cooling fins as shown in Figure 2.4c

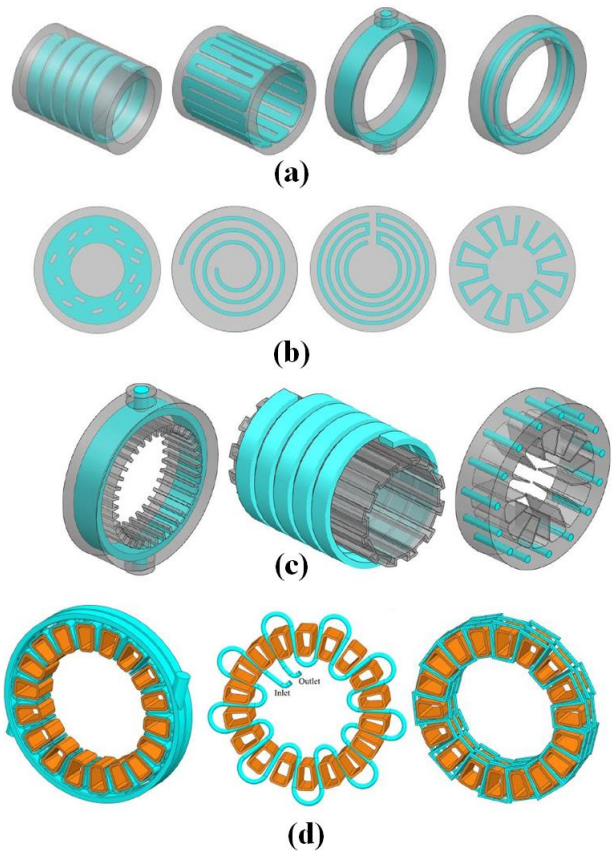

Figure 2.4: Cooling options presented in [3]: (a) Outer diameter liquid cooling jackets; (b) End cover liquid cooling jackets; (c) Stator cooling fins; (d) Different channel cooling configurations for stator cooling

can improve the thermal resistance from the heat-generating components by increasing the contact surface area of the cooling jacket material. Another method that can enhance the cooling is internal flow channels. Such channels directly address the sizeable copper losses in the stator and are the most effective cooling method that reduce the thermal resistance from the coolant to the windings. The internal flow channels are positioned close to the coils, with some possible designs as shown in Figure 2.4d.

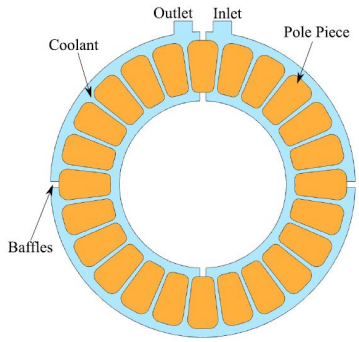

(a) Baffle design

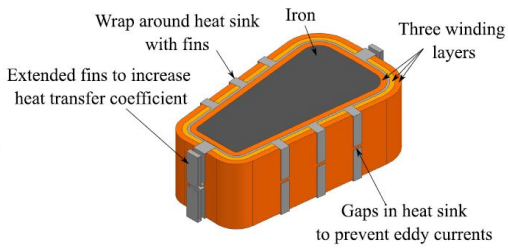

(b) Heat sink design with fins

Figure 2.5: YASA AFPM immersion design [3]

Direct cooling by immersion includes complete motor flooding. Due to the high speeds in applications like heavy-duty vehicles and aerospace, there are increased rotor windage losses, and fully flooded solutions are not recommended, according to [3]. Innovation within immersion design involves baffles, fins, flow reducers, heat sinks, intricate coil designs, and maximizing the contact area between the coils and coolant. One such design, was demonstrated in [3] as shown in Figure 2.5a where the stator cavity is divided into four sections, creating an even flow distribution between the stator coils. The improved immersion with baffle design reduced the hot spot temperature by 13°C and increased current density by 7% compared to the flooded design. The heat sink design as shown in Figure 2.5b compared to the baffle design in Figure 2.5a allowed an even higher increase in current density. These heat sinks were designed for traditional concentrated windings. The heat sink is made of $0.1mm$ sheet copper and is placed between the inner and middle windings extending into the stator cavity. This design removes heat from

the inner mid-winding region. However, the electromagnetic losses and eddy current losses were not assessed with the addition of the integrated heat sink.

2.6 Mechanical Considerations and Scaling Effects

In [10], the scalability of a proposed YASA machine is studied for electrified aviation application with a peak power of $250kW$ at $12kW/kg$ and $5000rpm$. Due to higher permeability and lower losses, cobalt steel is preferred in the stator teeth. The PMs in the rotor are segmented to minimize eddy currents. Hallbach array is used so the rotor flux has a return path within the PMs, thus eliminating the need for a heavy back iron, and the magnets are mounted on a lightweight carbon fiber-reinforced polymer. Table 2.1 compares and tabulates three machine designs, with data from the investigations done in [10]. Machine-1 is the base machine and it is concluded that scaling to lower power reduces the efficiency, active torque, and power density. In this case, the power density varies more than the torque density, due to different speeds at different power levels. For the large-scale design (Machine-3), a large winding cross-section results in large AC losses in the winding. At higher power levels due to thicker magnets, the magnet losses are increased which makes the magnet segmentation impertinent. Core losses are higher in Machine-1 relative to the other designs due to the compact design (shorter stator length), high speed, and high current leading to increased flux density and frequency effects in the stator core. AC winding losses were dominant in Machine-3 which had the highest speed and DC losses dominated in Machine-2 with the lowest speed.

2.7 Materials and Manufacturing

In [2], some materials suitable for AFMs are reviewed such as SMC, charged polymers, amorphous magnetic material, grain-oriented steel, and non-magnetic materials like plastics. The Kaman type using SMCs are reviewed, where SMCs are mainly used in the stator teeth. These stator teeth are obtained by milling the SMCs and the other way of obtaining the 3D shapes is by compacting the SMC with design molds. Additionally, a YASA type AFM with SMC in the stator teeth was investigated in [2], where the SMC powder was separately pressed to form shoes and central parts of the teeth. Such teeth built with SMCs were shown to have a high slot fill factor of 65%, even with

Table 2.1: Comparison of three YASA machines from data in [10]

Parameters	Machine-1	Machine-2	Machine-3
Outer diameter (mm)	270	270	520
Inner diameter (mm)	220	220	440
Stator length (mm)	35	25	30
Magnet axial thickness (mm)	10	10	30
Air gap thickness (mm)	1	1	2
Slots/Poles	42/40	42/40	42/40
Speed	5000 rpm	2700 rpm	6800 rpm
Torque (Nm)	477	400	1970
Power (kW)	250	113	1400
Efficiency (%)	95	93	94
Active torque density (Nm/kg)	63	56	72
Active power density (kW/kg)	33	16	52

a round wire conductor. Furthermore, it was found in [2] that a single-sided AFM operated at 1285 rpm and 300 Hz, with the stator and rotor both built with SMC had 19% lower losses and 12% higher efficiency compared to the machine rotor without SMC, due to the high resistivity of the SMC limiting the induced currents in the rotor.

Amorphous materials have high permeability and low hysteresis losses. Reference [2] investigated the use of amorphous material in Torus AFMs. The stator teeth are made from cut Amorphous magnetic material cores and this resulted in 86% efficiency for most of the torque/speed range of a 150 W machine, with ferrite PMs and a rotor core made with solid steel. When used in a slotless Torus machine, the toroidal core was wrapped with an amorphous magnetic material ribbon encapsulated in resin, resulting in 96% efficiency at 14000rpm despite having the same rotor as the 150 W machine, giving 10% lower losses. The use of plastic bonded magnets or segmented magnets in order to reduce losses is further highlighted in [2].

In [11], grain-oriented laminations were used in AFMs with a central stator machine configuration. A version of grain-oriented material was used so that loss data were scaled from $50Hz$ to a higher frequency since most of the commercial grain-oriented materials are made for $50/60Hz$ at lamination thicknesses not lower than $0.3mm$. The author concludes that these materials have the potential to produce low loss AFMs, comparable to or better than RFMs.

Some materials used in RFMs and AFMs are investigated in [8], like electromagnetic sheet steel 35A270 for the stator core in a RFM and SMC HB2 is mentioned in [8] as the mass-produced SMC material with the lowest iron loss. Still, the sheet steel 35A270 iron loss was way lower than with SMC HB2. Also in [8], a non-magnetic stainless steel material like carbon fiber reinforced plastic-SUS304 was used as PM holders, and magnet materials such as Neodymium sintered PM NMX-39EH and ferrite PM like NMF-15G was used, and detailed material properties was given. For example, the ferrite PM has 63% lower residual magnetic flux density and 66% lower coercive force compared to Neodymium sintered PMs. Still, the results in [8] showed that the AFM with ferrite magnets performed better than a comparable RFM with

Neodymium magnets.

The recent trends in AFPM machine fabrication are reviewed in [12]. Unlike RFMs, AFPM machines require radial laminations, which makes assembly challenging. In [12], a wire EDM technique was used to cut slots into a tape-wound core, and these slots were then machined. However, this machining process was found to introduce short circuits between the lamination layers. The author of [12] states that laminated cores are more efficient at low operating speeds, where frequencies are lower. However, at higher operating frequencies, SMC and laminated cores achieve similar efficiencies, due to increased eddy current losses in laminated steel at these higher frequencies. Additive Manufacturing (AM) technique was also reviewed in [12] and significant work was carried out highlighting the comparison of laminations, SMCs, and additively manufactured stators for AFMs. The additively manufactured stator showed in [12] lower core losses compared to laminated and SMC stators across both low and high-frequency operating regions. AM techniques are also reported to be used for fabricating windings.

In [13], a 10kW, 16 poles and 15 slots YASA AFM was built with AM. New design solutions were proposed which are hard to produce with traditional manufacturing techniques. An additively manufactured shape-profiled core design with cylindrical shaped layers as shown in Figure 2.6 is claimed to minimize the eddy current loss in the core especially at higher frequencies. Additionally to investigating AM-techniques, laser-cut grain-oriented electrical steel of grade M100-23p was used in the YASA machine in [13]. It was highlighted that guillotine-cut or water-cut laminations can reduce core loss in the MP100-23p laminations compared to laser-cutting at higher frequencies, both the guillotine- and water-cutting techniques have almost the same core losses. Therefore it was concluded that the proposed additively manufactured shape profiled core was the best solution for manufacturing high speed YASA machines compared to the conventionally-stacked laminations. The proposed AM core had better magnetic flux density distributions over its cross-section area and consequently lower core losses. Epstein frame setup is used to measure the magnetic material characteristics. The effect of different cutting techniques is also investigated as a possible solution to limit the core losses.

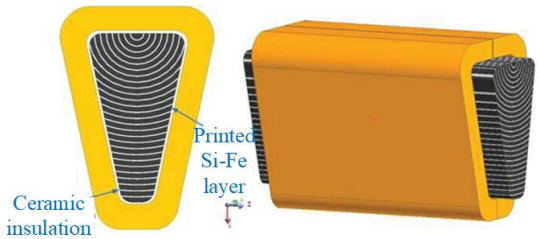

Figure 2.6: Proposed AM shaped profiled core with cylindrically shaped layers [13]

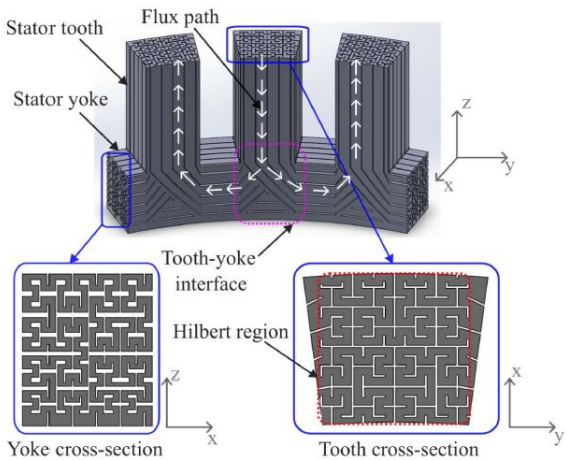

Figure 2.7: AFM stator design with Hilbert pattern [14]

In [14], an AM stator was designed with a Hilbert pattern to minimize eddy current losses. The Hilbert pattern is known for continuous fractal space-filling curves. The Hilbert space-filling curve design was separately considered for the stator yoke, stator teeth, and the interface between the yoke and the teeth as shown in Figure 2.7. In the stator yoke, the flux path is circumferential and the stator teeth carry flux in the axial direction. In the interface, the Hilbert space-filling curve of the stator yoke overlaps with the Hilbert space curve of the teeth. The stator was built using selective laser melting and the built component is attached to a baseplate in the selective laser melting process, and electric discharge manufacturing was used to remove the stator from the

baseplate. The stator was dipped in a solution of an inorganic insulating agent to coat the entire surface, including the air regions within the stator Hilbert structure. The purpose of this is to electrically insulate the stator surface and inhibit corrosion. Finally, coils were wound on the stator using AWG 12 equivalent insulated copper wire with a rectangular cross-section. The author of [14] concluded that Hilbert space-filling curve reduced the eddy current losses by approximately 50% compared to a solid structure. The AM stator had however a low stacking factor resulting in 18% lower magnetizing flux compared to a baseline stator. Still, the mass of the AM stator is 30% lower than the conventional stator. The experimental results show that the static torque of the AM machine is 22% lower than baseline machine, resulting in a net torque density (Nm/kg) improvement.

CHAPTER 3

Measurements of a 4kW Axial Flux Machine to Build a Reference Model

This chapter presents a detailed examination of a DSSR AFPM machine, focusing on its configuration, dimensional measurements, machine geometry, winding details, and the experimental setup employed for testing. By documenting these aspects, the chapter aims to provide a comprehensive understanding of the machine's physical characteristics, which are crucial for modeling the machine.

3.1 Configuration of the Reference Axial Flux Machine

The reference AFPM machine under investigation is a double-stator, single-rotor configuration. It is a 4 kW machine with an outer diameter of 169 mm. The investigation of the machine includes extracting the dimensions of the stator, rotor, and PM, as well as the type of lamination, slot dimensions, winding specifications, and details regarding magnet fixtures. Three similar AFPM machines were acquired to support the investigation. One of these

machines was disassembled and cut along the X, Y, and Z axes, resulting in various component parts. The three AFPM machines are referred to as AFM-1, AFM-2, and AFM-3 for clarity. AFM-1 is employed to measure the stator winding resistance, whereas AFM-2 has been disassembled to enable further investigations into the structural details and fixtures of various components within the machine. AFM-3 is utilized for conducting experiments in the laboratory. These details will also assist in constructing the 3D simulation model. The structure of the AFPM machine features a steel laminated dual stator with a rotor sandwiched between the two stators, hence the designation DSSR AFPM. The rotor contains inset PM that are glued into the rotor core. The various stages involved in dismantling the machine are shown in Figure 3.1. The AFM nameplate details are tabulated in Table 3.1.

Table 3.1: Name plate details

Description	Value
Model	TZ16XFZH4096
Voltage	96V DC
Rated power	4 kW
Peak power	8kW
Rated speed	2000rpm
Maximum speed	4000rpm
Rated torque	19Nm
Peak torque	50 Nm
Cooling method	Natural air cooling

Figure 3.2 illustrates the cutting of the stator along the pink and blue lines. The pink line bisects the stator, while the blue line segments it into three parts. The first part consists of one-half of the stator, labeled as I-1 and I-2. The sections marked II and III are divided by a chord. The portion of the stator designated as II is removed from the machine frame, resulting in two pieces labeled II-1 and II-2. The section labeled III is cut along the axial

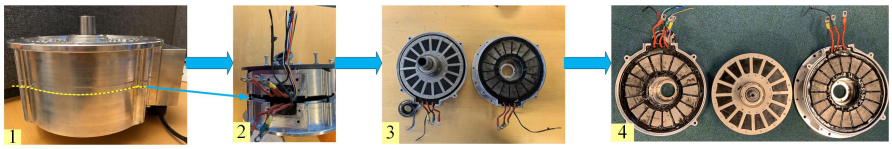

Figure 3.1: Stages in machine dismantling: 1 - Screws were unscrewed along the XY plane (yellow color line); 2 - Machine after unscrewing the screws along the yellow colored line; 3 - one stator separated; 4- Double stator and single rotor separated

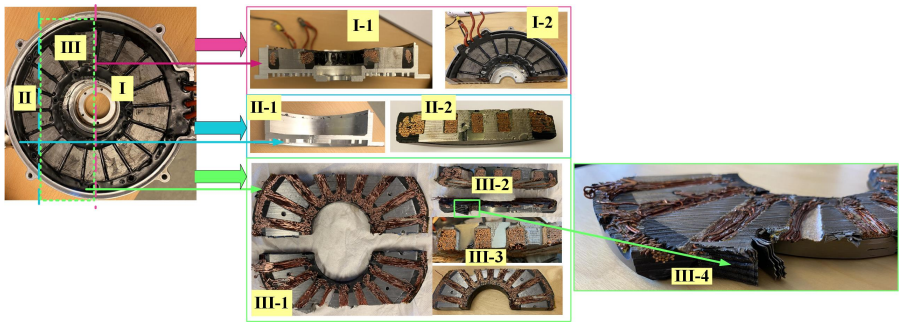

Figure 3.2: Stator cutting details: pink and blue color lines separate the stator into three parts. I-1 and I-2 forms half of the stator; II-1 and II-2 are pieces along the blue-colored chord, the second part is the piece giving the slot dimension details; III-1, III-2, and III-3 forms the third part of the stator revealing dimension of the tooth body, and the third part is axially slit to half; III-4 is zoomed out of III-2 with lamination details

direction, resulting in a part designated as III-1, as shown in Figure 3.2. The piece labeled II-1 in Figure 3.2 helps in determining the dimensions of the slot; the part labeled III-1 in Figure 3.2 is useful for measuring the dimensions of the tooth body, while the piece labeled III-4 demonstrates that the machine utilizes lamination rolled in the radial direction as illustrated in Figure 3.3. The length of a single copper strand wound closely around the tooth body is calculated by measuring the dimensions of the tooth body from the component labeled III-1 in Figure 3.2.

In addition to the investigation of the stator, the rotor of the AFM is also examined. This investigation includes details about the magnet fixture, along

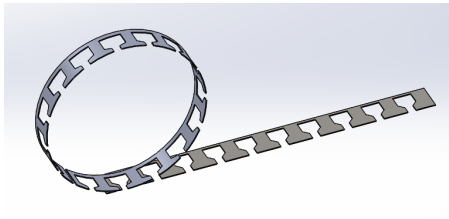

Figure 3.3: Stator rolled lamination

with the dimensions of the magnet, shaft, and rotor. The rotor of the reference AFM is labeled as 1 in Figure 3.4. The outer diameter of the rotor core is determined by measuring its circumference. The shaft is secured to the rotor, as shown in the sections labeled 1 and 2 in Figure 3.4. The thickness of the shaft is measured to determine both the rotor's inner diameter and the shaft's diameter. One of the magnets from the rotor is removed by unscrewing the magnet holding plates, as illustrated in Figure 3.4. The detached magnet piece aids in measuring its width, length, and thickness. The PM used are quite brittle and tend to break easily. The thickness of both the rotor and the magnet is the same. These PMs are inset and trapezoidal. The investigation reveals that the PMs are secured to the rotor core with an adhesive and supported by holding plates. These details can be observed in the sections labeled 3, 4, and 5 in Figure 3.4.

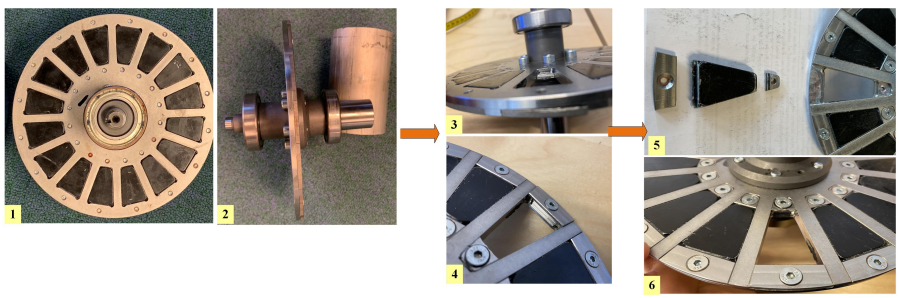

Figure 3.4: Rotor and magnet details: 1- Rotor top view; 2- Rotor side view; 3 and 4- Magnet holding details; 5- piece of magnet and magnet holding pieces; 6- backside of magnet holder.

3.2 Dimension Measurements

This section presents the measurements obtained from the reference AFPM machine. Using these measurements, several unknown dimensions, deemed essential for constructing a 3D model of the reference AFM, are calculated The disassembled AFM components were measured using a ruler, measuring tape, and vernier calipers. The dimensions of the disassembled AFM are divided into axial and radial measurements. Additionally, the length of a single coil wound around the stator teeth and the number of turns are calculated.

3.2.1 Axial Direction

The measurements obtained in the axial direction primarily include the thickness of the stator and the rotor. The machine frame is detached from the rest of the assembly. The frame thickness, on one side of the stator, is denoted as FT_1, which is indicated in the machine frame shown in Figure 3.5. The total air gap is determined by subtracting the stator and rotor thickness from the measured overall length of the machine. The air gap on each side is then calculated from the total air gap, considering the machine's double stator, and single rotor configuration. The length of the air gap on both sides represented as L_G, is calculated using the thicknesses of the stator, rotor, frame, and the overall axial length of the machine, L from

$$L_G = L - (FT_1 \cdot 2) - (ST_1 \cdot 2) - (RT) \tag{3.1}$$

where the length of air gap l_g on one side of the machine is

$$l_g = \frac{L_G}{2} \tag{3.2}$$

The axial measured dimensions of the reference AFPM machine are shown in Figure 3.5 and are summarized in Table 3.2.

Relative difference in air gap calculation

The calculated air gap is prone to some errors, as the blunt edges of the machine frame result in slightly inaccurate measurements of the machine's overall length. The measured overall length is estimated to be 96.5 mm but may be as much as 96.8 mm, yielding a 20% increased air gap.

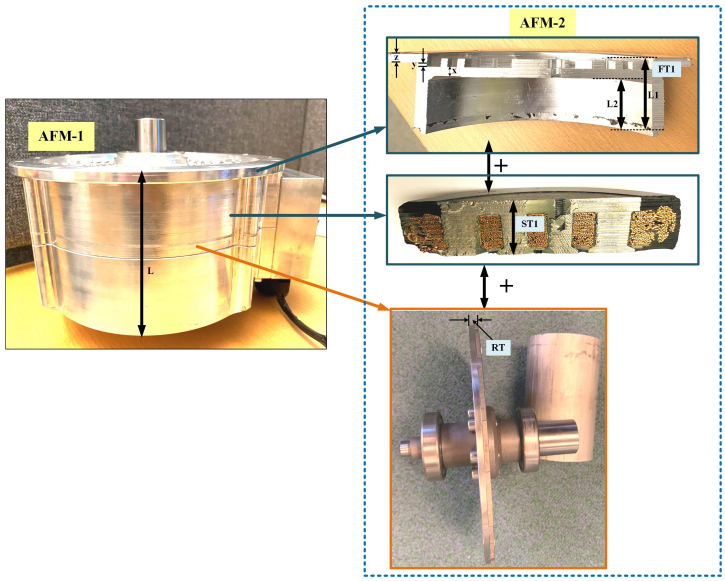

Figure 3.5: Axial measurement - Overall length of the machine measured from AFM-1, L - Overall length of machine; FT_1 - Half of the frame thickness; L_1 - Length of half of the hollow section in the machine frame; L_2 - Length excluding half of the frame thickness; ST_1- Stator thickness of one of the stator; RT - Rotor thickness

Table 3.2: Measurements in the axial direction

Parameters	Values
Overall length of the machine, L	96.5mm
Frame length per side, L_1	51mm
Length excluding frame thickness on one side, L_2	37mm
Frame thickness per side, $FT_1 = L_1 - L_2$	14mm
Stator thickness per stator, ST_1	30mm
Rotor thickness, RT	7mm
Total airgap, L_G	1.5mm
Airgap per side (calculated), l_g	0.75mm
Magnet thickness, PM_{th}	7mm
Slot height, $Hs2$	19mm

3.2.2 Radial Direction

The machine measurements in the radial direction are shown in Figure 3.7 and 3.8. The inner and outer diameters of the rotor are determined by measuring its circumference with a measuring tape and are recorded in Table 3.3. The measured dimensions in the radial direction are the outer and inner diameters of the stator and rotor, length and width of the magnets, tooth body, and tooth rim. The stator is cut along the white dashed line shown in Figure 3.6. The dashed line does not align with the center of the tooth, causing parts of the winding within the slot to become visible, as shown in Figure 3.6 and 3.7. The outer and inner diameters of the magnet are calculated based on the magnet's length the length between the outer diameter of the rotor and the placement of the magnets relative to the outer diameter of the rotor. The length of the tooth rim and the length of the magnets do not add up to the rotor length. This difference is due to the magnets being inset into the rotor core and secured with an adhesive material. The adhesive thickness is measured to be just below $1mm$, as seen in Figure 3.8.

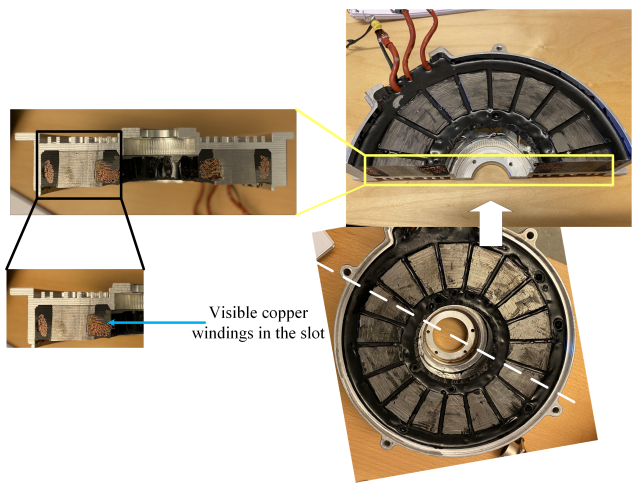

Figure 3.6: Cutting of the stator, cut along the dashed white line.

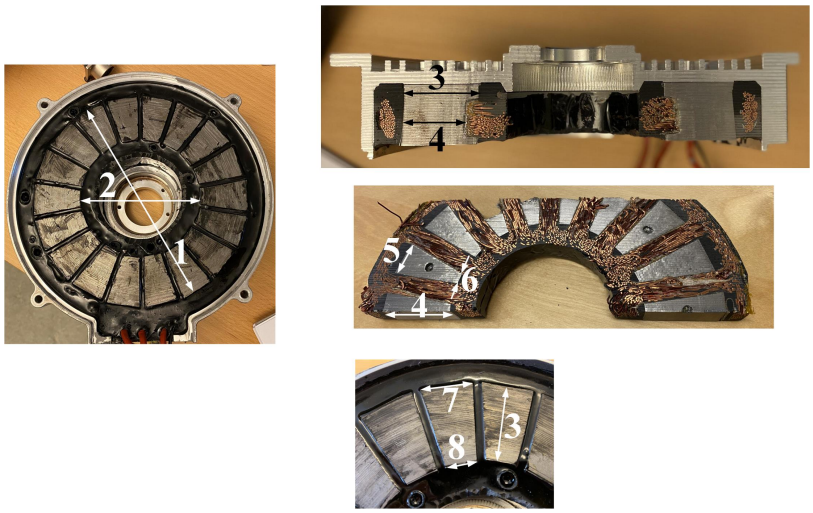

Figure 3.7: Radial measurement - Stator of AFM-2. 1 - Outer diameter of the stator; 2 - Inner diameter of the stator; 3 - Length of the tooth; 4 - Tooth body width at the cutting surface, when the stator cutting is along the white dashed line, seen in Figure 3.6; 5 - Tooth body outer width; 6 - Tooth body inner width; 7 - Tooth tip outer width; 8 - Tooth tip inner width

Table 3.3: Radial measurements XY-Plane

Parameter	Value
Stator dimensions	
Outer diameter of stator	166.2 mm
Inner diameter of stator	94.2 mm
Rotor dimensions	
Outer diameter of rotor	186.2 mm
Inner diameter of rotor	38 mm
Magnet dimensions	
Outer diameter of magnet	164.2 mm
Inner diameter of magnet	96.2 mm
Stator tooth dimensions	
Length of tooth rim	36 mm
Outer arc length of tooth rim	25 mm
Inner arc length of tooth rim	12 mm
Length of tooth body	36 mm

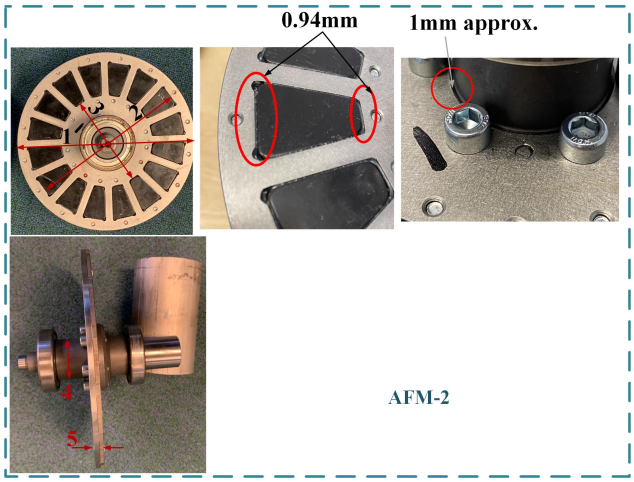

Figure 3.8: Radial measurements - Rotor. 1 - Outer diameter of rotor; 2 - Outer diameter of magnet; 3 - Inner diameter of magnet; 4 - Diameter of the cylinder attached to the shaft; 5 - Rotor thickness

3.2.3 Stator Slot

The stator slots in the reference AFM are of semi-enclosed type. The dimensions of the stator slots are measured from the piece dismantled from AFM-2, as illustrated in the Figure 3.9. The measured slot dimensions are summarized in Tables 3.3 and 3.4 and the reference parameters for the slot details are obtained from the semi-enclosed slot type template in Ansys Maxwell, as shown in Figure 3.10. These slots are classified as slot type-3 in the Ansys Maxwell software, version 2023 R1. The corresponding dimensional parameters are measured from the reference AFM.

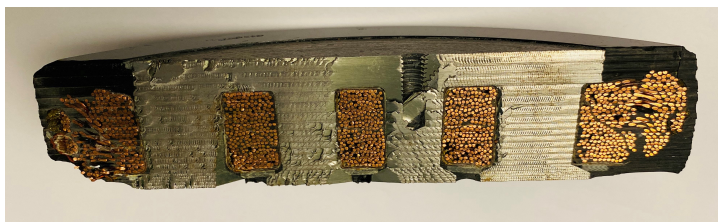

Figure 3.9: AFM-2 semi enclosed slots

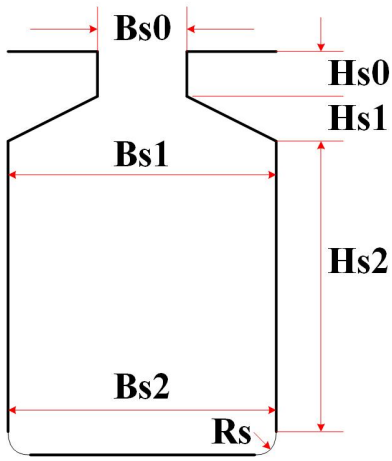

Figure 3.10: Slot type dimensions

Parameters	Specification
Hs0	2 mm
Hs01	0 mm
Hs1	2 mm
Hs2	19 mm
Bs0	4 mm
Bs1	12 mm
Bs2 (W_{ss})	12 mm
Rs	0.2 mm

Table 3.4: Slot dimensions

3.3 Stator Winding Configuration and Resistance

The data obtained by measuring the DC resistance R_{DC} depends on the total length of the conductor in a coil, the number of parallel paths, and the cross-sectional area of the conductor.

3.3.1 Stator Winding Resistance Measurement

The winding resistance of the reference AFM is measured on AFM-1, with the aid of the setup as described in Figure 3.11 and 3.12. The number of parallel branches is assumed to be one per machine half since the coils are connected in series hence a non-accessible wye-point is also assumed.

The DC resistance of the stator winding of a three-phase AFM is measured by connecting a known DC voltage that is applied across the phase terminals and the DC current $0.5A$ - $2.9A$ in 6 steps is measured with a FLUKE multimeter as in Figure 3.12. The test is repeated for the other two sets of the phase terminal connections. The measured DC resistance per phase of the stator winding $R_{s(dc)}$ is $18.2m\Omega$

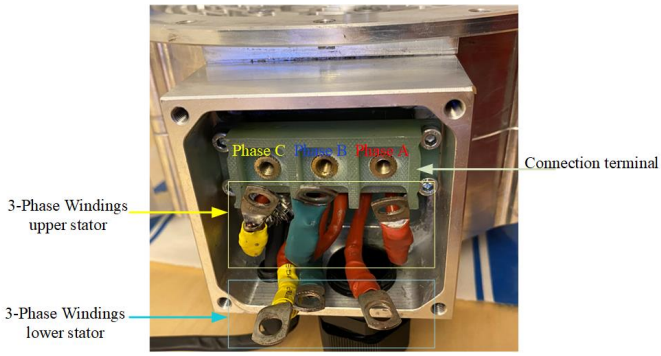

Figure 3.11: Connection terminal used for the measurement of the winding resistance. In the 3-phase windings of the upper stator, the measuring devices (Ammeter and voltmeter) are connected between two phases

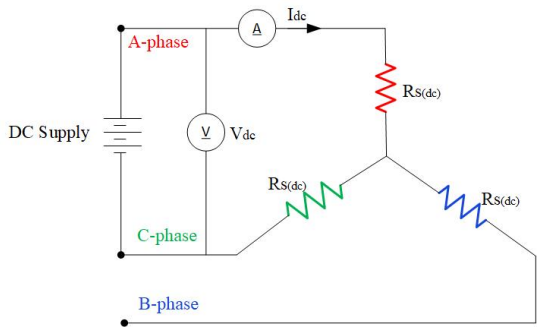

Figure 3.12: Connection diagram for the winding resistance measurement for one stator. The DC voltage source is connected across two phase terminals

3.3.2 Analytical Calculation of Stator Winding Resistance

The analytical calculation of the stator winding resistance of the reference AFM can be calculated using

$$R_{DC} = \frac{4 \cdot l_c \cdot \rho}{\pi d_{strand}^2 \cdot N_{strand}} \tag{3.3}$$

where,
R_{DC} - Resistance of the coil
l_c - Length of the coil [m]
ρ - Resistivity of the coil [Ωm]
d_{strand} - Diameter of each strand [m]
N_{strand} - Number of parallel copper strands

The resistivity of the copper at 20^oC, ρ_{cu}= $1.72 \times 10^{-8}\Omega - m$. The diameter of a single copper strand was measured using a vernier caliper to $0.9mm$. Assuming the insulation thickness to be $20\mu m$, the diameter of the copper strand is reduced to $0.88mm$.

Determination of number of turns

The number of turns is determined by physically inspecting the dismantled parts of the reference AFM. As shown in Figure 3.13, the round copper strands inside the slot are separated by an insulation layer indicating a double-layer winding. Each layer in a slot has 120 round copper strands and each phase has 12 parallel strands in each stator as in Figure 3.13. Hence, the number of turns N_t is determined to be 10.

Determination of length of winding

The winding length of a single coil is estimated as in Figure 3.14. The coils are wound around the tooth body and the average length of the copper strand, l_c is determined by measuring the dimension of the stator tooth body.

The trapezoidal shape of the wound coil is divided into segments for convenience, and these segments are labeled as G, H, & C with the sub-dimensions

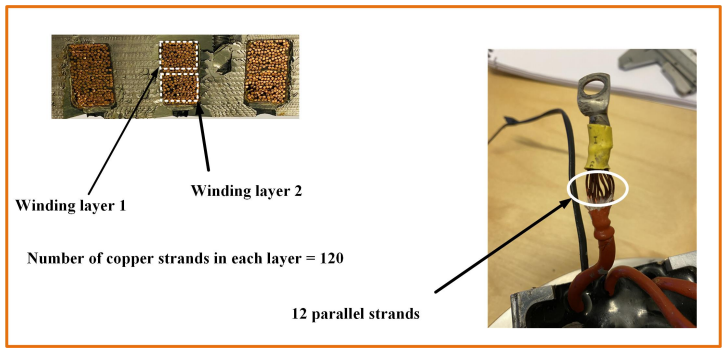

Figure 3.13: Winding layer and number of turns. There are 120 copper strands in each layer. There are 12 parallel strands in each coil.

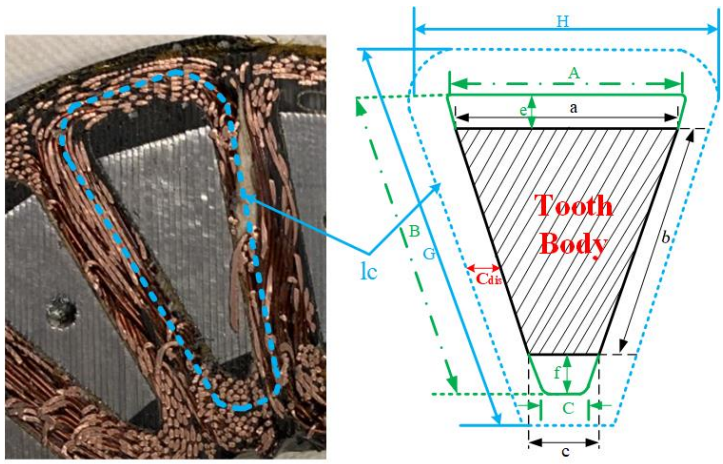

Figure 3.14: Single coil

as shown in Figure 3.14. The average length of the coil is calculated as,

$$\begin{aligned} l_c &= 2 \cdot G + H + C \\ &= 2 \cdot (B + 2 \cdot C_{dis}) + (A + 2 \cdot C_{dis}) + C \\ &= 2 \cdot (e + f + b + 2 \cdot C_{dis}) + (A + 2 \cdot C_{dis}) + C \end{aligned} \tag{3.4}$$

The dimensions C_{dis}, e, f, b, A, *and* C parameter values are tabulated in

Table 3.5: Coil details

Parameter	Values
Resistivity of copper at 20^oC, ρ_{cu}	$1.72 \times 10^{-8}\Omega - m$
Diameter of a single copper strand, d_{strand}	$0.88\ mm$
Number of strands, N_{strand}	12
Dimensions of the length of the coil:	
e	$6\ mm$
f	$4\ mm$
b	$36\ mm$
C_{dis}	$3\ mm$
A	$20\ mm$
Length of single coil, l_c	$0.133\ m$
Number of turns, N_t	10
Number of parallel branches, N_p	1

Table 3.5

The DC resistance of a single coil can thus be calculated using (3.3) to,

$$\begin{aligned} R_{sc} &= \frac{4 \cdot N_t \cdot l_c \cdot \rho}{N_p \cdot \pi d_{strand}^2 \cdot N_{strand}} \\ &= \frac{4 \cdot 10 \cdot 0.133 \cdot 1.72 \times 10^{-8}}{1 \cdot \pi \cdot \left(0.88 \times 10^{-3}\right)^2 \cdot 12} \\ &= 3.06 m\Omega \end{aligned} \tag{3.5}$$

With the calculation of the resistance of a single coil, the per-phase stator winding resistance can be found as

$$R_s = \frac{R_{sc} \cdot Q_s}{m} = \frac{3.06 \times 10^{-3} \cdot 18}{3} = 18.36m\Omega \tag{3.6}$$

where,
R_{sc} is the single coil resistance
Q_s is the number of stator slots
m is the number of phases

Hence, the percentage difference between the calculated and measured stator winding resistance per phase is less than 1%.

3.3.3 Length of the Coil from Measured Resistance

This section determines the coil length from the measured phase resistance, $R_{ph} = 18.2m\Omega$. From the previous section, some of the investigated and calculated parameters are used in determining the length of the coil,

Number of slots per phase S_{ph},

$$S_{ph} = \frac{Q_s}{m} = \frac{18}{3} = 6 \tag{3.7}$$

Number of coils per slot, C_s=1

Number of coils per phase C_{ph},

$$C_{ph} = C_s \cdot S_{ph} = 1 \cdot 6 = 6 \tag{3.8}$$

Resistance per coil around one tooth R_{sc},

$$R_{sc} = \frac{R_{ph}}{C_{ph}} = \frac{0.0182}{6} = 3.03m\Omega \tag{3.9}$$

Copper area in the slotA_{cu},

$$A_{cu} = a_{cond} \cdot N_t \cdot N_l \tag{3.10}$$

The cross-section area of the conductor in the slot a_{cond},

$$a_{cond} = \frac{1}{4}\pi \cdot d_{strand}^2 \cdot N_{strand} \tag{3.11}$$

where,
d_{strand}-Diameter of single strand,
N_{strand}-Number of copper strands per phase
N_t-Number of copper strands in each layer of winding in a slot
N_l-Number of layers
Combining (3.10) and (3.11)

$$A_{cu} = \frac{1}{4}\pi \cdot d_{strand}^2 \cdot N_{strand} \cdot N_t \cdot N_l = 145.97\ mm^2 \tag{3.12}$$

Total length of the coil with $\rho = 1.72 \times 10^{-8}\Omega m$,

$$l_c = \frac{R_{sc} \cdot A_{cu,w}}{\rho} = 12.87\ m \tag{3.13}$$

Length of single copper strand L_{sc},

$$L_{sc} = \frac{l_c}{N_{c,strand}} = 0.107\ m \tag{3.14}$$

where, $N_{c,strand}$ is the number of copper strands in each layer

The volume of the copper per coil V_{cu}

$$V_{cu} = L_{sc} \cdot A_{cu,w} = 7831.69\ mm^3 \tag{3.15}$$

Calculating the copper volume will serve to validate the copper volume in the 3D FEM model.

3.3.4 Slot Area and Fill Factor

From the investigation on the reference AFM the dimensions of the slot shown in Figure 3.10 are used to determine the slot area A_s

$$A_s = \frac{B_{s1} + B_{s2}}{2} \cdot H_{s2} + (B_{s2} - 2R_s)\, R_s + \frac{\pi}{2} R_s^2 = 230.38\ mm^2 \tag{3.16}$$

and the slot fill factor k_{slot},

$$k_{slot} = \frac{A_{cu}}{A_s} = 0.63 \tag{3.17}$$

The winding details such as winding resistance, area of the slot, slot fill factor, number of winding turns, and other winding-related information from the previous section are tabulated for the DSSR machine configuration in Table 3.6.

3.4 Experimental Set up

Open-circuit and load tests were performed on the AFM-3. The three-phase voltages and currents are recorded for different operating speeds $500rpm$, $1000rpm$, and $1500rpm$.

3.4.1 Test Set up

In this section, the test up is explained and further details can be referred to [15]. The experimental set-up on the AFM side includes a 114V/110A EV inverter with a CAN interface. The CAN analyzer tool establishes communication between the inverter and the test machine. The inverter on the AFM side is powered by a DC power supply of 300V/20A. The motor controller also uses another auxiliary DC power supply of 12V. The test set-up is as shown in Figure 3.15. The DC machine and the AFM are mechanically coupled.

The DC motor is operated using a $\pm 440V/\pm 25A$ thyristor converter placed in a power panel in Figure 3.15. The voltage and current measurements are recorded with voltage and current sensors mounted on the power panel with a maximum value of $\pm 650V$ and $\pm 35A$.

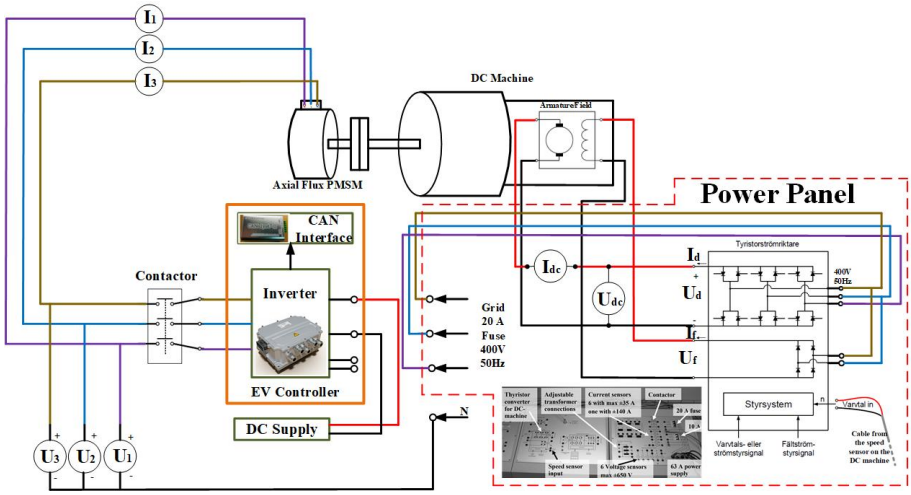

Figure 3.15: Experimental set-up

While conducting the open-circuit test, the DC motor drives the AFM. During the load test, the AFM drives the DC machine. The experimental connection for the load test is very much the same as the open-circuit test, except that the AFM inverter is turned ON. The motor is loaded by increasing the negative armature current of the DC machine. The operating speed of the AFM and the DC machine is controlled by the inverter. The three-phase terminal voltage and three-phase currents on the AFM side are recorded for varying torque and speeds. The measured quantities for both the open-circuit test and load test on the DC machine side are U_{dc} and I_{dc} (i.e. armature current and armature voltage). On the AFM side the measured quantities are three phase voltages U_1, U_2, U_3 and three phase currents I_1, I_2, I_3. The measured three-phase current is the total current of the double stator AFM as seen in Figure 3.1. The two stators of the AFM are connected in parallel, where one of the phase winding connection diagrams is on the right side of the connection diagram in Figure 3.16.

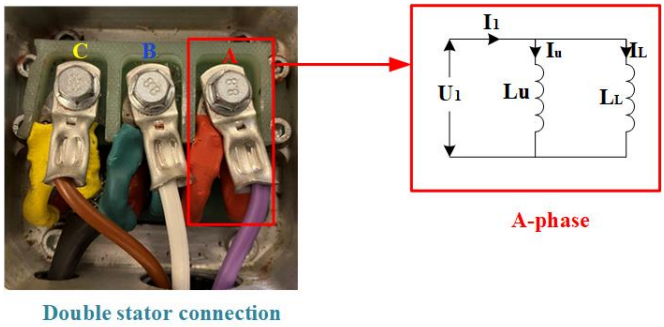

Figure 3.16: Double stator connection diagram of the AFM. U_1-phase voltage, I_1-phase current, L_u-upper stator winding, L_L- lower stator winding, I_u- current in upper stator, I_L- current in lower stator

3.4.2 Power Flow in the Load Test

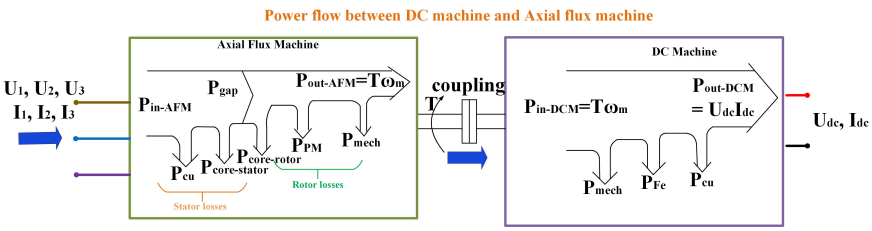

Figure 3.17: Power flow during load test

The power flow diagram shown in Figure 3.17, shows the power flow between the DC machine and the AFM. While performing the load test, the torque produced from the DC machine is fed as input to the AFM.

3.5 Measurement Results and Material Selection

The results from both the no-load and load tests were compared with the corresponding FEM simulation results as shown in section 4.4.1, and they matched fairly well. The flux linkage, induced voltage, and torque plots shown in Figures 4.12 and 4.13 are consistent with the FEM simulations, validating the accuracy of the FEM models. However, slight discrepancies between the

experimental and simulation results were observed, which can be partially attributed to the unknown material properties of the lamination and PMs. These materials were chosen based on the best available data, but their actual properties might differ, influencing factors like the magnetic flux density and torque production. These variations in material properties could account for the differences, highlighting the need for more precise material data for a more accurate prediction of the AFM performance. Due to issues with the drive unit in the experimental setup, while performing the load test, while the induced voltage versus time was not fully accurately measured because the measured points of the induced voltage were slightly misaligned regarding the periodicity. Therefore the load angle could not be determined (thus i_d and i_q could not be specified). However, the reluctance torque component was found in simulations (not presented here) to be negligible. Still, it was found that the calculated torque results from the captured induced voltage showed good agreement with the FEM simulations. The core material data used in the FEM model can be found in [16] a comprehensive summary of the material properties is included in Appendix C for convenient reference, and the PM material is discussed and chosen in section 4.4.1.

Table 3.6: Winding details

Parameter	Value
Number of pole pairs, p	8
Number of stator slots per stator, S_s	18
Number of winding layers, N_l	2
Number of turns, N_t	10
Number of parallel branches, N_p	1
Number of coils per phase, N_c	12
Number of Slots per phase, S_{ph}= $\frac{S}{m}$	$\frac{18}{3} = 6$
Calculated stator winding resistance per phase, R_s	18.36 $m\Omega$
Resistivity of copper at 20^oC ρ_{cu}	$1.72 \times 10^{-8}\Omega - m$
Analytically calculated length of the coil l_c	0.133 m
Number of slots per pole S_s, S_s/p	1.125
Number of slots per pole per phase, $q = \frac{S_s/p}{m}$	0.375
Copper area in each layer per slot $A_{cu,w}$	73 mm^2
Total length of single strand in a coil , l_c	12.87 mm
Average length of coil,L_c	133 mm
Volume of copper in each coil V_{cu}	7831.69 mm^3
Cross section area of coil a_{cond}	$0.608mm^2$
Area of copper in slot, A_{cu}	$145.971mm^2$
Slot area, A_s	$230.38mm^2$
Slot fill factor, k_{slot}	0.63

CHAPTER 4

Building of 3D and 2D Models of Axial Flux Machines

This chapter introduces the structured development of Axial flux machine models in 3D and 2D beginning with an overview of machine model creation followed by a detailed examination of key aspects, including geometric modeling, electromagnetic field analysis, and system parameterization, thereby presenting fully reproducible AFM models.

4.1 Structured Development of Axial Flux Machine Models

A model of the reference AFM presented in the previous chapter is built in the ANSYS Maxwell software 2023 R1 and evaluated. Using the FEM. The main flux path is in the axial and radial direction, flowing from the PM to the stator tooth axially through the air gap and radially to the consecutive tooth as in Figure 4.1 which shows a cut-out surface of the 3D machine model shown in Figure 4.3, along the work-plane in the center of the air gap. If also the end leakage flux is to be considered, together with the tapered shape of the stator teeth and magnets then a 3D FEM model is preferred over 2D

modeling because the flux path is in every dimension along the axial, radial, and tangential direction. Hence, the geometry of the AFPM is centralized around the z-axis in cylindrical coordinates as shown in Figure 4.2, and the rotor rotates around the z-axis in $\pm\theta$ direction.

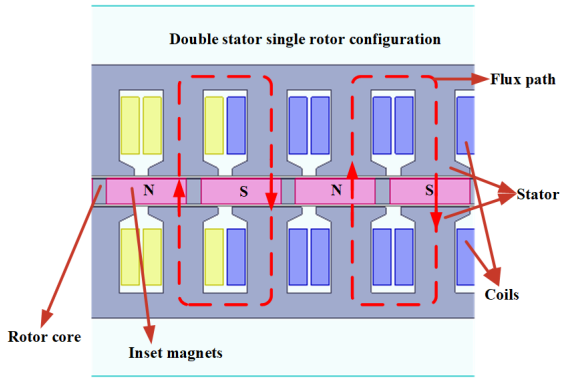

Figure 4.1: Flux path of the axial flux machine

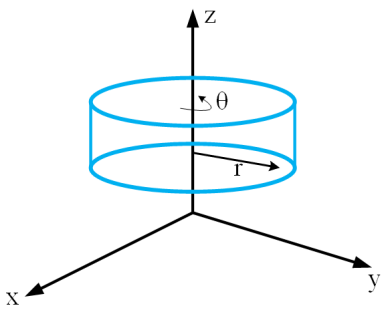

Figure 4.2: AFPM machine in cartesian and cylindrical coordinate system

The electromagnetic field problems are solved with Maxwell's equations in a finite region of space with appropriate boundary conditions. In the 3D maxwell design, the reference AFM dimensions are declared as variables. The reference machine is modeled using built-in templates in the Ansys Maxwell software referred to as user-defined primitives.

The FEM AFPM with double stators and a sandwiched rotor with concentrated windings is as shown in Figure 4.3. The rotating parts of the machine are enclosed within a band object since it is necessary to have all moving objects as one rigid body with a single force acting on the assembly. The complete machine model is covered by a region to create a boundary so that the solution domain is defined and the region restricts the flux within the solution region.

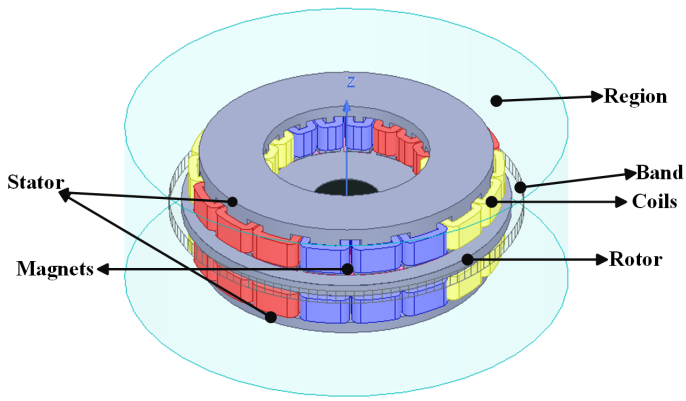

Figure 4.3: FEM model

The long computation time for solving the full 3D model is not a viable option. Hence, to reduce computation time, a symmetric piece of the machine is simulated. The machine's symmetry is based on the number of stator/rotor slot/pole combinations. For the reference AFM model with the existing number of slots and poles, one-quarter of the whole machine is used for computation as shown in Figure 4.4.

To complete the flux path, necessary boundary conditions must be applied to the reduced model. The necessary boundary conditions used in the existing reference AFM model are matching and symmetry boundary conditions. The matching boundary condition comprises of the independent and dependent boundary conditions. The applied boundary conditions are as shown in Figure 4.4. The symmetry boundary condition restricts the flux to be normal to the surface. The Ansys Maxwell software solvers give room to perform

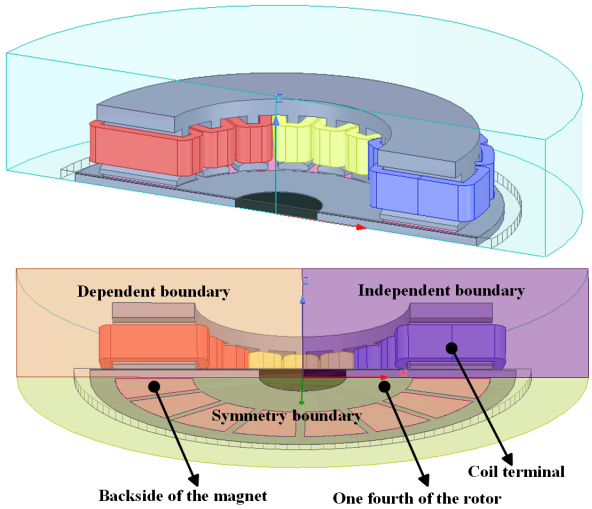

Figure 4.4: Split model of AFM

magneto-static and transient studies.
The variables for the 3D reference machine model are seen in Appendix A. These measurements and parameterized quantities are used to create the 3D AFM model. Since Maxwell separates the moving and the non-moving objects, all moving objects like the rotor core and the attached magnets are housed within the cylindrical band object as in Figure 4.5. Having all the moving objects within the band helps in forming one single moving object group. The outer surface of the band is divided into segments, with each segment ranging from 1° - 5° in ANSYS Maxwell software. The segmentation of the band is determined by the segmentation angle, calculated as 360° divided by the number of time steps. These outer surface segments in the band can range from 72 to 360 segments. The purpose of defining the outer segments is to synchronize the time steps with the rotation of the machine. In transient simulations, time steps represent discrete intervals at which calculations are performed. These calculations track how electromagnetic fields, currents and other parameters change as the rotor moves. The synchronization of the time steps with band segmentation is impertinent. If the time steps are too large compared to the angular displacement, the model might end up missing important changes in the electromagnetic field.

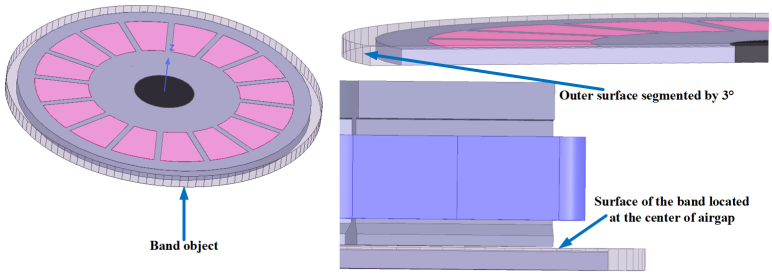

Figure 4.5: Creating a band object

4.2 Transformation of 3D to 2D Model

The 3D model of the AFM is converted into a 2D model, simplifying the machine's representation as a 2D planar problem. In this transformation, the third coordinate is treated as depth, which helps streamline the geometry and reduce computational complexity. Various transformation methods are discussed in the literature, and in this work the 2D LMMA is employed. This section outlines the steps involved in converting the 3D model to the 2D model as illustrated in Figure 4.6.

The computational plane is located along the average radius. The cross-section area along the XY and XZ plane of the 3D FEM model are compared with the equivalent 2D model tabulated in Table 4.1.

4.3 Dimension Parametrization of 3D and 2D Axial Flux Machine Model

Dimension parameterization refers to the process of defining the physical dimensions and geometrical attributes of machine components using a set of parameters. This approach helps in creating flexible and adaptable models where dimensions can be easily modified without rebuilding the entire design. Dimension parameterization allows quick evaluation of different design variations to achieve the best performance.

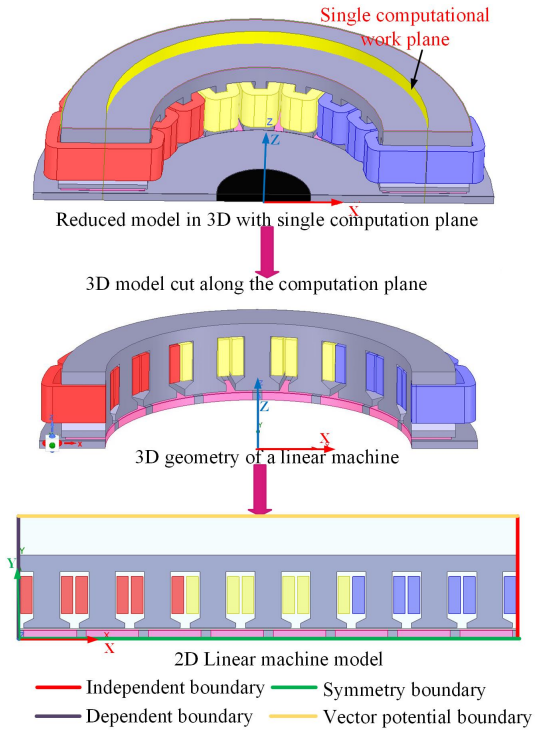

Figure 4.6: Process of transforming a 3D model to a 2D; yellow curved sheet is the computational plane used to form the 2D model

By parameterizing dimensions such as rotor diameter, stator length, airgap width, and slot dimensions, one can systematically study the effects of changing these variables on the machine's electromagnetic behavior.

4.3.1 3D Model Dimension Parameterization

Parameterization involves defining the geometry and dimensions of a model using a set of independent and dependent variables.

Table 4.1: Comparison of cross-section areas

Part of the motor	3D model	2D model
Along XY plane for 3D model and along depth for 2D model		
Stator tooth body[a]	385 mm^2	364 mm^2
Stator tooth rim[a]	674 mm^2	636 mm^2
Single magnet	733 mm^2	733 mm^2
Rotor core[b]	7,180 mm^2	1,090 mm^2
Along XZ plane for 3D model and along XY plane for 2D model		
Stator cross-section	3,840 mm^2	3,840 mm^2
Coil cross-section	73 mm^2	73 mm^2
Single magnet	75 mm^2	75 mm^2
Rotor core	112 mm^2	112 mm^2

[a]difference is due to the selection of depth = magnet length

[b]active part alone in the 2D model in the radial direction

Independent Variables

Independent variables are the primary parameters that the designer directly controls. They represent key dimensions or attributes that can be freely adjusted to alter the design. The independent variables of the 3D model are listed in Table 4.2 along with the slot dimensions in Table 3.4.

Dependent Variables

Dependent variables are calculated or derived based on the values of the independent variables. These geometric constraints or relationships maintain the model's consistency and functional integrity.

The 3D model, necessitates the parameterization across all three coordinate axes. Initially, the dependent variables are parameterized in the XY-plane. The view of the outer and inner diameters and radius of the stator core and

Table 4.2: 3D model parameterization - independent variables

Description	Parameter
length of the magnet in x-direction	L_{mag}
Length of tooth in x-direction	L_{tooth}
Outer diameter of magnet	OD_{mag}
Inner diameter of magnet	ID_{mag}
Outer diameter of rotor core	OD_{rotor}
Inner diameter of rotor core	ID_{rotor}
Thickness of the magnet	Th_{magnet}
Core spacing between the magnets	$W_{mag,core}$
Number of stator slots	S_s
Number of poles	p
Stator slot opening	$Bs0$
Angle near slot opening	S_α
Slot height	$Hs2$
Height of slot opening	$Hs0$
Depth of stator core	d_s
Width of stator slot	W_{ss}
Cross section area of coil	A_c

magnets are depicted in Figure 4.7. The following set of equations establishes the dependent variables, which are calculated or expressed in terms of the independent variables for the variables in Figure 4.7.

Radius of the work plane,

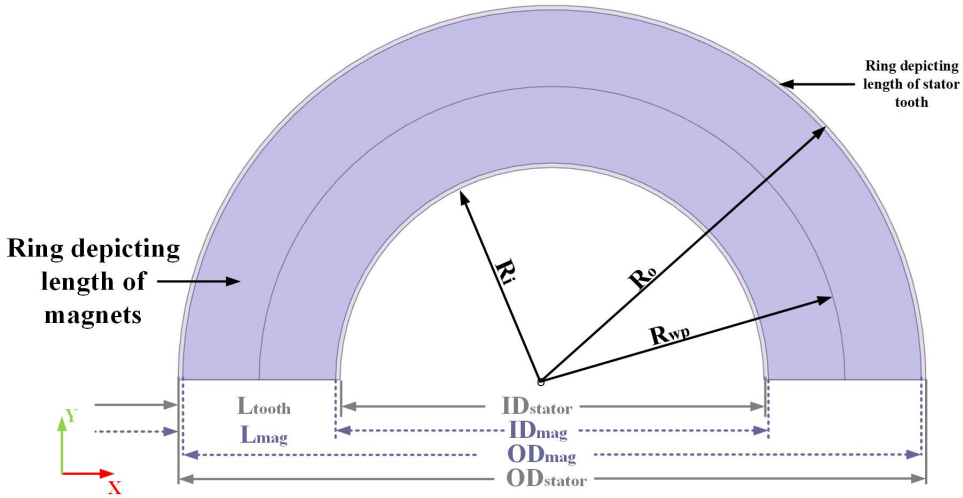

Figure 4.7: Diameter and radius of the machine, defined with a focus on the stator core and magnets to establish key parameters

$$R_{wp} = \frac{OD_{mag} - ID_{mag}}{4} + \frac{ID_{mag}}{2} \tag{4.1}$$

Inner radius of the stator core,

$$R_i = R_{wp} - \frac{L_{tooth}}{2} \tag{4.2}$$

Outer radius of the stator core,

$$R_o = R_{wp} + \frac{L_{tooth}}{2} \tag{4.3}$$

Outer diameter of the stator core,

$$OD_{stator} = R_o \cdot 2 \tag{4.4}$$

Inner diameter of the stator core,

$$ID_{stator} = R_i \cdot 2 \tag{4.5}$$

The variables for the stator slot, tooth, and coils are parameterized based on the independent slot variables, as shown in Table 3.4. These variables are

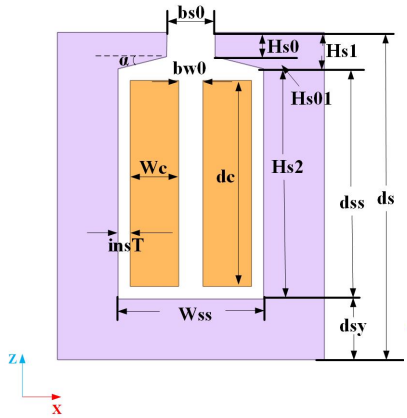

(a) Dependent variables in the slot

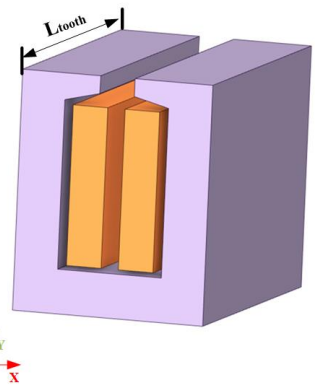

(b) Length of the tooth

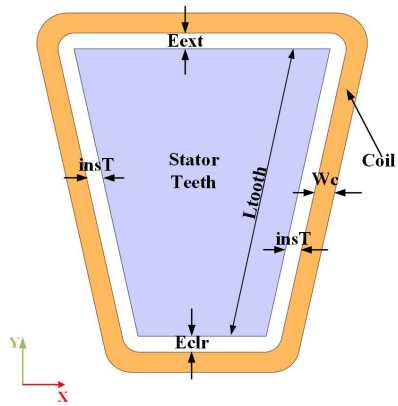

(c) Dependent variables for tooth and coil

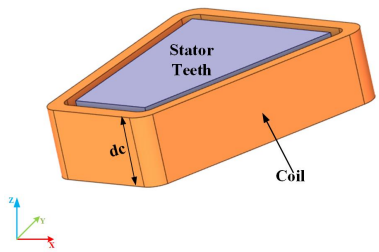

(d) Depth of the coil

Figure 4.8: Dependent variables of the stator tooth, slot and coil

depicted in Figure 4.8.
The variables of the stator slot seen in Figure 4.8a are parameterized in the following equations:

Depth of the stator core,

$$d_s = d_{ss} + d_{sy} \tag{4.6}$$

where, the d_{ss} and d_{sy} are determined from slot dimensional parameters.

$$d_{ss} = Hs0 + Hs01 + Hs2 = Hs1 + Hs2 \tag{4.7}$$

$$Hs1 = Hs0 + \frac{w_{ss} - bs0}{2} \cdot \tan(\alpha) \tag{4.8}$$

$$d_{sy} = d_s - d_{ss} \tag{4.9}$$

The variables linked to the concentrated coil of the machine model are as shown in Figure 4.8c parameterized with the variables in the XY plane.

$$OD_{coil} = \left(\frac{OD_{stator}}{2} + E_{ext} + W_c\right) \tag{4.10}$$

$$OD_{coil,i} = \left(\frac{OD_{stator}}{2} + E_{ext}\right) \cdot 2 \tag{4.11}$$

$$ID_{coil} = \left(\frac{ID_{stator}}{2} - E_{clr} - W_c\right) \cdot 2 \tag{4.12}$$

$$ID_{coil,i} = \left(\frac{ID_{stator}}{2} - E_{clr}\right) \cdot 2 \tag{4.13}$$

$$W_c = \frac{W_{ss} - 2 \cdot ins_T - bw0}{2} \tag{4.14}$$

$$d_c = d_{ss} - Hs1 - 2 \cdot ins_T \tag{4.15}$$

$$A_{coil} = W_c \cdot d_c \tag{4.16}$$

4.3.2 2D Model Dimension Parameterization

Some of the independent and dependent variables from the 3D model are also used in developing parameterization of the 2D model. The parameterization of the 2D model is structured by sequentially linking variables to the stator, coils, rotor, and magnets. The parameterization of the 2D model begins with positioning the work plane, which passes through the center of the magnets and (4.1) defines the radius of the work plane R_{wp}. In the 2D model, the overall length along the y-axis of the machine depends on the radius of the work-plane R_{wp} and the arc length of the work plane for 180^o,

$$arc_{wp} = \pi \cdot R_{wp} \tag{4.17}$$

Thickness of the yoke,

$$Th_{yoke} = Th_{stator} - (Hs2 + Hs1 + Hs0 + Rs) \tag{4.18}$$

Total height of the machine in z-direction,

$$H_z = Th_{mag} + l_{gap} + Th_{stator} \tag{4.19}$$

Width of the 2D model,

$$W_{2D} = \pi \cdot R_{wp} \tag{4.20}$$

The section of the rotor of the 3D model is shown in Figure 4.9, and the angles of the rotor core and magnet are parameterized as

$$\alpha_{core} = 2 \cdot arcsine \left[\left(\frac{W_{mag,core}}{2} \right) / R_{wp} \right] \cdot \frac{180}{\pi} \tag{4.21}$$

$$\alpha_{magnet} = \frac{360^o}{p} - \alpha_{core} \tag{4.22}$$

The width of the space between the magnets and the width of the magnets in the 2D model is found from the angles as in (4.21) and (4.22) to be

$$W_{core} = R_{wp} \cdot \alpha_{core} \cdot \frac{\pi}{180} \tag{4.23}$$

$$W_{magnet} = R_{wp} \cdot \alpha_{magnet} \cdot \frac{\pi}{180} \tag{4.24}$$

Similar to the rotor parameterization, the stator tooth and slot are also

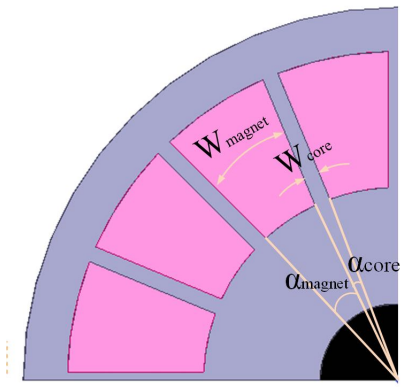

Figure 4.9: Dimensions used for the 2D model

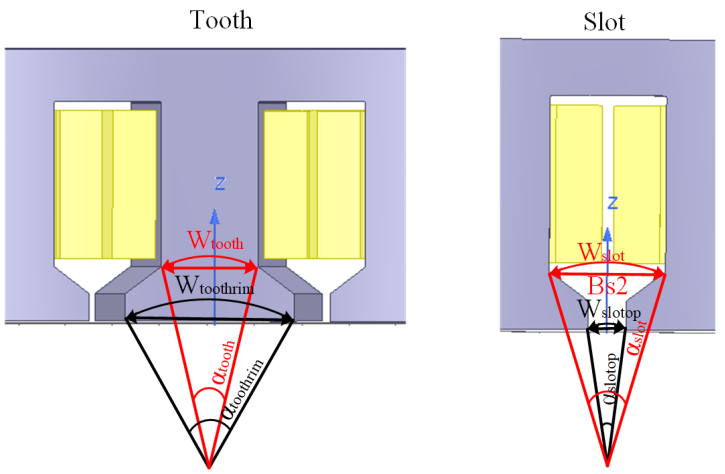

(a) Variables in the tooth

(b) Variables in the slot

Figure 4.10: Variables in a stator tooth and slot

parameterized, with variables supporting the parameterization shown in Figure 4.10: Angle formed from the arc length of the slot,

$$\alpha_{slot} = 2 \cdot arcsine \left[\left(\frac{Bs1}{2} \right) / R_{wp} \right] \cdot \frac{180}{\pi} \tag{4.25}$$

Angle formed from the arc length of the tooth,

$$\alpha_{tooth} = \frac{360^o}{S_s} - \alpha_{slot} \tag{4.26}$$

Angle formed from the arc length of the slot opening,

$$\alpha_{slotop} = 2 \cdot arcsine \left[\left(\frac{Bs0}{2} \right) / R_{wp} \right] \cdot \frac{180}{\pi} \tag{4.27}$$

Angle formed from the arc length of the tooth rim,

$$\alpha_{toothrim} = \frac{360^o}{S_s} - \alpha_{slotop} \tag{4.28}$$

Arc length of the slot,

$$W_{slot} = R_{wp} \cdot \alpha_{slot} \cdot \frac{\pi}{180} \tag{4.29}$$

Arc length of the tooth,

$$W_{tooth} = R_{wp} \cdot \alpha_{tooth} \cdot \frac{\pi}{180} \tag{4.30}$$

Arc length of the slot opening,

$$W_{slotop} = R_{wp} \cdot \alpha_{slotop} \cdot \frac{\pi}{180} \tag{4.31}$$

Arc length of the tooth rim,

$$W_{toothrim} = R_{wp} \cdot \alpha_{toothrim} \cdot \frac{\pi}{180} \tag{4.32}$$

The coil dimensional variables are parameterized with those depicted in Figure 4.11. The shape of the coil is rectangular hence, cross-section area of the coil,

$$A_{coil} = L_{coil} \cdot W_{coil} \tag{4.33}$$

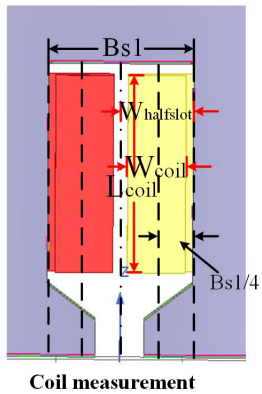

Figure 4.11: Coil variables

The conductor dimensions are calculated based on the copper area of the physical machine.
Angle of the arc length of half of the slot,

$$\alpha_{slotcoil} = 2 \cdot arcsine \left[\left(\frac{Bs1}{4} \right) / R_{wp} \right] \cdot \frac{180}{\pi} \tag{4.34}$$

Angle of the arc length of the coil,

$$\alpha_{coil} = \frac{360^o}{N_{slot} \cdot 2} - \alpha_{slotcoil} \tag{4.35}$$

Arc length of the coil,

$$W_{coil} = R_{wp} \cdot \alpha_{coil} \cdot \frac{\pi}{180} \tag{4.36}$$

Width of half of the slot,

$$W_{halfslot} = R_{wp} \cdot \alpha_{slotcoil} \cdot \frac{\pi}{180} \tag{4.37}$$

Length of the coil,

$$L_{coil} = \frac{A_{coil}}{W_{coil}} \tag{4.38}$$

The equations for the coordinates used in constructing the 3D model of the stator, along with the coordinate equations for the complete 2D model are detailed in the appendix D and E.

4.4 The 3D FEM Simulations and Measurements

4.4.1 No-Load and Load Test Results

In this study, both open-circuit and load tests were conducted to analyze the flux linkage, induced voltage, and torque characteristics of the AFPM machine at 500 rpm, 1000 rpm, and 1500rpm, as seen in Figures 4.12 and 4.13. The open-circuit test provides insight into the machine's flux linkage as shown in Figure 4.12a calculated from the induced voltage in Figure 4.12b. However, the load test shown in Figure 4.13 reveals the machine's performance under mechanical load, showing how the torque output, correlates with the applied load at rotational speeds of 500 rpm, 1000 rpm, and 1500 rpm.

The results of the open-circuit test showed an increase in the induced voltage with speed, consistent with the expected behavior of the machine as the rate of change of flux increases.

Since the magnet and the core materials are unknown, the core material was assumed, and two magnet materials with lower and higher BH values were selected. NdFeB-33UH (used for the simulations presented in Figure 4.12 and Figure 4.13) has a higher BH value and NdFeB-28ah has a lower BH value. The comparison of the magnitude of induced voltages is tabulated in Table 4.3, showing that the induced voltage in the reference machine is 10% lower than the 3D FEM model when the NdFeB-33UH is selected as magnetic material. When NdFeB-28ah is selected as the magnetic material, the induced voltage in the reference machine is 2% lower than the 3D FEM model.

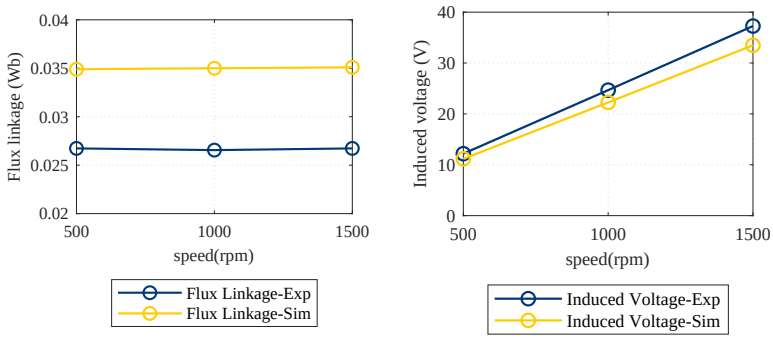

(a) Flux linkage versus speed

(b) Induced voltage versus speed

Figure 4.12: Comparison of experimental and FEM open-circuit test results

Table 4.3: Comparison of the back emf of the reference machine with 3D FEM model

Measurements	Induced voltage (V)
Ref. machine	12.2
3D model- NdFeB-33UH	13.6
3D model- NdFeB-28ah	12.5
%Difference	
% Diff. 3D-NdFeB-33UH	10.6 %
% Diff. 3D-NdFeB28ah	2.4%

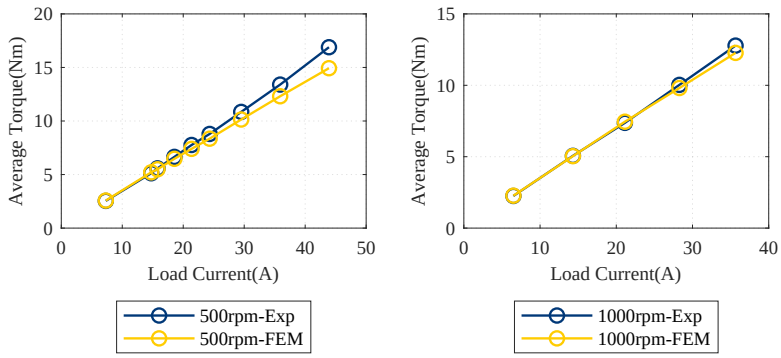

(a) Load Torque versus current at $500rpm$

(b) Load Torque versus current at $1000rpm$

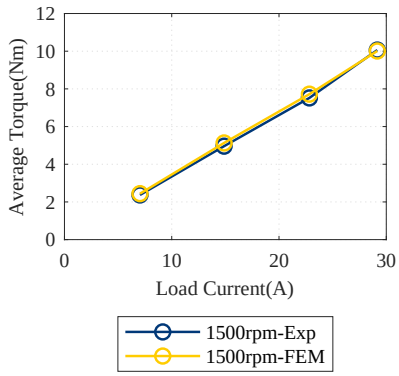

(c) Load Torque versus current at $1500rpm$

Figure 4.13: Comparison of experimental and FEM of load torque for varying speeds

CHAPTER 5

2D and 3D Modeling Resolution and Sensitivity Analysis

This chapter offers an in-depth analysis of mesh generation, time step selection, and the comparative study of 3D and 2D models in FEM analysis of AFMs, while specifically comparing the representation of end leakage flux.

5.1 Mesh Density Variation

In this section, an attempt is made to compare the 3D and 2D models in the context of electromagnetic simulations, focusing on the resolution which includes variation in mesh element size, particularly for flux linkage, induced voltage, torque, and losses.

The 3D model represents the full geometry of the axial flux machine and the spatial resolution variation in 3D. This allows for a detailed analysis of complex interactions between components like stator, rotor, and air gap. Hence variation in all three dimensions helps in a comprehensive understanding of the machine's performance. However, the 2D model simplifies the geometry, visualizes mostly in the form of a planar object, and does not capture all 3D effects. The 3D models need higher mesh density to accurately resolve the

detailed geometries and field variations throughout the volume. However, the 2D models can have a lower mesh density since they represent a cross-section of the 3D model and do not capture all the complexities of the 3D interactions.

Design and evaluation of electrical machines are commonly built upon electromagnetic Finite Element Analysis (FEA). However, FEA does not guarantee accurate results by default. The numerical inaccuracies associated with electromagnetic FEA can be mitigated by carefully adjusting the mesh resolution. The meshing process is crucial in numerical simulations.

Table 5.1: Maximum length of mesh element size

Machine part	Mesh element size 3D	Mesh element size 2D
Coils	8 mm	5 mm
Band	30 mm	5 mm
Band surface	3 mm	2 mm
Magnet layer	1 mm	2 mm
Magnet surface	2 mm	1 mm
Magnets	5 mm	5 mm
Region	40 mm	40 mm
Rotor	20 mm	5 mm
Rotor layer	10 mm	2 mm
Stator	15 mm	10 mm

The volume and geometry of a 3D model is complex. The mesh elements in 3D are tetrahedral and must resolve variations across all three dimensions. However, the mesh elements in 2D are triangular.

Mesh scaling is performed to maintain a similar spatial resolution between the 3D and 2D models. In a 2D model, the geometry is simplified (e.g., assuming symmetry in the z-direction), so the mesh size might be larger compared to a

Table 5.2: Details about the number of mesh elements and computations time in 3D and 2D models

Mesh Type	3D Model		2D Model	
	No. of mesh elements	Computational time (hh:mm:ss)	No. of mesh elements	Computational time (hh:mm:ss)
Extra coarse	105865	02:01:10	3208	00:03:13
Coarse	140640	02:42:08	3872	00:03:41
Medium	353470	09:27:48	5160	00:04:37
Fine	570434	11:41:26	5997	00:05:02
Extra fine	747191	13:00:37	8573	00:06:35

3D model that fully resolves the geometry in all three dimensions. Scaling the mesh element size compensates for the dimensional differences ensuring that flux density and field interactions are resolved comparably in both 3D and 2D.

The mesh element sizing technique involved applying mesh element size variations to all machine parts, by assigning a scaling factor to the element size as shown in Table 5.1 (showing the maximum length of mesh element size for each part, Table 5.2 and Figure 5.1 (showing the five chosen different mesh resolutions; extra coarse, coarse, medium, fine, and extra fine). This study aims to analyze the effects of mesh element sizing under both no-load and rated conditions. It is impertinent to know that at no load, the variation in magnetic field distribution is minimal due to the absence of current driven fields and electromagnetic interactions. A coarse mesh can provide a general view of the magnetic field because the fields are not greatly distorted. However, it may not accurately capture the fields near the edges. In contrast, under rated conditions, the magnetic fields are significantly affected by the high current levels in the winding, which can create a complex field distribution due to the interactions between the stator and rotor. A finer mesh is essential in these conditions to accurately capture the stronger magnetic field and non-linearities caused by the increased load currents. This is especially important in areas like the air gap, where the field lines may become concen-

trated. The number of mesh elements and the computational time for each mesh type for both the 3D and 2D models are tabulated in Table 5.2.

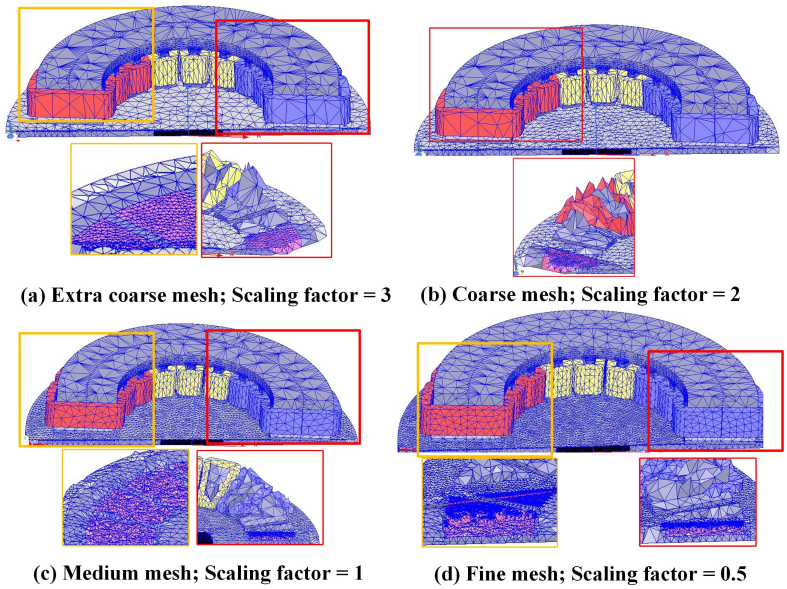

Figure 5.1: Mesh density variation in the 3D model of the AFM

5.1.1 Mesh Density Variation Results

Flux Linkage and Induced Voltage

In Figure 5.3a and 5.3b, the flux linkage and induced voltage from the 3D and 2D models for both no load and rated operating condition are plotted versus the mesh type. It is seen in Figure 5.3a that the flux linkage does not vary much with the mesh density in the 2D model, whereas the 3D shows more variation, both at no load and at rated conditions. A coarse mesh can be used in 2D, and a medium/fine mesh is required in 3D, to get good accuracy. As seen in Figure 5.3b, the induced voltage shows a similar behavior as is seen with the flux linkage. The difference in the ripples of the induced voltage for one phase is plotted against time for the 3D model with varying mesh element sizes, as shown in Figure 5.2.

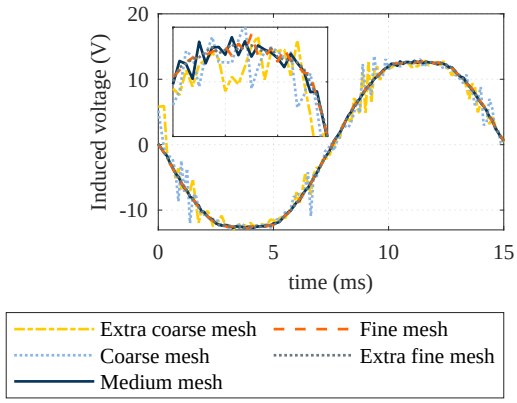

Figure 5.2: Induced voltage versus time for one phase with varying mesh element size

Torque

Figure 5.3c shows the differences in torque between the 3D and 2D models of the AFM for both no load and rated condition. The torque calculation depends on the accurate resolution of the magnetic field distribution in the air gap. Hence the field resolution needs a finer mesh in the air gap. The cogging torque arises from small variations in the magnetic field as the rotor moves relative to the stator teeth. These variations are highly sensitive to the geometric alignment of the rotor and stator, and mesh quality is crucial to capturing these variations. If the mesh is too coarse, the solver may miss important field variations, leading to underestimating or overestimating cogging torque. Thus, edge effects often influence cogging torque, which requires a finer mesh to resolve properly. These effects can become more pronounced when the rotor and stator are closely aligned and a coarse mesh can smooth out these details.

It is seen in Figure 5.3c that the torque does not vary much with the mesh density in the 2D model, whereas the 3D shows more variation, which is mostly visible at rated conditions. At load, the coarse mesh can be used in 2D, and a medium/fine mesh is required in 3D, in order to get good accuracy. At no load, both 3D and 2D models need a finer mesh in the sensitive parts in the air gap of the machine.

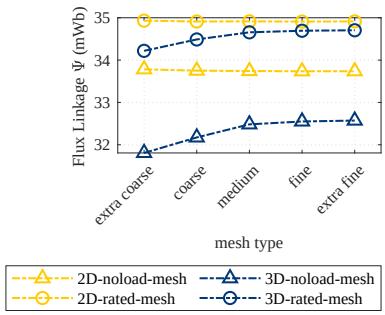

(a) Magnitude of flux linkages

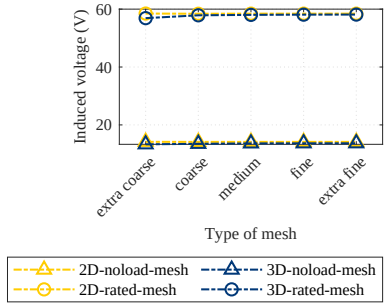

(b) Magnitude of induced voltage of fundamental component

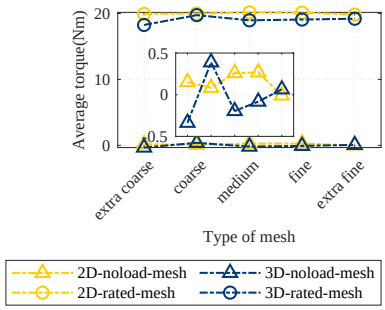

(c) Average Torque

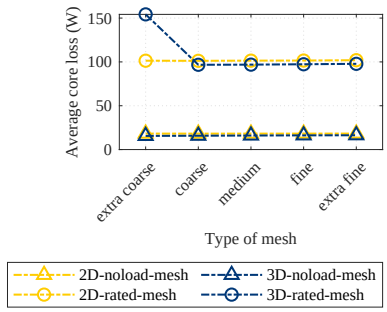

(d) Average core loss for second period

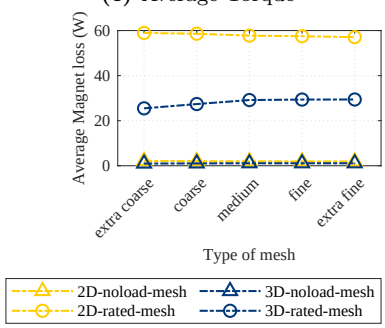

(e) Average magnet loss for second period

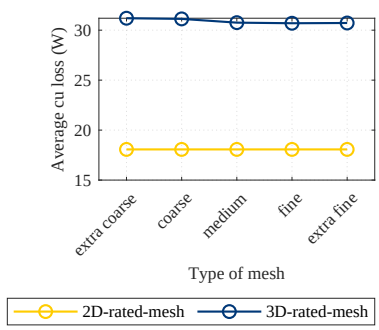

(f) Average copper loss

Figure 5.3: Comparison of the magnitude of flux linkages, average torque, average core loss, and average magnet loss at no load and rated condition of the 3D and the 2D models for varying mesh element length and with 120 time steps per electric period.

Core Loss

The average core losses are as shown in Figure 5.3d. The hysteresis losses are related to the maximum flux density and the shape of the flux waveform. Meanwhile, eddy current losses depend on the rate of change in magnetic flux and the magnitude of flux. Capturing rapid spatial and temporal changes in flux requires fine meshing.

In the 2D model, a medium-mesh type gives good accuracy at no load. Also, at rated conditions, the medium-mesh type seems to be a good choice, as the difference between the loss with the medium mesh and with the fine mesh is around 0.1%, whereas the average core loss between medium and extra fine mesh has a difference of 0.5%. In the 3D model at no load, the average core loss difference between a coarse mesh and a medium mesh is 1.5%, and between the medium mesh and the fine mesh it is 1.2%. Even though it can be seen that the extra fine mesh helps in gaining better accuracy in the 3D model, with a difference of 1.9% compared to the medium-mesh, the higher computational time of the extra fine mesh yields that the fine mesh is not a good option. Similar to the no load results, the average core loss in the 3D model during rated conditions, show a small difference of 0.16% between the coarse and medium mesh is used as compared to a fine mesh but when a comparison was made with an extra fine mesh the difference was 0.95%. Therefore, a medium-mesh appears to be a suitable choice for both 3D and 2D models providing a reasonable computational time for the 3D model.

Magnet Losses

The magnet losses between no load and rated conditions are shown in Figure 5.3e. At no load, the magnet losses are lower because the magnetic field is not changing rapidly resulting in reduced induced current in the magnetic material. In rated conditions, the machine operates at maximum load, and a finer mesh captures a more accurate representation of the magnetic field distribution and its variation over time.

Figure 5.3e demonstrates that magnet losses in both 3D and 2D models are sensitive to variations in mesh density. At no load, the average magnet loss in the 2D model is quite sensitive to mesh density variation, unlike the core

and copper losses. The 2D model with a coarse mesh shows an increase in loss by 3.7% compared to the medium mesh, but the difference in loss decreased by 1% between medium and fine mesh. Further, the magnet loss decreases by 2.4% when comparing the medium mesh and extra fine mesh. But the difference in magnet loss between fine and extra fine mesh is 1.4%. In a 3D model, the magnet loss accuracy varies significantly between each mesh type. The comparison between coarse and medium mesh results in a 6.6% difference, whereas the difference between medium and fine mesh, and medium and extra fine mesh is 0.6% in both cases.

In the rated condition, the 2D model shows a similar trend as in the no-load case where the difference between coarse and medium mesh is 1.4%, medium and fine mesh 0.5% and medium and extra fine mesh 1.2%. However, in the 3D model, the difference between coarse and medium mesh is 6.1%, between medium and fine mesh 0.7%, and between medium and extra fine mesh 0.85%. Magnet losses are significantly more sensitive to variation in mesh density in both 3D and 2D models. Based on the percentage of accuracy, the medium mesh is reasonable for both 3D and 2D models with a reasonable computational time for the 3D model.

Copper Losses

The copper loss in the rated condition is shown in Figure 5.3f. Due to the higher copper volume included in the 3D model, the losses are high compared to the 2D model. The copper losses are not sensitive to mesh element sizes in the 2D model since the mesh only needs to capture the rectangular coil cross-section area. However, in the 3D model the copper losses are quite sensitive to mesh element size variations. As seen in Figure 5.3f, a medium mesh is enough to accurately capture the entire coil shape, including the coil ends, in the 3D model.

5.1.2 Relative Difference between the 3D and 2D Models

As the previous section shows, both 3D and 2D models are sensitive to mesh variations but with varying degrees. This section further investigates how the difference between the 3D and 2D models vary when mesh density is varied, looking again at the flux linkage, induced voltage, torque, and loss

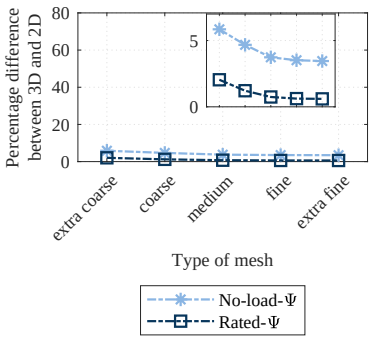

(a) Magnitude of flux linkages

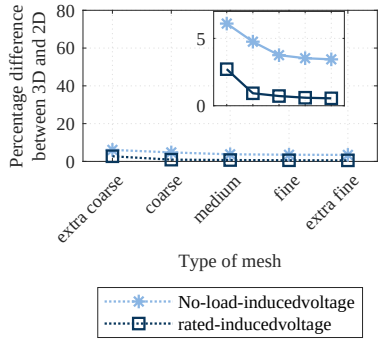

(b) Magnitude of induced voltage

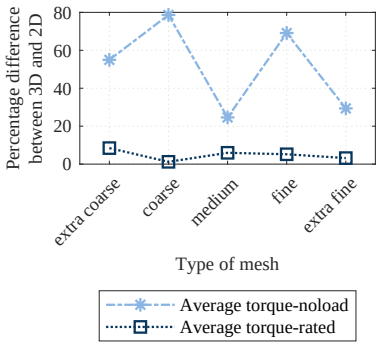

(c) Average Torque

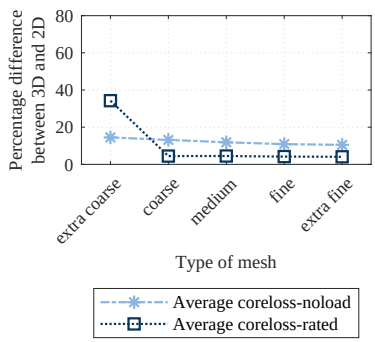

(d) Average core loss

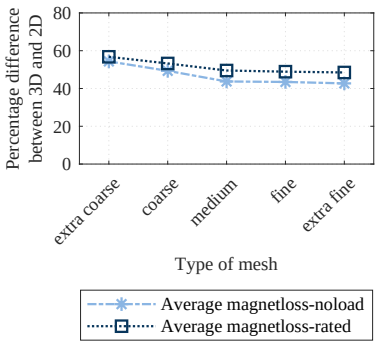

(e) Average magnet loss

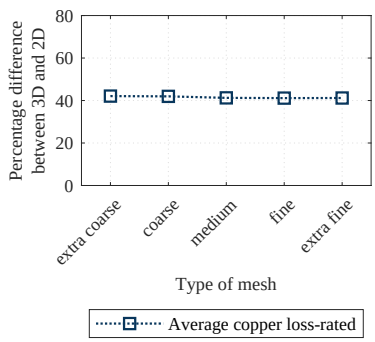

(f) Average copper loss

Figure 5.4: Sensitivity analysis between 3D and 2D model with the mesh element size variation

components. Results are seen in Figure 5.4 which thus shows the percentage difference between the 3D and 2D models for flux linkage, induced voltage, average torque, average core loss, magnet loss, and copper loss.

Flux Linkage and Induced Voltage

The percentage difference between 3D and 2D models with varying mesh density for flux linkage and induced voltage are shown in Figure 5.4a and 5.4b. The differences between the 3D and 2D models in both no-load and rated cases result from variations in mesh as well as the difference in model geometry, since the 2D model do not include the end regions and therefore do not capture end leakage flux, and the 2D model does not capture the tapered shapes of the magnets and stator teeth. As expected, the differences in accuracy for induced voltage are similar to that of flux linkage. In the zoomed-in plots, it can be seen that the discrepancy between 3D and 2D models decreases exponentially with the increase in mesh density. The accuracy of flux linkage and induced voltage improve, and the 2D model results converge slightly towards the 3D model results, reducing the percentage difference. In no load, the differences are higher compared to the rated condition because the no-load flux linkage is lower than the flux linkage at rated operation.

Torque

At no load, the machine's average torque is inconsistent and due to this, the difference in accuracy between the 3D and 2D models is inconsistent with varying mesh density as shown in Figure 5.4c. It can also be seen that increased mesh density might not fully resolve the complexity of the machine's magnetic field at no-load conditions because, as mentioned, 2D models inherently assume a simplified geometry and do not account for axial or off-plane field components that are captured in a 3D simulation. In rated conditions, the differences between the 3D and 2D models are reduced due to more dominant magnetic fields in the presence of load currents.

Core Loss

In Figure 5.4d, the percentage difference between 3D and 2D models with varying mesh density for average core loss is presented. It can be seen that at rated conditions a medium to fine mesh yields a rather small difference

(<10%) between 3D and 2D eddy current and hysteresis loss. In contrast, a coarser mesh can lead to significant inaccuracies in capturing the flux density variations due to which a difference of 40% is observed with the extra coarse mesh. There is an increased difference in core loss between 3D and 2D in no-load (>10%), compared to loss difference at rated conditions (<10%), but the difference in loss between 3D and 2D at no-load is gradually reduced as the mesh is refined, approaching 10%.

Magnet Losses

Magnet losses occur due to time-varying magnetic fields interacting with the magnets' conductive materials. These losses are influenced by spatial variations in the magnetic flux density, dynamic field changes (in rated conditions), and localized hotspots. These localized hotspots can be due to eddy current concentration, especially in areas of high flux density gradients, such as the magnet edges.

In Figure 5.4d, the percentage differences between the 3D and 2D models with varying mesh density for average magnet losses are depicted. In a 3D model, the simulations can fully capture the complex spatial distribution of magnetic fields, accounting for variations in all three dimensions (radial, tangential, and axial). This allows accurate computation of magnet losses due to eddy currents. However, a 2D model simplifies the geometry, reducing it to a cross-sectional view and assuming symmetry or averaging in the third dimension. This might lead to an inaccurate representation of flux variations, and oversimplification of 3D phenomena like fringing effects, leakage flux, and flux density gradients near edges. Hence, 2D models struggle to predict solid losses accurately compared to 3D models. At rated conditions, the field complexity is high, giving localized eddy currents that require a detailed 3D representation to capture the loss accurately. The 2D models cannot represent these complexities, resulting in higher accuracy differences (of 40% to 60%) at rated conditions.

Copper Loss

In Figure 5.4e, it is seen that the percentage difference between 3D and 2D models with varying mesh density for copper loss is roughly the same, around

40%, irrespective of mesh density variation. The difference between 3D and 2D model is due to the geometry of the 2D model neglecting the end part of the windings. The slight improvement with higher mesh density is due to the better geometrical representation of the coil shapes, as mesh density improves.

5.2 Time Step Variation

In this section, the mesh element size is kept constant and time steps are varied. From the studies carried out on variation in mesh density, it is seen that a medium mesh gives good accuracy in both 3D and 2D models. Hence, a medium mesh is used to investigate the impacts due to the variations in the time steps. A shorter time step (in this case $t5 = 360$ steps per electric period is chosen) provides a more detailed capture of these changes, while a longer time step (in this case $t0 = 60$ steps per electric period) provides less resolution but requires less computational effort.

5.2.1 With 3D and with 2D Models

The accuracy of parameters like flux linkage, induced voltage, electromagnetic torque, core losses, magnet losses, and copper losses for no-load and rated cases are analyzed in this section. The time step in the transient simulations defines the frequency at which the software calculates and updates the electromagnetic field values, which includes changes in current, voltage, and magnetic flux distribution over time.

If the time step is too long, the rapid fluctuations that induce eddy currents will not be resolved accurately, especially at rated conditions where the flux changes are more dynamic. The cyclic nature of the magnetic field can also be missed with longer time steps. Another impact could be that the magnetic field may appear more stable than it is in reality, as transient peaks or dips are averaged out, leading to a loss of accuracy in predicting parameters like torque ripple, instantaneous flux linkage, and current distribution.

Flux Linkage and Induced Voltage

In Figure 5.5a and 5.5b, the flux linkage and induced voltage are shown, calculated from the 3D and 2D models at no load and rated load, when the

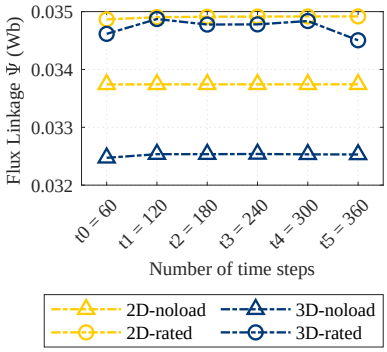

(a) Magnitude of flux linkage

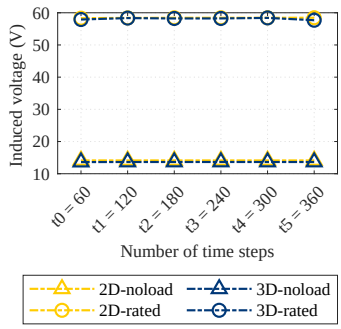

(b) Magnitude of induced voltage

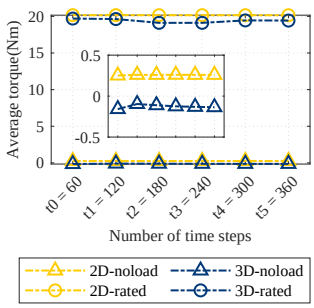

(c) Average Torque

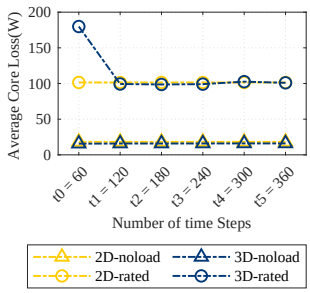

(d) Average core loss

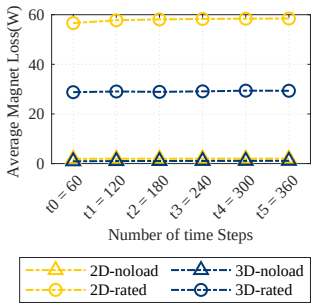

(e) Average magnet loss

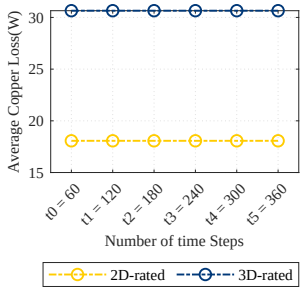

(f) Average copper loss

Figure 5.5: Comparison of the magnitude of flux linkages, average torque, average core loss, and average magnet loss between the 3D and the 2D models for varying time steps and with medium mesh element size per electric period.

number of time steps is varied. It can be seen that in rated conditions the shorter time steps help in capturing the rapid fluctuations in flux and hence in induced voltage. At no load, the variations in time steps from longer to shorter does not show any differences in accuracy for both 3D and 2D models. However, in rated conditions, the 3D model shows a slight difference of 0.9% with the time step of $t0 = 60$ and $t1 = 120$ and a difference of 1.2% in accuracy is seen when the time step is $t5 = 360$. Similar differences were seen in induced voltage accuracy as well.

Torque

In Figure 5.5c, the average torque for no load and rated condition are presented for both 3D and 2D models. At no load, the torque is sensitive to changes in time steps, similar to the mesh density variation, resulting in differences of 3.3 % in accuracy between the variation in time steps of $t0$ and $t1$. A difference of 0.2% to 0.3% is present between the time steps $t1$ to $t5$ for the 2D model. However, at no load in the 3D model, differences in accuracy are quite inconsistent and the difference in accuracy ranges between 13% - 39% with varying time steps. In rated condition, the 2D model shows barely any difference in the accuracy of the measured average torque with varying time steps. In the 3D model the differences range between 0.3% to 1% when the time steps are varied between $t0$ to $t5$. Hence, the variation of time steps with average torque can be interpreted as quite sensitive and inconsistent in the no load conditions for both 3D and 2D models, and the accuracy of the measured average torque is quite stable in the rated case. It should be considered that the choice of time step depends on the amount of transients that are needed to capture. The cogging torque is specifically difficult to model with few time steps, and this can be seen in Figure 5.20 where the cogging torque versus time is seen with $t1 = 120$ steps. In the ideal case, with a perfect time and mesh resolution, the average cogging torque should be zero.

Core Loss

The accuracy of measured average core loss with varying time steps is shown in Figure 5.5d. At no load, the change of the average core loss with varying time steps is almost zero in a 2D model. However, in the 3D model the average core loss is slightly sensitive to varying time steps with a difference in accuracy

ranging from 0.04% to 1.35%. At rated condition, a difference of 0.02% in the 2D model is seen with varying time steps. However, in the 3D model, the variation in time steps affects the average core loss, and the difference ranges from 0.65% to 3.23% and a major difference of 44% is observed when the time steps are varied between $t0$ and $t1$. Hence time step of 120 is a quite reasonable choice from the accuracy and computational time perspective.

Magnet Loss

In the mesh density variation investigation, it was seen in Figure 5.3e that the magnet losses are quite sensitive to the choice of mesh in both the 3D and 2D models (at rated operation). A similar trend can be observed in Figure 5.5e regarding the variation of time steps. At no load, the differences in accuracy of the average magnet loss in a 2D model range between 0.89% and 2.75%. However, the 3D model is more sensitive to variation in time steps compared to the 2D model ranging from a difference of 3.1% to 8.3%. At the rated condition, the differences in accuracy are not that prominent as compared to the no-load condition. In the 2D model the accuracy differs between 0.6% to 2%. However, in the 3D model the accuracy differs between 0.2% to 1.2% with variation in time steps. These differences in accuracy are measured for time step $t1 = 120$. Owing to the differences in accuracy, the time step $t1 = 120$ is considered reasonable.

Copper Loss

The copper loss in the rated condition is shown in Figure 5.5f. Due to the higher copper volume included in the 3D model the losses are high compared to the 2D model. The copper losses are not sensitive to variation in time steps in the 2D and 3D models since only DC copper loss is considered.

5.2.2 Relative Difference between the 3D and 2D Models

In this section, a sensitivity analysis is performed as shown in Figure 5.6 to analyze the differences in the accuracy of the measured parameters such as flux linkage, induced voltage, torque, and losses, for both no load and rated operation in the 3D and 2D models with varying time steps.

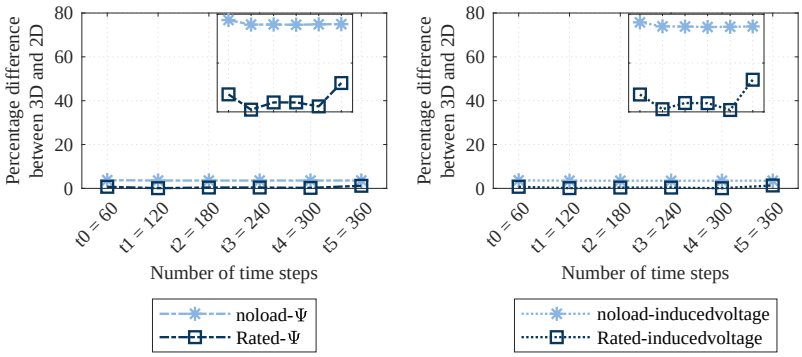

(a) Magnitude of flux linkage

(b) Magnitude of induced voltage

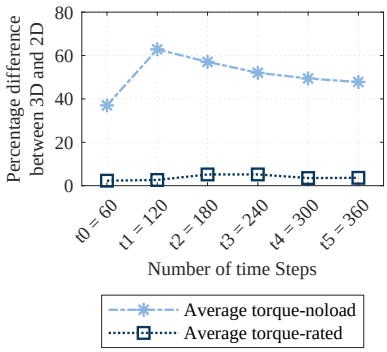

(c) Average torque

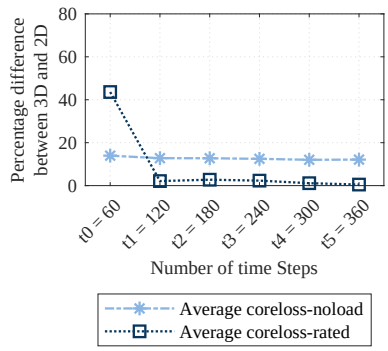

(d) Average core loss

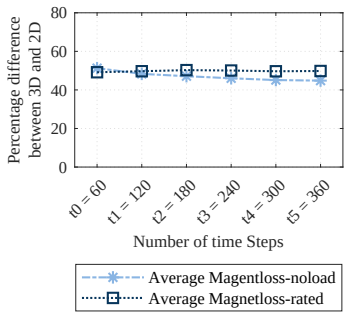

(e) Average magnet loss

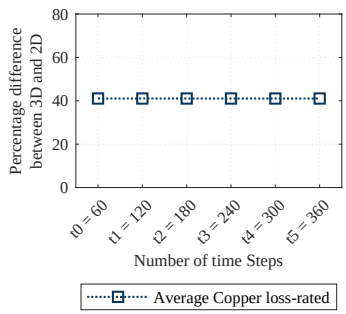

(f) Average copper loss

Figure 5.6: Sensitivity analysis between 3D and 2D model with time step size variation

Flux Linkage and Induced Voltage

The percentage difference between 3D and 2D models with varying time steps for flux linkage and induced voltage are shown in Figure 5.6a and 5.6b. The differences between the 3D and 2D model are less than 4% for the no-load case and less than 2% for the rated case. In both cases, the difference is not so much depending on the choice of time-step.

Torque

In Figure 5.6c, the percentage difference between 3D and 2D models with varying time steps for calculated average torque is presented. The difference in accuracy at no load ranges between 40% to 60%, with the best match found at $t5 = 360$ steps. The major contributor to the high difference in no load is the cogging torque fluctuations. Shorter time steps make both models more sensitive to local flux variations and transient events. In 3D these phenomena are captured more accurately compared to the 2D models, as previously described. At rated conditions, the difference in accuracy is below 5%.

Core Loss

In Figure 5.6d the percentage difference between 3D and 2D models with varying time steps for average core loss are presented. As seen, the difference at rated operation is low, nearly negligible at time steps above 120. The difference is higher at no load. This is because core loss is the dominant loss at no load. Yet, the difference between the 3D and 2D models in no-load loss seems not much affected by the choice of time-step, being about 15% for all time-steps.

Magnet Loss

The percentage difference between the 3D and 2D models for varying time steps for average magnet loss are shown in Figure 5.6e. It is seen that the percentage difference between 3D and 2D is high, around 50%, although it decreases slightly with time step refinement.

Copper Loss

The average copper losses are the same as in the mesh density variation sensitivity analysis. In Figure 5.6f the DC copper losses are, not surprisingly, seen not to be sensitive to variations in time steps.

The differences between the 2D and 3D magnet and core loss calculations are further addressed in section 5.3, investigating a 3D block model, thus a 2D model extruded along the active length of the motor. This is done to investigate if the difference between the 2D model and the 3D model stems from differences in solvers and mesh elements, or is solely due to end leakage effects and geometrical differences.

5.3 Extruded 2D Model into Simplified 3D Model

The earlier sections examine the 3D and 2D models, focusing on variations in mesh element size and time step. These investigations highlight differences between the 3D and 2D models due to variations in geometry and solvers. However, creating a 3D extrusion of the 2D model could help clarify these differences more distinctly. The extruded 2D model is as shown in Figure 5.7. Similar variations in mesh element size and time steps applied to the 3D and 2D models are also implemented in the extruded 2D models.

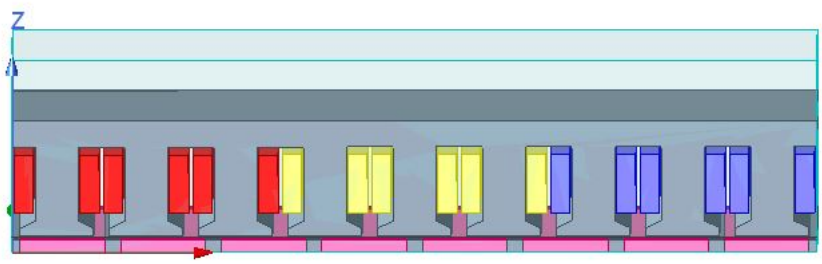

Figure 5.7: 3D extrusion of the 2D model

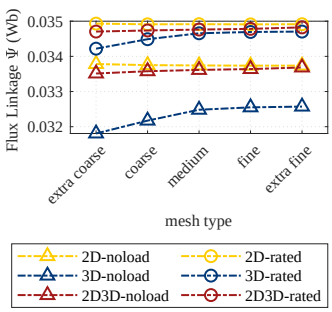

(a) Magnitude of flux linkage

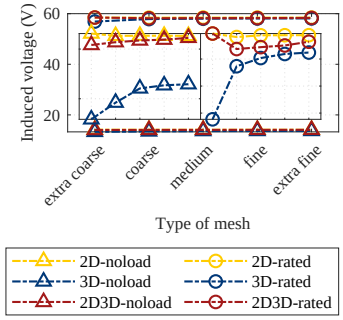

(b) Magnitude of induced voltage

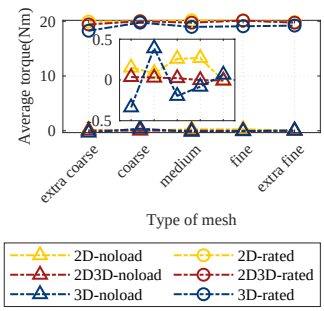

(c) Average Torque

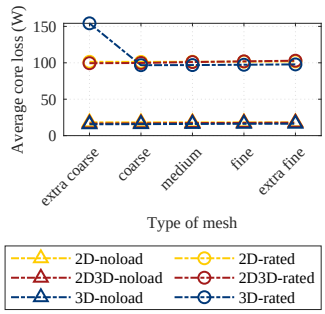

(d) Average Core loss

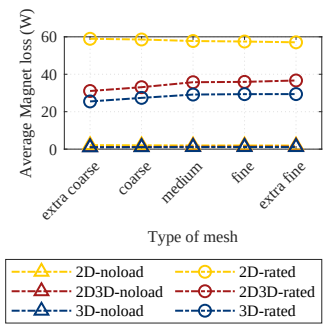

(e) Average Magnet Loss

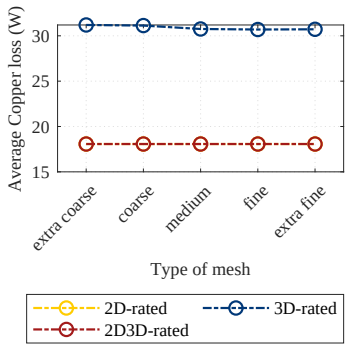

(f) Average Copper Loss

Figure 5.8: Mesh density variation in the 3D model, extruded 2D model and 2D models of the AFM

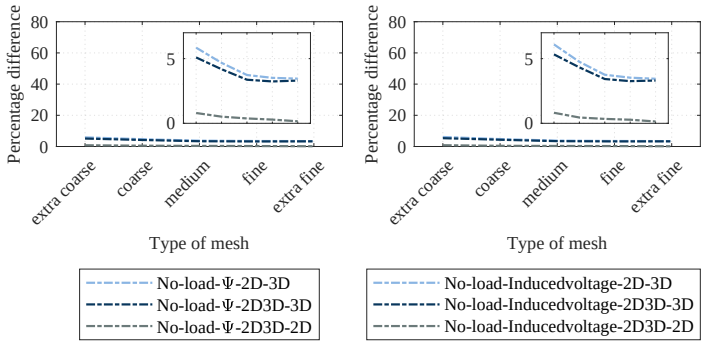

(a) Magnitude of flux linkages **(b)** Magnitude of induced voltage

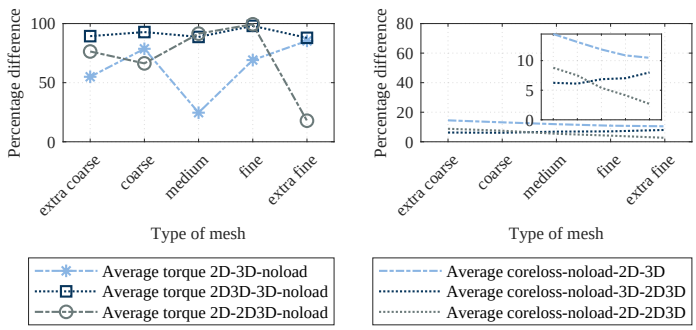

(c) Average Torque **(d)** Average Core loss

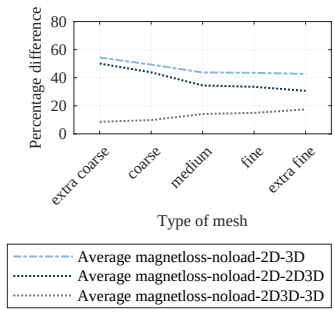

(e) Average Magnet Loss

Figure 5.9: Sensitivity analysis in No load between 3D, extruded 2D and 2D model with the mesh element size variation

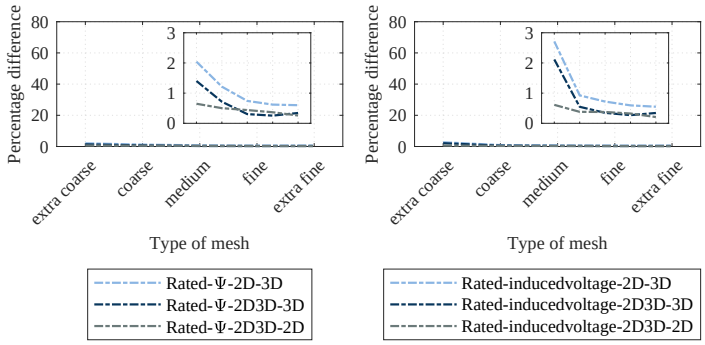

(a) Magnitude of flux linkages **(b)** Magnitude of induced voltage

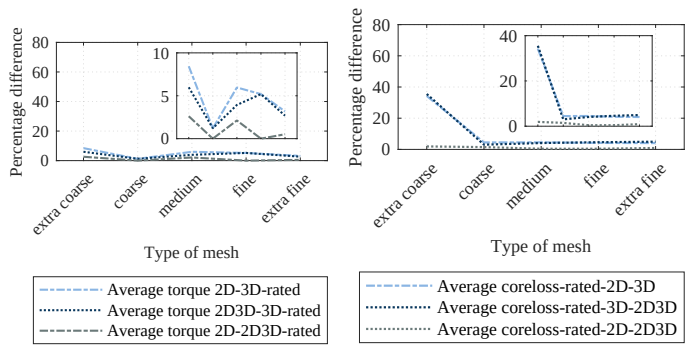

(c) Average Torque **(d)** Average Core loss

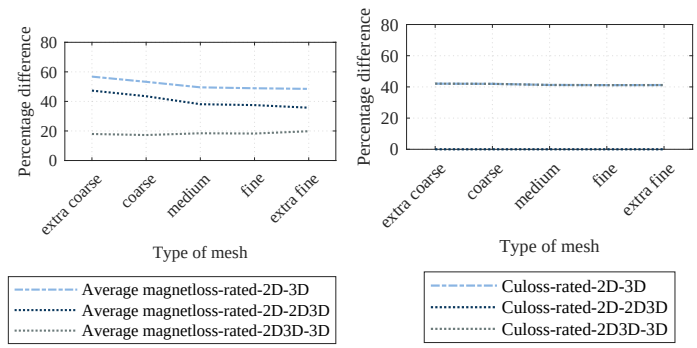

(e) Average Magnet Loss **(f)** Average Copper Loss

Figure 5.10: Sensitivity analysis in rated condition between 3D, extruded 2D and 2D model with the mesh element size variation

5.3.1 Mesh Element Size Variation

Flux Linkage and Induced Voltage

In Figure 5.8a and 5.8b, the flux linkage and induced voltage from the 3D, extruded 2D and 2D models are plotted versus the mesh type. The differences arising in the flux linkages and induced voltages in 3D and 2D models are discussed in the previous section. In Figure 5.8a and 5.8b, the magnitude of flux linkages and induced voltage in extruded 2D model and 2D model are quite close in no load condition as compared to the 3D model. In Figure 5.9a and 5.9b, it can be observed that the percentage difference between the extruded 2D and 2D models is less than 1%, while the difference compared to the 3D model is less than 6%. The 1% variation is anticipated due to differences in mesh element and solver types. In the rated condition, the percentage differences between the extruded 2D model and 2D model are shown in Figure 5.10a and 5.10b, and it can be noted that the percentage differences are low as compared to the 3D model.

Torque

In Figure 5.8c, the average torque at no load and rated condition for the extruded 2D and 2D models are compared. The cogging torque is quite sensitive to edge effects and the average cogging torque should be zero. In the extruded 2D model, the cogging torque is not significantly influenced by variation in mesh density and the cogging torque is approximated based on the uniformity along the extrusion axis. End effects and axial variations are neglected, potentially underestimating or oversimplifying the cogging torque hence the percentage differences are a bit unpredictable with varying mesh density due to cogging torque ripple as shown in Figure 5.9c. In the rated condition, the percentage differences between the extruded 2D and 2D models are below 3% as illustrated in Figure 5.10c.

Core Loss

The extruded 2D model and the 2D models depict similar results with varying mesh density in Figure 5.8d. The percentage differences between extruded 2D and 2D models both at no load and at rated condition are lower than 1% as shown in Figure 5.9c and 5.10c. This implies that the uniform flux distribution

along the extrusion axis in the extruded 2D model fails to capture end-region effects, such as non-uniform flux or leakage flux variations.

Magnet Loss

The average magnet losses between 3D, extruded 2D and 2D models are shown in Figure 5.8e. Unlike core losses, the extruded 2D and 3D models have lower loss values compared to the 2D model in both no load and rated condition. The losses follow similar trends in extruded 2D and 3D models. In Figures 5.9e and 5.10e the percentage differences between the extruded 2D and 3D models are less than 20% for the medium mesh type and close to 20% for the extra fine mesh type. The percentage difference between 2D and extruded 2D models is between 35% and 50% with varying mesh density. The percentage difference between 3D and 2D models is between 50% to 60%.

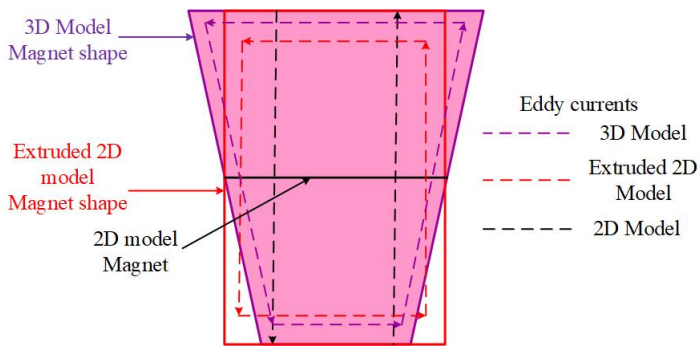

Figure 5.11: Eddy currents in magnets for different models

Figure 5.11, provides a detailed explanation of magnet losses, highlighting the differences among the three models. In the 3D model, the PMs have a trapezoidal shape, while in the extruded 2D model, it is rectangular (having the same cross-section area). The magnet in the 2D model, is represented as a line in Figure 5.11. The trapezoidal magnets in the 3D model create more complex flux gradients due to the non-uniform geometry, leading to dissimilar eddy current path lengths as illustrated in Figure 5.11. The losses in the 2D model are higher than the 3D model. The losses in the extruded 2D model is close to the 3D model since the induced eddy currents can circulate within the magnet in both models. However, in the 2D model, the assumed simple

path of the eddy currents, which do not represent the actual distribution in the trapezoidal magnets nor account for 3D leakage flux and hence further oversimplifies the behavior.

Copper Losses

The copper losses in the extruded 2D model and 2D model are shown in Figure 5.8f and the respective percentage differences between 3D, extruded 2D and 2D models are shown in Figure 5.10f. The end turns are not included in the extruded 2D model hence there is a difference in average copper loss between the 3D and extruded 2D model. However, the copper loss is the same in the 2D and extruded 2D model.

5.3.2 Time Steps Variation

In this section, a sensitivity analysis is performed as shown in Figures 5.12, 5.13 and 5.14 to analyze the differences in the accuracy of the measured parameters between 3D, extruded 2D and 2D models with varying time steps. It could be seen that the 2D and extruded 2D models are more or less independent on the choice of time steps, whereas the 3D model is more sensitive to a variation in time-step for the chosen medium mesh density.

5.4 Impact of End Leakage Flux

In this section, the $4kW$ AFM is compared with its equivalent 3D and 2D FEM model. The measured no-load induced voltage of the reference AFPM machine at 500 rpm is compared with its equivalent calculated results from the 3D FEM model. Furthermore, the 3D model is compared with the transformed 2D model for varying core lengths and magnet lengths as shown in Figure 5.15. Note that the outer diameter is kept constant. The resulting flux linkage, torque, and loss are plotted in Figure 5.16.

The model geometry of magnets and coils differs slightly between the 3D and 2D models. The reference AFPM machine and the 3D FEM model have trapezoidal-shaped magnets and the 2D model has rectangular-shaped magnets. Furthermore, the end parts of the coils are not included in the 2D model.

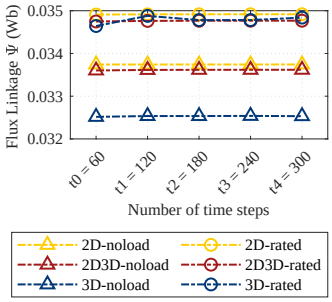

(a) Magnitude of flux linkage

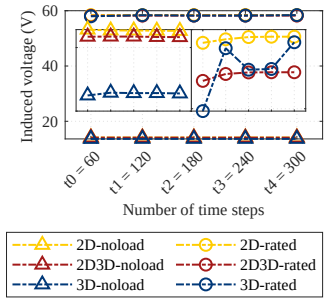

(b) Magnitude of induced voltage

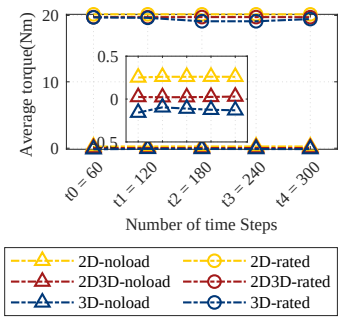

(c) Average Torque

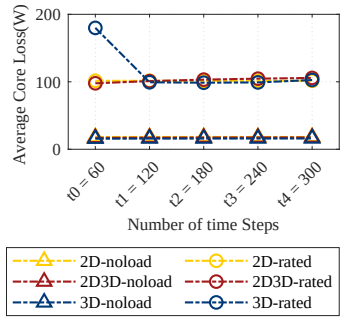

(d) Average Core loss

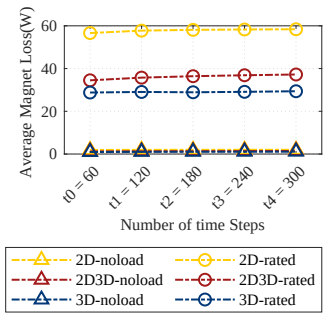

(e) Average Magnet Loss

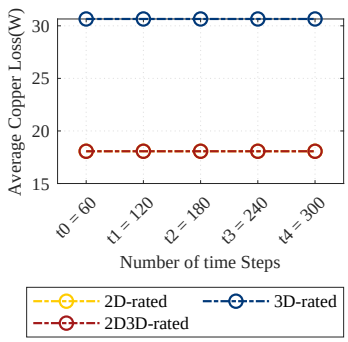

(f) Average Copper Loss

Figure 5.12: Time step variation in the 3D model, extruded 2D model and 2D models of the AFM

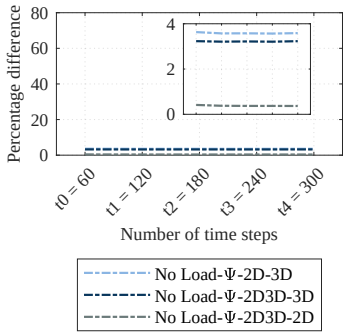

(a) Magnitude of flux linkages

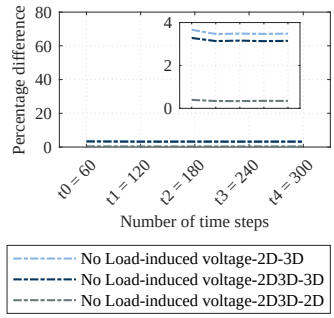

(b) Magnitude of induced voltage

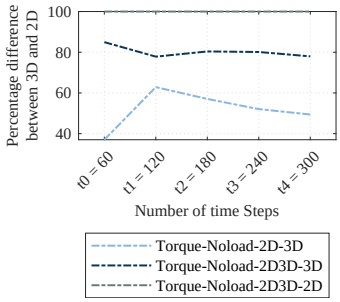

(c) Average Torque

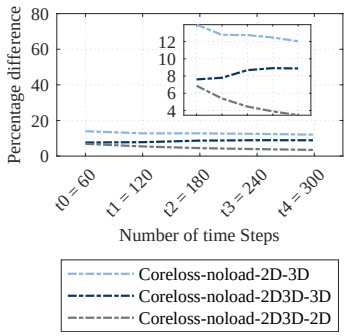

(d) Average Core loss

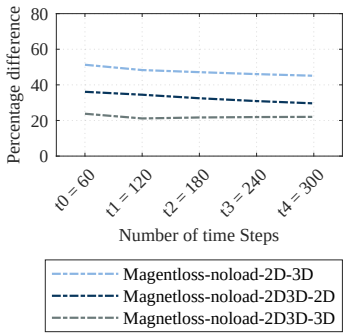

(e) Average Magnet Loss

Figure 5.13: Sensitivity analysis in No load between 3D, extruded 2D and 2D model with the time step variation

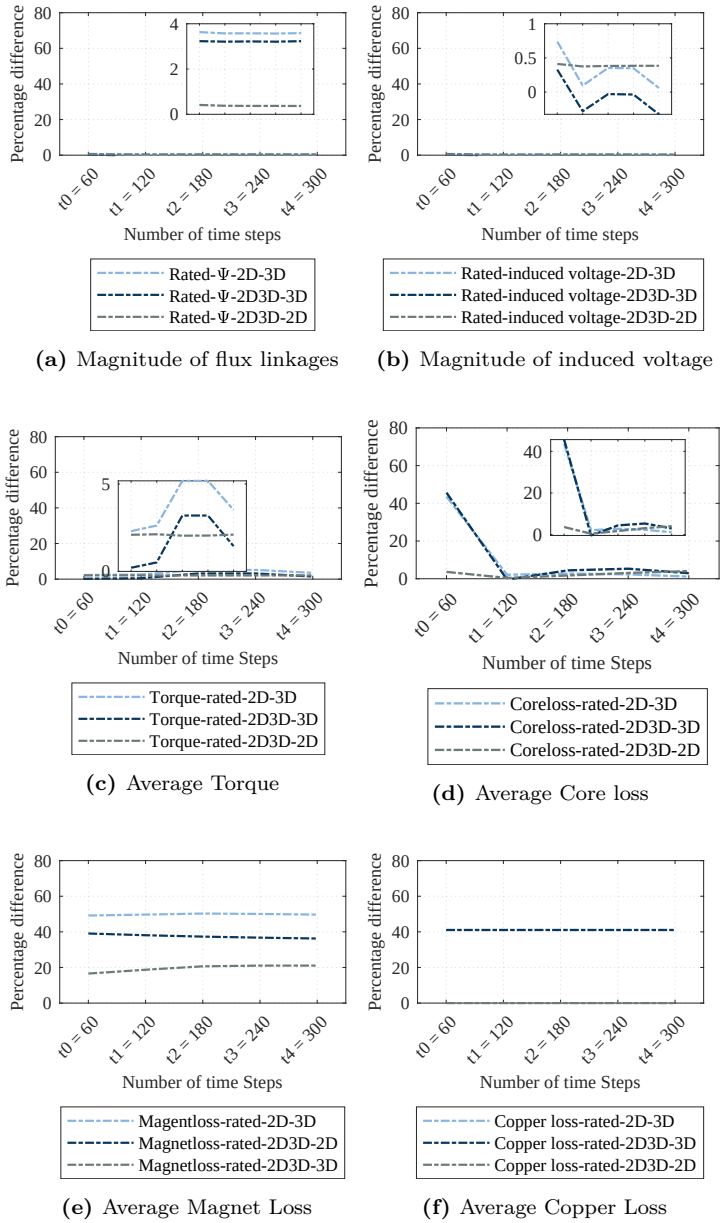

(a) Magnitude of flux linkages **(b)** Magnitude of induced voltage

(c) Average Torque **(d)** Average Core loss

(e) Average Magnet Loss **(f)** Average Copper Loss

Figure 5.14: Sensitivity analysis in rated condition between 3D, extruded 2D and 2D model with the time step variation

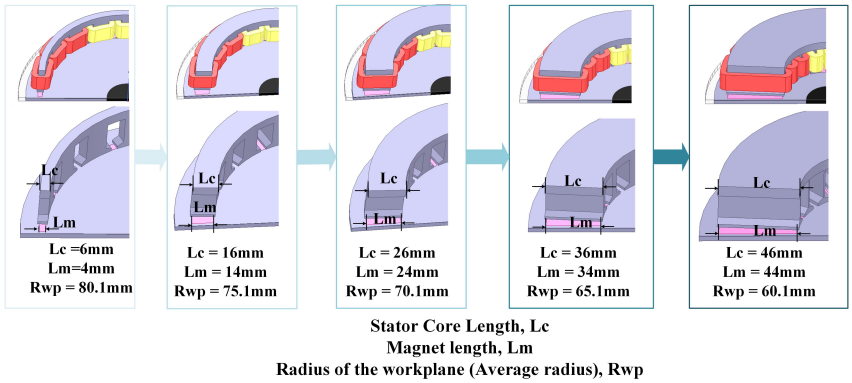

Figure 5.15: Varying core length and magnets length of the AFM

The comparison includes the magnetic flux linkage and its relative percentage difference along with the average torque, average core loss, and magnet loss for both no load and rated conditions.

In Fig. 5.16a showing flux linkages, a diamond-shaped marker indicates a percentage difference of less than 5% between the 3D model and the 2D model for a magnet length of 34mm. Conversely, a star-shaped marker signifies a higher percentage difference of 39% between the 3D and 2D models for a magnet length of 4mm.

The average torque and average core loss comparison are depicted in Figures 5.16b and 5.16c. It is observed that the discrepancies between the 3D and 2D models for torque and core loss values at rated motor operation are small across various magnet and core lengths.

The complex three-dimensional nature of eddy current formation results in larger differences in average magnet losses between the 3D and 2D models under rated operation, as illustrated in Figure 5.16d.

5.4.1 The Differences between 3D and the 2D FEM Model

The model with the narrow core with a magnet length of 4 mm (as seen to the left in Figure 5.15 is selected to investigate further the limitations of reducing

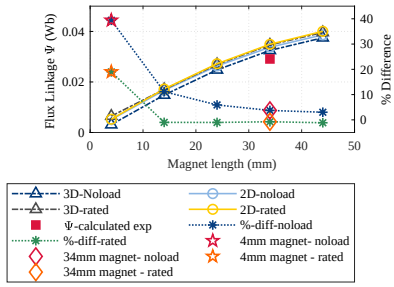

(a) Magnitude of flux linkages and percentage difference in the magnitude of flux linkage between the 3D and the 2D models

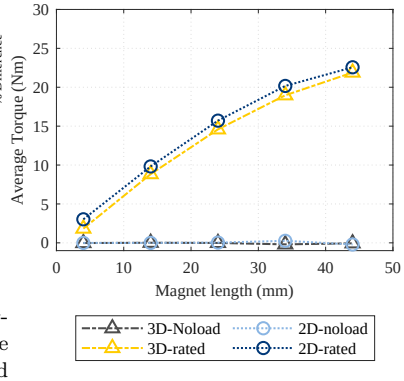

(b) Average torque

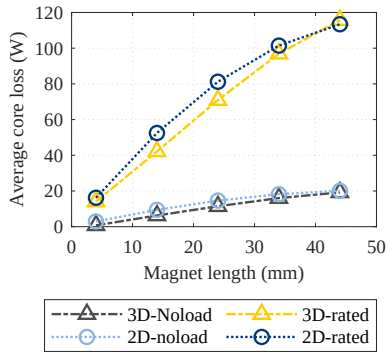

(c) Average Coreloss

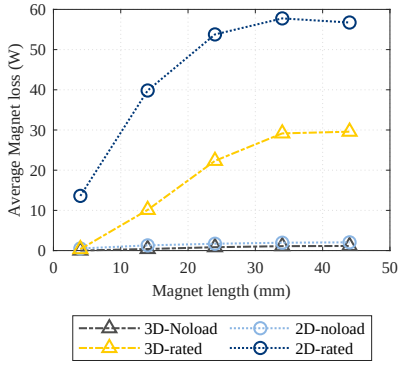

(d) Average Magnet loss

Figure 5.16: Comparison of magnitude of flux linkages, average torque, average core loss and average magnet loss between 3D and the 2D models for varying core length and magnet length but plotted concerning magnet length for no-load and rated speed of 2000 rpm of the 4 kW machine (with a 34 mm magnet length).

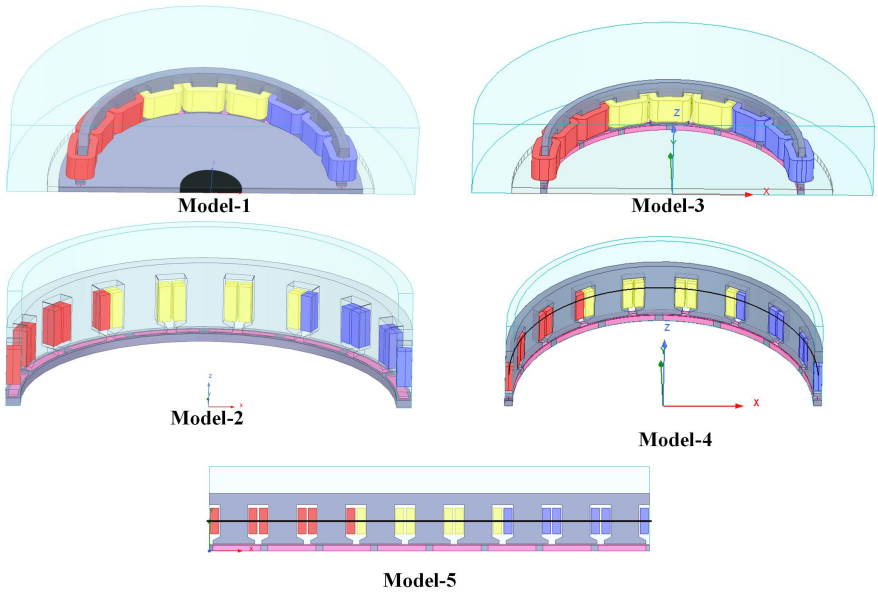

Figure 5.17: Selected machine models to investigate the difference between the 3D and 2D model. (a) Model 1 - 3D model with end winding, magnet length = $4mm$, core length = $6mm$; (b) Model 2 - 3D model without end winding, magnet length = $4mm$, stator and rotor core length = $6mm$, (c) Model 3 - 3D model with end winding, magnet, stator and rotor core length = $4mm$; (d) Model 4 - 3D model without end winding, magnet, stator core and rotor core length = $4mm$; (e) Model 5 - 2D model with depth = $4mm$

the model from a full 3D model. The model geometry was altered in five ways, and leakage due to various parts was investigated. The modifications in model geometry are listed in Table 5.3 and illustrated in Figure 5.17.

No-Load Test Analysis

At no-load when the machine is operated at a rated speed of 2000 rpm, the magnitude of flux linkages are studied for the five different models, see Figure 5.18. The flux linkage magnitude provides information about the leakage flux. It can be observed that models 1 and 2 have the lowest flux linkage with more leakage flux than the other models. The winding end part is wider than

Table 5.3: Description and differences in selected models

Model	Stator and Rotor Core length [mm]	Magnet length [mm]	Geometry modification in radial direction
Model 1[d]	6[c]	4	End winding and rotor core present
Model 2	6	4	End winding removed and rotor core present
Model 3	4	4	End winding present and rotor core removed
Model 4	4	4	End winding and rotor core absent
Model 5[e]	4	4	End winding and rotor core absent

[c]Applies only for stator core

[d]Full 3D model

[e]2D model

the active part for the narrow core geometry. The wider end winding part (in model 1) and the rotor core around the magnets (in models 1 and 2) account for a relatively higher-end winding and magnet leakage flux.

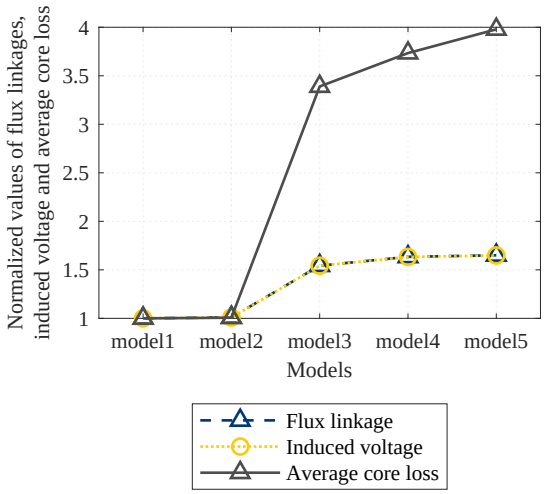

Figure 5.18: Normalized values of the magnitude of flux linkage and induced voltage, average core loss at no-load for the five models

The normalized values of core loss follow the flux linkage values since the core loss depends on the square of the flux density. The flux density predicted by different models varies in the tooth as illustrated in Figure 5.19a. Figure 5.19b illustrates the flux leakage from coils and magnets. The illustration makes it apparent that the increased leakage flux in models 1 and 2 is attributable to the lower flux density in the teeth of models 1 and 2. The similar results of model 1 (with end windings) and model 2 (without end windings) clarify that the primary source of leakage flux is attributed to magnet flux leaking to the rotor core, with a lesser contribution from the end part of the winding. Likewise, the flux in models 1 and 2, with the rotor core positioned both outside and inside of the magnets, and without outside and inside rotor cores in models 3, 4, and 5, exhibits a more noticeable and substantial difference.
Cogging torque as shown in Figure 5.20, core loss, and magnet loss are sensitive to selected mesh element size and number of time steps. A fine mesh is chosen

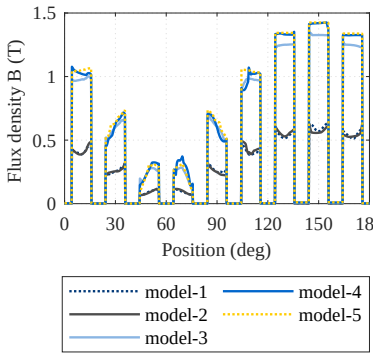

(a) Tooth flux density versus position (circumferentially) for half of the machine with 8 magnets and 9 slots depicting 180deg

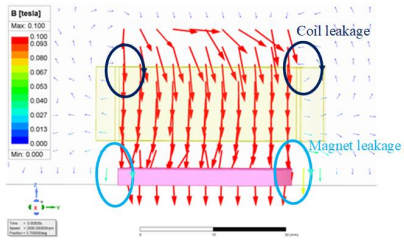

(b) Flux density vectors in coils and magnets in the 3D FEM model

Figure 5.19: Flux density in parts of the machine

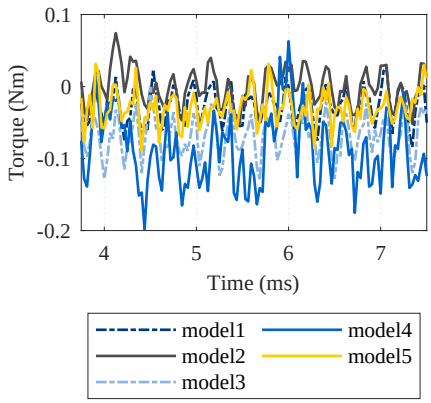

Figure 5.20: Cogging torque versus time with the torque plot being centralized near zero to demonstrate the torque ripples for the five models.

in the models, utilizing tetrahedral elements for the 3D model and triangular elements for the 2D model, with 120 time steps per period. However, cogging torque is especially sensitive, and before presenting results of torque ripple, even better discretization (in 3D) is required. Still, initial results of cogging torque in the five models show that the highest torque ripple is found in model 4. The boundary of model 4 lies along the core, and all magnet flux is recorded passing along the sharp corners of the teeth, hence larger torque ripples are to be expected.

Load Test Analysis

The load test analysis assesses the load torque and losses. The results in this section are recorded when the machine was operated at 2000 rpm, with a maximum excitation current of 60A.

The average torque concerning the load current is illustrated in Fig. 5.21. The average torque tends to saturate in models 1 and 3. Since models 1 and 3 encompass the end region with an end winding, the leakage flux around the end winding plays a role in the saturation of the stator core, with more flux leakage at higher currents. Models 2, 4, and 5 have boundary conditions that prevent the inclusion of this effect. Thus in subsequent models, all the currents are utilized effectively, and the flux remains contained within the active part of the machine.

The core loss is illustrated in Fig. 5.22. In models 1 and 2 the leakage flux in the rotor core around the magnets and in the end part of the winding leads to a lower magnetic flux density in the tooth, similar to the no-load test. Consequently, the core loss is lower than in the other models at lower load currents. At high currents, the end winding leakage in model 1 induces increased core loss compared to model 2. A similar effect is observed in model 3, indicating a core loss increase with increased currents. In models 2, 4, and 5 the core loss practically remains constant with increasing load current. Models 4 and 5 exhibit a minor difference in the average core loss, possibly attributable to the tapered magnets and the difference in mesh elements.

From the magnet loss plot illustrated in Figure 5.23, it is seen that an increase in current leads to increased magnet loss in all models with the highest loss in

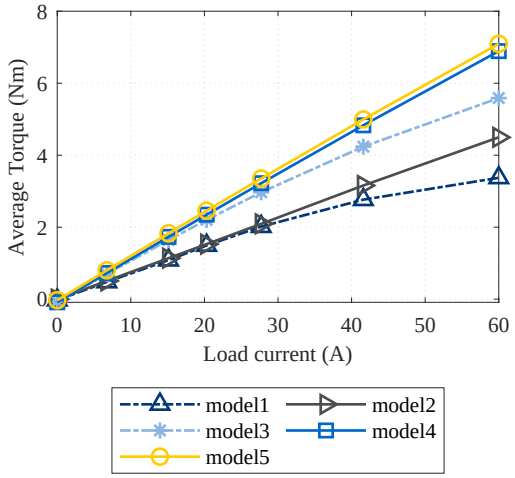

Figure 5.21: Average torque of the five models; models 2, 4, and 5 depict a linearly increasing curve without the end parts of the winding; models 1 and 3 with the end part of the winding depict a slightly bent curve starting at 27A.

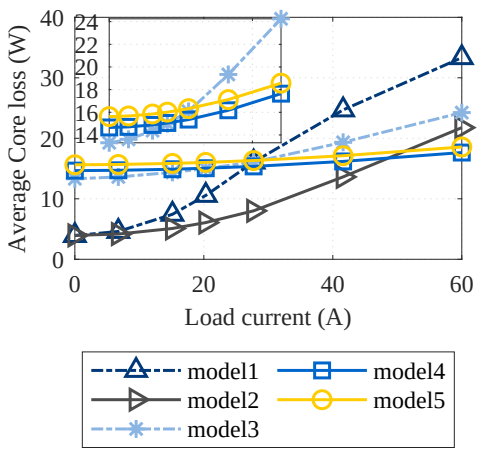

Figure 5.22: Average core losses versus load current; the curves for models 3, 4, and 5 are zoomed in as they appear flat when plotted along models 1 and 2.

models 4 and 5. The boundary condition in both models 4 and 5 forbids any leakage and hence the stator flux is channelized into the magnets. The steady increase in flux with an increase in load current induces circulating current within the magnets and hence the magnet losses are found to be greater in model 5. Nevertheless, it is the same with model 4 but the shape of the magnets is trapezoidal as compared to the rectangular magnets in the 2D model (model 5). The lower magnet loss in model 4 compared to model 5 as previously explained is due to the shape of the magnets with their assumed eddy current paths (as shown in Figure 5.11), and the different mesh elements. In contrast to models 4 and 5, models 1, 2, and 3 include the effects of leakage flux, resulting in lower magnet loss.

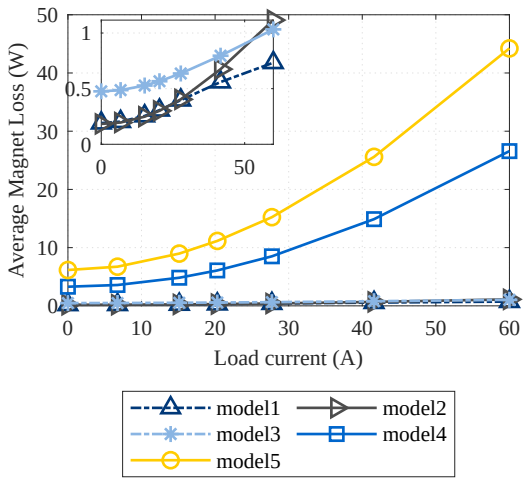

Figure 5.23: Average magnet loss versus load current; Models 1, 2, and 3 are nearly flat and equal to zero in the main plot hence, the zoomed-in plots of these three models depict that the losses are low and increasing

The cross-section area of the copper is equivalent in all five models. However, in the 3D models, the volume of the copper in the winding is not the same when compared to the 2D model. The copper loss is illustrated in Fig.5.24. Model 1 and Model 3 have slight differences, although they both contain end windings. The stator core length is 6mm in model 1 (similar to model 2) and 4mm in model 3. As a consequence, there is a difference of 2mm in the active length of the coil. The copper loss in models 4 and 5 are the same as

the models are geometrically equivalent regarding coil volume. The analysis of copper losses only includes DC copper loss, and the examination of AC copper losses is beyond the scope of this report.

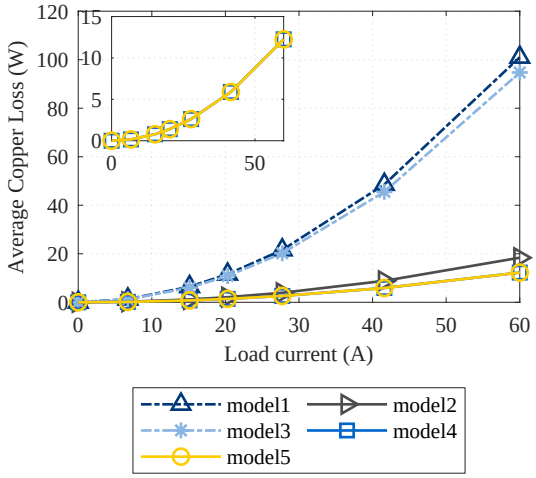

Figure 5.24: Copper loss versus load current; models 4 and 5 have the same cross-section area and the depth of stator core; Models 1 and 3 have end part of the winding and the stator core length has a difference of 2mm; Model 2 is without the end part of the winding but with stator core length of 6mm.

5.5 Torque-Speed Plots of the 3D and 2D Model

In this section, the torque- and power-limits versus speed for the 3D and 2D models are compared. The rated current of $25A$ is used as the current limit, and the voltage limit is predicted to be 60 V, which is close to the induced voltage at rated speed ($2000rpm$). The resulting torque and power for a few speeds are shown in Figure 5.25. It can be seen that the 3D model has lower torque and power values compared to the 2D model. The leakage flux reduces the effective magnetic flux interacting with the rotor, which lowers the torque, and the leakage flux is captured in the 3D model resulting in a lower torque value than the 2D model. In the previous section, it is explained that the 2D model neglects the edge effects and leakage paths occurring at the edge of the machine. At high speeds the eddy current becomes dominant and the eddy

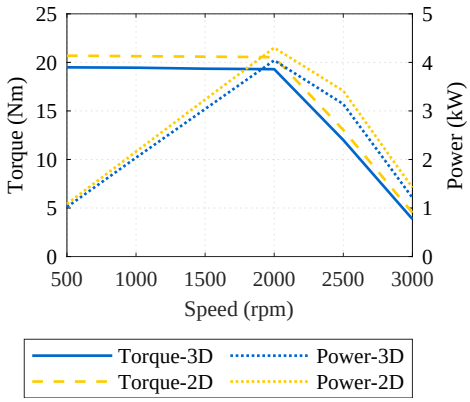

Figure 5.25: Comparison of torque speed curve between 3D and 2D model

currents are incorporated in 3D models. These effects are not captured in the 2D model effectively as compared to the 3D model. The power at higher speeds is a bit uncertain due to the prediction of the voltage limit.

CHAPTER 6

End-Turn Leakage Inductance Investigation

This chapter investigates the end-turn leakage inductance in AFMs using both 3D and 2D modeling approaches. By comparing the results from 2D and 3D models, the study aims to highlight the differences in accuracy and the impact of geometric complexities. The chapter explores the limitations of 2D models and emphasizes the importance of 3D simulations for capturing realistic inductive effects in the end-turn.

6.1 Stator Winding Leakage Inductance in 3D and 2D Models

The AFM phase winding inductance comprises the main inductance L_s (representing the main flux that passes the air gap), and the leakage inductance L_λ (representing the stator leakage flux). The stator leakage flux, in turn, consists of slot leakage inductance $L_{\lambda,slot}$ and end turn inductance leakage inductance $L_{\lambda,end}$. Thus the total per-phase inductance L_{tot} is,

$$L_{tot} = L_s + L_\lambda = L_s + L_{\lambda,slot} + L_{\lambda,end}\ (H) \tag{6.1}$$

The main flux experiences a large air gap along the d-axis (comprising of the air gap and the magnet length), and a short air gap along the q-axis (comprising only of the airgap). The end-turn leakage flux ϕ may follow three different paths around the end-turns: a) only through the air in the end parts of the machine, b) partly through the air in the end parts and partly through the stator core, and c) partly through the end parts and partly through the rotor core. For a machine with CWs, the first path, (point a above) is relatively short since the coils are closely wound around the tooth. It is only for the third path (point c above) that the rotor position plays an importance. Thus, the end leakage flux will not be the same along the d- and q-axis, and the corresponding end-turn inductances $L_{d\lambda,end}$ and $L_{q\lambda,end}$, will vary with imposed d- and q-axis currents differently since the saturation effects are different for the different rotor positions. Generally, for a magnetic circuit with a coil with N turns and current i, a magnetically conducting core with relative permeability μ_r, and an air gap with a distance g, the inductance is calculated as,

$$L = N\phi/i = \mu_0 \cdot A \cdot N^2/((l_c/\mu_r) + g)\ (H) \tag{6.2}$$

where l_c is the length that the flux goes in the core material, μ_0 is the permeability of free space, and A is the cross-section area through which flux passes. For high core permeabilities, the term l_c/μ_r may be ignored if the material is unsaturated. However, if saturated, the lamination stack needs to be included in the calculations, even when calculating the end-turn leakage inductance.

To find the operating points in the speed-torque diagram of the AFPM machine, the standard procedure is to run 2D FEM simulations for all possible currents, i, split in direct and quadrature axes (i_d, i_q), and extract inductances, L_d, and L_q, and magnetic flux induced from the permanent magnets, ψ_m. However, by not considering the end leakage flux (a 3D effect), the believed operating points no longer give the expected torque and power, thus tuning must be made.

In this work, the d- and q-axis leakage inductance of the off-the-shelf-AFM (described in chapter 3) with concentrated windings is first determined directly, using 2D and 3D FEM for different operating points and then the result is compared to two analytical methods found in literature [17] and [18].

In Figures 6.1 and 6.2 the inductances along the d- and q- axis are plotted for both 3D and 2D models with magnet-induced flux linkage presented in Figure 6.3. The d-axis inductances in the 3D and 2D models are calculated using 3D and 2D FEM with one of the phases aligned with the d-axis and then optimetrics were performed for varying current in the d-axis. The d-axis leakage inductance was calculated by subtracting the inductance obtained from the 2D model from the inductance obtained from the 3D model. The inductance and leakage inductance along the q-axis were calculated by repeating the same procedure as was done for the d-axis, however, this time one of the phases was aligned with the q-axis. The calculated leakage inductance and the corresponding percentage difference of the leakage inductance compared to the total inductance are presented in Figures 6.4 and 6.5, for d- and q-axes respectively. To find PM induced flux linkage (Ψ_m), the direct axis of the rotor is aligned with the phase A axis, same as when calculating d-axis inductance, but now the q-axis current is varied. The resulting leakage flux (the difference between induced flux in 3D and 2D) and its percentage difference from the main flux linkage (from the 3D results) is given in 6.6.

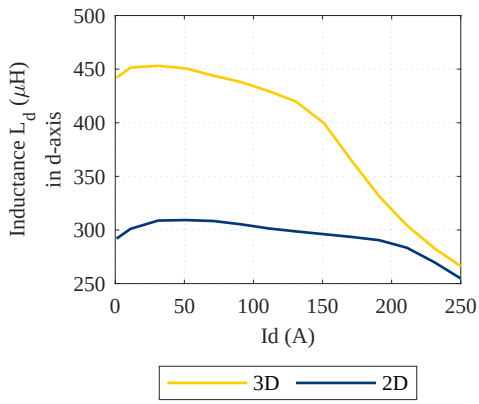

Figure 6.1: Inductance in d-axis versus d-axis current

It can be seen that in Figures 6.1 and 6.4 that the d-axis inductance is 33% larger in the 3D model compared to the 2D model at low d-axis currents, and at high currents, under saturated conditions, the difference between 3D and

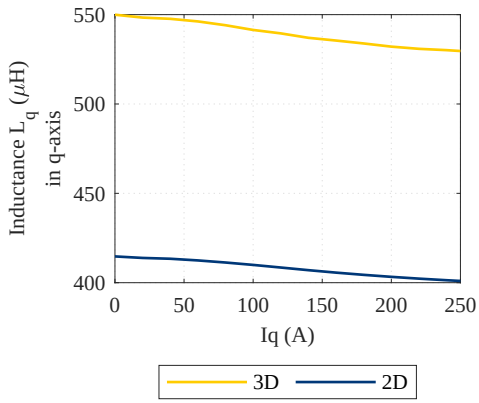

Figure 6.2: Inductance in q-axis versus q-axis current

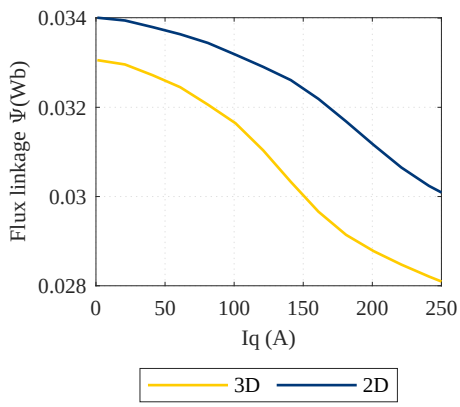

Figure 6.3: PM induced flux linkage versus q-axis current

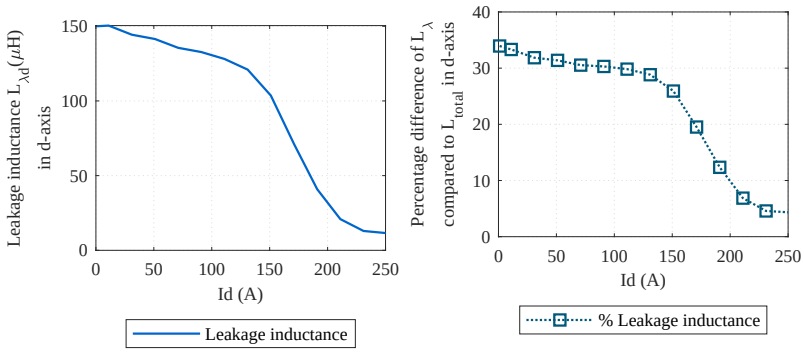

(a) Leakage inductance λ_d versus I_d

(b) Percentage difference of leakage inductance

Figure 6.4: Leakage inductance and consequent percentage difference of leakage inductance L_λ compared to total inductance L_{total} in d-axis

2D is small. The magnetic field distribution is accurately represented at low currents in the 3D model. The 3D model captures the leakages from the coil's end turn and along the sides of the magnets as shown in Figure 5.19b. The leakage and edge effects are neglected in the 2D model. This simplification leads to an underestimation of flux leakage and thus the inductance appears lower than in the 3D model. However, at higher currents the core material begins to saturate, reducing the material's permeability and thus the inductance. In the 3D model, the additional flux paths outside the core are less effective when the core saturates since the fields depend on the high permeability of the core. The inductance drops significantly. In the 2D model the leakage flux is not considered, the inductance may not decrease as drastically because the simulation doesn't capture the changes in the flux paths outside the core.

When evaluated under varying current conditions, the inductance calculated along the q-axis exhibits a slightly flatter curve compared to the d-axis inductances, as shown in Figure 6.2. The magnetic field along the d-axis interacts directly with the main flux path of the rotor and the core, the d-axis experiences stronger saturation effects because the magnetic flux is concentrated along the main magnetic flux path, especially at high currents. This results in a steep drop in inductance as the current increases. However, the q-axis repre-

sents the orthogonal path to the main flux and is less magnetically intense due to the lesser interaction involved with the magnets or rotor poles in the same way as the d-axis. Saturation effects are less pronounced because the flux density along the q-axis is lower and the magnetic paths are less constrained. This results in a flatter curve as shown in Figure 6.2, with inductance dropping more gradually as the current increases. Due to the reasons mentioned above the core saturation has a more significant impact on the d-axis inductance since the axis handles the primary flux linkage. The q-axis has a more distributed and less concentrated flux, which is less affected by saturation, leading to more stable inductance as shown in Figure 6.5, where the q-axis leakage inductance is 25% of the total q-axis inductance (calculated in the 3D model), irrespective of the current value.

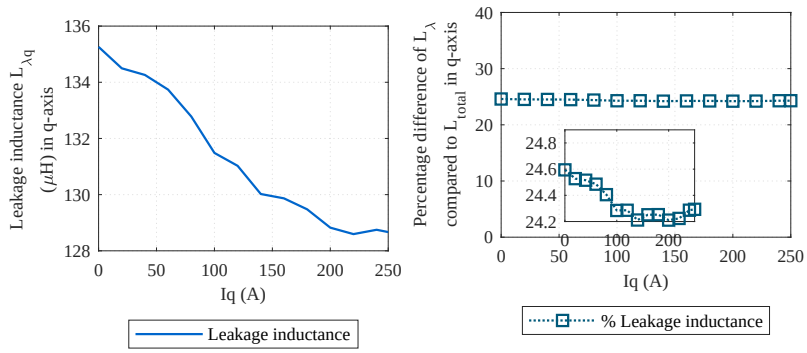

(a) Leakage inductance λ_q versus I_q

(b) Percentage difference of leakage inductance

Figure 6.5: Leakage inductance and consequent percentage difference of leakage inductance L_λ compared to total inductance L_{total} in q-axis

In Figure 6.3 and 6.6, the flux linkage of the 3D model is seen to be up to about 8% lower than the flux linkage of the 2D model. Again, this is because the 3D model captures the leakage flux from coils and magnets as in Figure 5.19b.

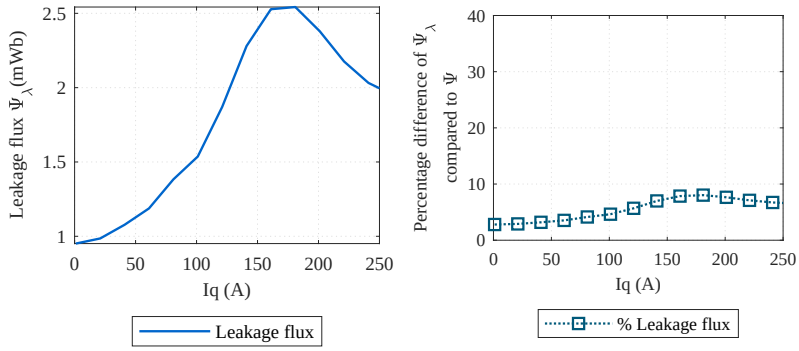

(a) Leakage flux versus q-axis current **(b)** Percentage difference of leakage flux

Figure 6.6: Leakage flux and consequent percentage difference of leakage flux Ψ_λ compared to total flux Ψ (from the 3D model)

6.2 Analytical Calculation of the End-Turn Inductance

Analytical equations and empirical formulas may be used to calculate the end-turn inductance. Two methods found in the literature, see [19] and [18], were used. In the first method [19] which is deduced for RFMs, the end part of the coil is assumed to be circular and identical on both inner and outer sides. In the second method [18], deduced for AFMs, the end parts of the coils are also assumed to be circular but with a bigger end turn on the outer side and a smaller end turn on the inner side, better replicating a trapezoidal shape more common to AFMs.

6.2.1 First Analytical Method - Circular End-Turn with Average Radius

The concentrated coil for the AFM with simplified parts of the end turns of the coil is illustrated in Figure 6.7. The dimensions of this coil are compared with the coil dimensions of the off-the-shelf AFM as in Figure 3.14.

The end coil shape is considered circular, with the two circular end sections merged to form a circular coil in the air, as depicted in Figure 6.7. Then the

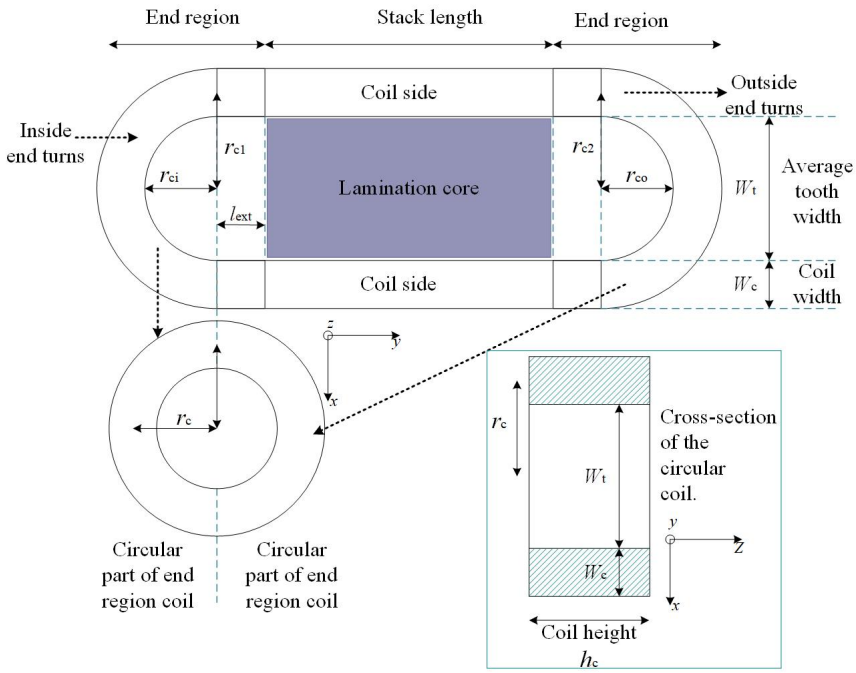

Figure 6.7: Concentrated coil with simplified circular end-winding designs

Table 6.1: Dimensions of the coil for the concentrated winding captured as shown in Figure 3.14

Parameter	Value
A	20 mm
a	18 mm
b	36 mm
c	5 mm
e	6 mm
f	4 mm
C_{dis}	3 mm

per-phase end winding inductance can according to [19], be calculated to

$$L_{\lambda end} = K_M \cdot K_P \cdot N_t \cdot N_c^2 (k_1 + k_2)/N_p^2 \tag{6.3}$$

where K_M is a mutual phase cross-coupling factor, K_P is the end region permeable support structure factor, N_t is the number of winding layers, N_c is the number of coils per phase, k_1 and k_2 are coefficients depending on slot and coil dimensions (average coil radius r_c, coil h_c and the end winding axial extension, l_{ext}) and N_p is the number of parallel branches. Equation (6.3) is calculated using a MATLAB code from [17] which is based on [19]. Table 6.1 and 6.2 show parameters and the dimensions supporting the analytical calculation in (6.3). The used value of the coil end extension is the average of the outer and inner end extensions. The actual coil in the AFM has end parts of the coil with different coil radii and the average of these coil radii r_c on the outer end turn of the coil r_{c2} and inner end turn of the coil r_{c1} are calculated.

$$r_{c_1} = \frac{c}{2} + C_{dis} \tag{6.4}$$

$$r_{c_2} = \frac{a}{2} + C_{dis} \tag{6.5}$$

$$r_c = \frac{r_{c_1} + r_{c_2}}{2} \tag{6.6}$$

$$l_{ext} = \frac{f+e}{2} \tag{6.7}$$

The end leakage inductance expressed in (6.3) is calculated using the MATLAB code attached in the appendix.

6.2.2 Second Analytical Method - Circular End-Turns with Different Inner and Outer Radius

The second analytical method is primarily developed for AFMs with concentrated windings and trapezoidal teeth. In this method, the coil's end turns are assumed to be circular, with the outer end turn being wider than the inner one. The analytical approach for calculating the end-turn leakage inductance was initially proposed in [18] for an AFM featuring a concentrated, single-layer winding. This method has been adapted for the off-the-shelf AFM with a double-layer winding. Since the exact length of the end turn and the magnetic field distribution around it are not precisely known, the length of the coil's end turn is approximated. The first method explained in section 6.2.1, is suitable for a RFM with concentrated windings. To consider the coil shapes of AFMs, the analytical method suggested in [18] should present a better choice. The coil geometry used in this method is shown in Figure 6.8. The leakage flux as in Figure 6.8 of the outside and inside end turns for the double-layer winding are calculated as,

$$\phi = \int_{r_s}^{(r_s+r_{co})} \mu_0 \frac{n_{cs} i}{2\pi x} \frac{r_{co}\pi}{2} dx \tag{6.8}$$

where r_s is the coil radius assuming a coil with a circular cross-section. It is to be noted (6.8) follows the author's interpretation of the method described in [18] (since the flux equation given in [18] seems to be inconsistent with the explained method). The total length of the end turns for a slot pair is,

$$l_{end} = (r_{co} + r_{ci}) \frac{\pi}{2} \tag{6.9}$$

It is to be noted that the analytical calculation of the end-turn leakage inductance is a rough approximation since the end-turn shape is far from circular, as is seen in Figure 3.14. Furthermore, it is only the unsaturated phase leakage inductance that is calculated, not the d- and q-axis components at varying

Parameter	Values
N_p, Number of parallel branches	1
N_{cc}, Number of conductor per coil	12
N_c, Number of coils per phase	6
S_α, Winding short pitch ratio	1
D_{is}, Inner diameter of the stator	94.2 mm
$Z = N_c \cdot S_s \cdot N_l$, Total number of conductors	432
T_{ph}, Number of turns per phase	10
p, Number of pole pairs	8
S_s, Number of stator slots	18
N_l, Number of winding layers	2
r_c, Average coil radius	8.75 mm
W_c, Width of the coil	6 mm
W_t, Average tooth width	10.71 mm
h_c, Height of the coil	15.2 mm
l_{ext}, End winding extension	5 mm
K_M, Mutual phase cross-coupling factor	1.1
K_P, end region permeable support factor	1
$l_{ew-bend}$, Span extension one side	6 mm

Table 6.2: Parameters used for calculating coil end leakage inductance

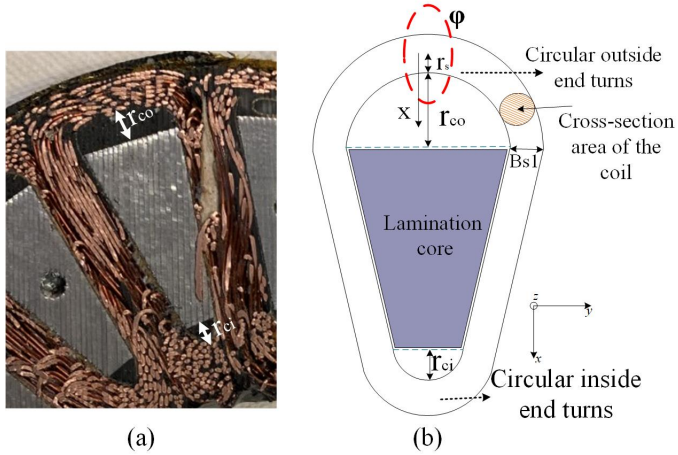

Figure 6.8: Concentrated coil with trapezoid shape and circular end-turns

current loadings (which can be calculated by FEM, as shown in 6.1). The main assumption in [18] is that the end-turn conductors form a semi-circular shape with a circular cross-section area equal to the rectangular cross-section area of the slot. This implies that the end turns are considered cylindrical cables carrying current. The rectangular coil side conductor area A_{rect} is represented as an equivalent circular area A_{circ},

$$A_{rect} = \frac{W_c \cdot H_c}{2} = r_s^2 \pi = A_{circ} \Rightarrow r_s = \sqrt{\frac{W_c \cdot H_c}{\pi}} \tag{6.10}$$

By doing this, the end leakage inductance for the outer and inner end turns are found, see [18], as

$$L_{\lambda o} = \frac{\mu_0 n_{cs}^2 r_{co}}{2} ln\left(\frac{r_s + r_{co}}{r_s}\right) \tag{6.11}$$

$$L_{\lambda i} = \frac{\mu_0 n_{cs}^2 r_{ci}}{2} ln\left(\frac{r_s + r_{ci}}{r_s}\right) \tag{6.12}$$

yielding the total end-turn leakage inductance

$$L_\lambda = L_{\lambda_o} + L_{\lambda_i} \tag{6.13}$$

The method in [18] assumes a single-layer winding. In our case, the machine incorporates double-layer windings, so the method is slightly modified (the coil cross-section area is used instead of the slot cross-section area to calculate A_{circ}.)

To analyze the importance of approximating the inner end turn radius, r_{ci} is varied while keeping the outer end turn radius $r_{co} = 9mm$ constant. The other variation was varying the outer end turn radius and keeping the inner end turn radius $r_{ci} = 2.5mm$ as constant. The results of these variations are presented in Figure 6.9. In Figure 6.9a, r_{ci} is held constant while r_{co} is varied. Increasing the outer end turn radius enlarges the leakage flux loop area, causing the flux to spread outward into surrounding non-magnetic regions. This reduces magnetic coupling and results in increased leakage inductance with increasing r_{co}, as illustrated in Figure 6.9a.

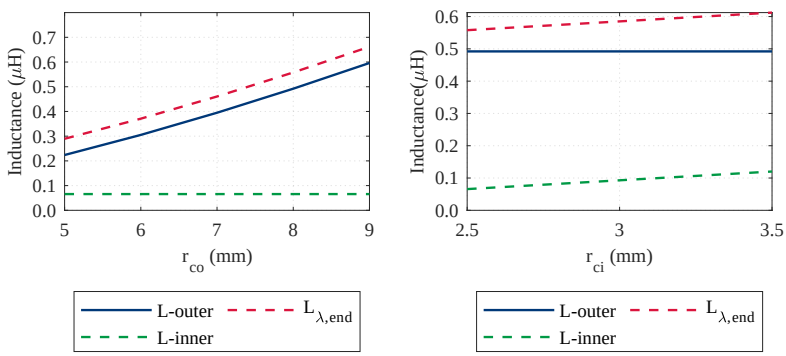

(a) Leakage inductance with varying outer end-turn radius while keeping the inner end turn radius constant (2.5mm)

(b) Leakage inductance with varying inner end-turn radius while keeping the outer end turn radius constant (9mm)

Figure 6.9: Outer and inner end-turn inductances, along with the corresponding leakage inductances, as functions of varying inner and outer coil radii of the end-turn extension, while keeping one of the radii constant.

In Figure 6.9b, the inner end turn radius is varied from $2.5mm$ to $3.5mm$ while the outer end turn radius is set to its maximum value ($9\ mm$). The high

value of r_{co} results in a larger leakage flux loop area compared to Figure 6.9a, leading to higher end-turn leakage inductance, with a maximum value of 0.66 μH. From the measurements on coil dimensions on the cut open 4 kW AFM, a span of r_{ci} between 2.5 mm to 3.5 mm, and r_{co} between 5 mm to 9 mm, is noted. This results in an estimated end-turn leakage inductance between 0.28 μH and 0.66 μH.

6.3 Comparison of the End-Turn Leakage Inductance Calculation Methods

In this section, the three methods of calculating the end turn leakage inductance are compared. The first method from [19], is the analytical calculation with a circular end turn with an average radius, the second method from [18], is the analytical method with circular end turns with different inner and outer radius, and the third method is calculating the leakage inductance in d-axis and q-axis from 2D and 3D FEM.

The leakage inductances from all three methods are compared as presented in Figure 6.10. In the first analytical method, the leakage inductance is calculated for different values of the end extension, l_{ext}, varying between $5mm$ and $8.75mm$. The average radius, r_c is kept to a constant value of $8.75mm$. In this case, the calculated end turn leakage inductance stays around 50 μH, with a slight increase when l_{ext} increase.

For the second analytical method, l_{ext} is not considered, and it was seen that the end-turn leakage inductance drastically increases with an increase in r_c.

The third method, with zero current, shows a similar trend as analytical method 1, thus a slight increase when l_{ext} is increased. The third method results were further compared with rated current and at high currents leading to saturation, and it can be seen that at high currents due to saturation the leakage inductance reduces irrespective of changing the end extension length.

Using method 3 FEM, the winding inductance and the corresponding leakage inductance for varying end extension lengths on both d-axis and q-axis are calculated and presented in Figures 6.11 and 6.12. The variation in length

extension are equally varied both on the inner and outer end turns in method 3. It is seen that the leakage inductance along both d-axis and q-axis decreases slightly with increasing the end turn extension. The q-axis end turn leakage inductance is slightly lower compared to the d-axis end turn leakage inductance for current values up to about 100 A, and thereafter the d-axis end turn inductance is lower than the q-axis end turn leakage inductance. Thus, the q-axis leakage inductance is not so sensitive to saturation, as is the d-axis leakage inductance.

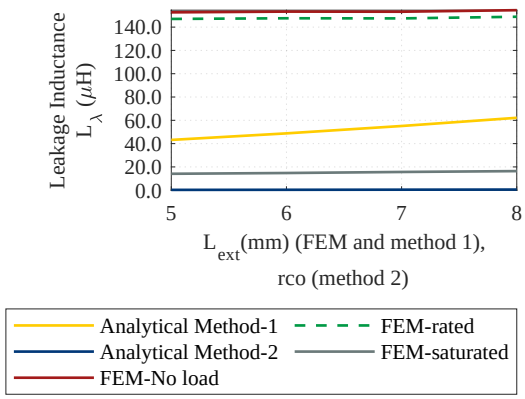

Figure 6.10: Leakage inductance with varying inner and outer end turn extension

From Figure 6.10, it is clear that neither of the analytical methods match the FEM results well. Analytical method 1 (yielding values between 44 μH to 63 μH for varying l_{ext}) underestimates the end-turn leakage inductance at rated conditions and overestimates the inductance at saturated conditions. On the other hand, analytical method 2 (yielding values between 0.28 μH and 0.66 μH for varying r_{co}) underestimates the end-turn leakage inductance at all load points.

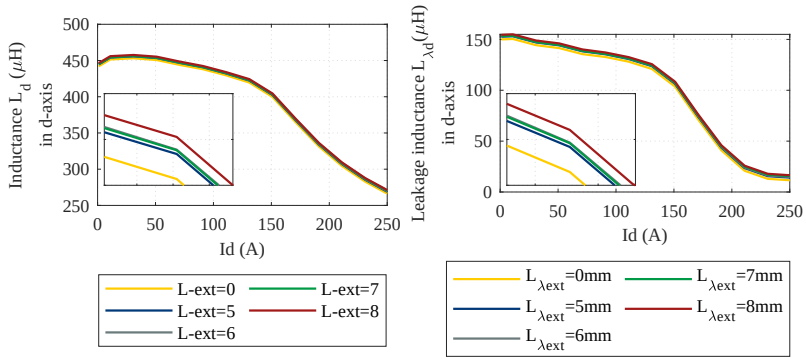

(a) Inductance in d-axis

(b) Leakage inductance in d-axis

Figure 6.11: Inductance and Leakage inductance in d-axis with varying end turn extension and Phase-A aligned along d-axis through FEM

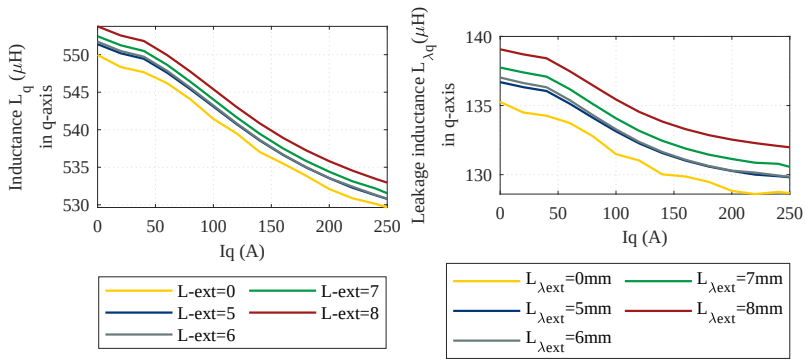

(a) Inductance in q-axis

(b) Leakage inductance in q-axis

Figure 6.12: Inductance and Leakage inductance in q-axis with varying end turn extension and Phase-A aligned along q-axis through FEM

CHAPTER 7

Conclusion and Future Work

7.1 Conclusion

This study provides a comprehensive investigation into modeling and analysis of a double stator single rotor AFM, emphasizing the differences between 3D and 2D simulation approaches. By modeling a physical AFM with a detailed 3D finite element model, validated against measurements, the work establishes a possible benchmark for accurate electromagnetic analysis of AFMs. The transformation of the 3D model into a parameterized equivalent 2D model highlights the potential and limitations of computationally efficient alternatives. Additionally, the investigation of an extruded 2D model enhances comparative insights.

The main highlight of this work is the detailed analysis of end leakage flux and end-turn leakage inductance. The comparison of the 3D and 2D models quantifies how 2D FEM methods together with analytical formulas cannot fully capture the end effects and cannot accurately calculate the end-turn leakage inductance. The two analytical methods suggested in literature for calculation of end turn leakage inductance, one for RFMs, and one for AFMs

both fail to capture the end-turn inductance well, with the best guess yielding a 60% lower value compared to FEM simulations. These effects are essential for precise performance predictions. It is found with FEM that the end-turn leakage inductances in the d- and q-directions are 33% and 25% of the total d- and q-axis inductance, respectively. The 11% difference of power between 3D and 2D at higher speeds is due to the leakage inductance.

However, for certain applications where detailed edge effects are less critical, the 2D model can serve as an effective approximation, offering a good balance between computational efficiency and accuracy. It can be concluded that the 3D AFMs with a wider core in the xy-plane can be transformed to an equivalent 2D model but the AFM with the narrow core is not feasible for transformation. For the investigated machine, the recommended ratio of the length of the magnet in the radial direction to the radius of the computational plane should be greater than 0.5.

The results indicate that the 3D models are quite sensitive to variation in mesh density and time steps compared to the 2D FEM model. The cogging torque and magnet losses are more sensitive to mesh density variation than the variation in time steps. Finer meshes and smaller time steps improve the fidelity but at the cost of increased computational resources underscoring the need for balanced modeling approaches. From the study, it is concluded that a medium-mesh density combined with 120 time-steps per electric period provides an optimal balance between computational accuracy and time efficiency.

Overall this work advances the modeling methodology of AFMs, providing valuable insights for efficient motor design. It underscores the importance of accounting for end effects and geometric intricacies.

7.2 Future Work

The work presented in this report is meant to form a good base for future investigations of the AFM and its suitability compared to the RFM, and how current solutions can be improved in terms of manufacturing, torque, and power density, and regarding recycling/reuse aspects.

Further, more specific suggestions for future work are;

- Build a parameterized YASA machine configuration with surface-mounted permanent magnets, initially with similar outer and inner diameters to the reference machine.
- Investigating different materials and designs, including scaling and possibly thermal modeling and cooling solutions.
- Continue the search for analytical/empirical methods that can be used together with 2D FEM to calculate end-turn leakage inductances.

APPENDIX A

Variables for 3D modeling

Name	**Value**	**unit**	**Evaluated**
OD_stator	166.2	mm	166.2 mm
new_depthS	36	mm	36 mm
ID_stator	OD_stator-(new_depthS*2)		94.2 mm
N_slots	18		18
Hs0	2	mm	2 mm
Hs01	0	mm	0 mm
Hs1	2	mm	2 mm
Hs2	19	mm	19 mm
Bs0	4	mm	4 mm
Bs1	12	mm	12 mm

Name	Value	unit	Evaluated
Bs2	12	mm	12 mm
Rs	0.2	mm	0.2 mm
OD_rotor	186.2	mm	186.2 mm
ID_rotor	38	mm	38 mm
Th_rotor	7	mm	7 mm
N_poles	16		16
mesh_layer	6.8	mm	6.8 mm
Th_rotor1	Th_rotor-mesh_layer		0.2 mm
OD_magnet	164.2	mm	164.2 mm
new_depthM	34	mm	34 mm
ID_magnet	OD_magnet-(new_depthM*2)		96.2 mm
Th_magnet	7	mm	7 mm
mag_gap	4	mm	4 mm
Box_x	2	mm	2 mm
Box_y	85	mm	85 mm
Box_z	-3.5	mm	-3.5 mm
Box_len	new_depthM+20mm		54 mm
pp	360/N_poles	deg	22.5 deg
L_gap	0.75	mm	0.75 mm
gap_stator	L_gap+(Th_rotor/2)		4.25 mm
X_coil	0.6	mm	0.6 mm
y_coil	0.4	mm	0.4 mm

Name	Value	unit	Evaluated
OD_coil	OD_stator+X_coil		166.8 mm
ID_coil	ID_stator+y_coil		94.6 mm
OD_coil	OD_stator+X_coil		166.8 mm
ID_coil	ID_stator+y_coil		94.6 mm
Th_coil	30	mm	30 mm
A_copper	146	mm^2	146 mm^2
W_coil	4.78723931	mm	4.7 mm
L_coil	(A_copper/2)/W_coil*1e3	mm	15.2 mm
coil_correction	1.61	mm	1.61 mm
Hs2_coil	L_coil+coil_correction		16.8 mm
coil_angle	360/N_slots	deg	20 deg
N_conductor	10		10
OD_band	200	mm	200 mm
len_band	Th_rotor*1e3+1	mm	8 mm
dia_region	250	mm	250 mm
len_region	100	mm	100 mm
shaft_dia	38	mm	38 mm
shaft_th	7	mm	7 mm
Rwp	((OD_magnet-ID_magnet)/2+ID_magnet)/2		65.1 mm
rotor1_posZ	3.3	mm	3.3 mm
mac_height	gap_stator+Th_stator		34.25 mm
Cy_height	gap_stator+(Th_stator/2)		19.25 mm

Name	Value	unit	Evaluated
OMEGA_speed	500	rpm	500 rpm
OMEGA_rpm	500		500
EFreq	(OMEGA_rpm*N_poles)/120		66
I_s_amp	0	A	0 A
Theta_I	0	deg	0 deg
I_s_d	I_s_amp*cos(Theta_I)		0 A
I_s_q	I_s_amp*sin(Theta_I)		0 A
Omega_r	2*pi*EFreq		418.87
T_cycle	1/EFreq*1e3	ms	15 ms
N_step	120		120
N_cycle	2		2
T_stop	T_cycle*N_cycle*1e3	ms	30 ms

APPENDIX B

MATLAB code to calculate end turn leakage

```
na=1;Nc=12;Nq=6;rc=0.012;wc=0.006;wt=0.01071;hc=0.0152;lext=0.005;
lew_bend=0.006;KM=1.1;
Kp=1;A=rc;C=hc;
if (lext < 0.0025)
B=2*wc;
le=wt+2*wc+2*lext;
BETA=B/2/A;
K1=(2*BETA/pi)*(log(4/BETA)-0.5)+(BETA*BETA/8)*
(log(4/BETA)+(1/8))-...
(2*BETA/pi)*((BETA*BETA/64)*log(4/BETA)-(2/3))+
(5*BETA^6/1024)*(log(4/BETA)-...
(109/120))
kvot=B/C
if kvot<1
X=kvot;
Y=C/2/A;
F1=-0.0638*X^2 + 0.3298*X - 0.001973;
F2=-0.1165*X^2 + 0.03898*X - 0.3941;
```

```
F3=0.06118*X^2 - 0.03218*X + 0.001861;
F4=1.167*X^2 + 0.3721*X - 5.587;
K2= F1*exp(F2*Y) + F3*exp(F4*Y)
else
X=C/B;
Y=C/2/A;
F1=-0.2652*X*X+0.6943*X-0.01944;
F2= -8.246*EXP(-20.14*X)-0.2779*EXP(-0.3369*X);
F3=(-0.001548*X+0.0003029)/(X^4-2.211*X^3 + 1.1485*X^2- 0.2759*X +
0.01816);
F4=(-2.493*X^2 + 0.8325*X- 0.4384)/(X^3+ 0.03686*X^2 - 0.2928*X + 0.05966);
K2= F1*exp(F2*Y) + F3*exp(F4*Y)
end
Le2=(4*le/(2*pi*A))*(1.9739/na^2)*2*(A^2/B)*Nc^2*Nq*(K1-K2);
Le3=KM*Kp*Le2 %Leakage inductance in uH
else
B1=wc;
B2=2*wc;
le1=wc+2*lext;
le2=wt+wc;
BETA1=B1/2/A;
BETA2=B2/2/A;
K11=(2*BETA1/pi)*(log(4/BETA1)-0.5)+(BETA1*BETA1/8)*
(log(4/BETA1)+(1/8))-...
(2*BETA1/pi)*((BETA1*BETA1/64)*log(4/BETA1)-(2/3))+
(5*BETA1^6/1024)*(log(4/BETA1)-...
(109/120))
K12=(2*BETA2/pi)*(log(4/BETA2)-0.5)+(BETA2*BETA2/8)*
(log(4/BETA2)+(1/8))-...
(2*BETA2/pi)*((BETA2*BETA2/64)*log(4/BETA2)-(2/3))+
(5*BETA2^6/1024)*(log(4/BETA2)-...
(109/120))
kvot1=B1/C;
if kvot1<1
X=kvot1;
Y=C/2/A;
```

```
F1=-0.0638*X^2 + 0.3298*X - 0.001973;
F2=-0.1165*X^2 + 0.03898*X - 0.3941;
F3=0.06118*X^2 - 0.03218*X + 0.001861;
F4=1.167*X^2 + 0.3721*X - 5.587;
K21= F1*exp(F2*Y) + F3*exp(F4*Y)
else
X=C/B1;
Y=C/2/A;
F1=-0.2652*X*X+0.6943*X-0.01944;
F2= -8.246*exp(-20.14*X)-0.2779*exp(-0.3369*X);
F3=(-0.001548*X+0.0003029)/(X^4-2.211*X^3 + 1.1485*X^2- 0.2759*X +
0.01816);
F4=(-2.493*X^2 + 0.8325*X- 0.4384)/(X^3+ 0.03686*X^2 - 0.2928*X + 0.05966);
K21= F1*exp(F2*Y) + F3*exp(F4*Y)
end
kvot2=B2/C;
if kvot2<1
X=kvot2;
Y=C/2/A;
F1=-0.0638*X^2 + 0.3298*X - 0.001973;
F2=-0.1165*X^2 + 0.03898*X - 0.3941;
F3=0.06118*X^2 - 0.03218*X + 0.001861;
F4=1.167*X^2 + 0.3721*X - 5.587;
K22= F1*exp(F2*Y) + F3*exp(F4*Y)
else
X=C/B2;
Y=C/2/A;
F1=-0.2652*X*X+0.6943*X-0.01944;
F2= -8.246*exp(-20.14*X)-0.2779*exp(-0.3369*X);
F3=(-0.001548*X+0.0003029)/(X^4-2.211*X^3 + 1.1485*X^2- 0.2759*X +
0.01816);
F4=(-2.493*X^2 + 0.8325*X- 0.4384)/(X^3+ 0.03686*X^2 - 0.2928*X + 0.05966);
K22= F1*exp(F2*Y) + F3*exp(F4*Y)
end
Le1=(1.9739/na^2)*2*((0.5*le1)^2/B1)*Nc^2*Nq*(K11-K21);
Le2=(4*le2/(2*pi*A))*(1.9739/na^2)*2*(A^2/B2)*Nc^2*Nq*(K12-K22);
```

Le3=KM*Kp*(Le1+Le2) %Leakage inductance in uH

APPENDIX C

Core Material Data

Typical data for SURA® M235-35A

T	W/kg at 50 Hz	VA/kg at 50 Hz	A/m at 50 Hz	W/kg at 100 Hz	W/kg at 200 Hz	W/kg at 400 Hz	W/kg at 1000 Hz	W/kg at 2500 Hz
0,1	0,02	0,05	24,7	0,04	0,08	0,19	0,93	3,89
0,2	0,06	0,14	32,6	0,14	0,32	0,87	3,55	14,3
0,3	0,11	0,24	38,1	0,30	0,73	1,88	7,45	29,6
0,4	0,20	0,37	43,1	0,49	1,21	3,17	12,3	50,2
0,5	0,29	0,51	48,2	0,71	1,78	4,73	18,5	76,7
0,6	0,38	0,67	53,9	0,97	2,44	6,56	25,8	110
0,7	0,50	0,87	60,7	1,25	3,19	8,67	34,6	153
0,8	0,62	1,09	68,8	1,57	4,03	11,0	45,0	205
0,9	0,77	1,36	79,3	1,92	4,97	13,8	57,2	270
1,0	0,92	1,71	93,7	2,31	6,01	16,9	71,5	349
1,1	1,10	2,17	115	2,75	7,19	20,3	88,3	
1,2	1,31	2,89	156	3,26	8,54	24,3		
1,3	1,56	4,45	260	3,88	10,1	28,9		
1,4	1,92	10,3	690	4,67	12,2	34,8		
1,5	2,25	32,4	1950	5,54	14,4	41,2		
1,6	2,53	84,6	4410					
1,7	2,75	162	7630					
1,8	2,94	274	12000					

Figure C.1

SURA® Grade	Thickness	Max specific total loss at 50 Hz		Minimum magnetic polarization at 50 Hz			Conventional density
		$\hat{J}$ =1,5 T	1,0T*	$\hat{H}$=2500	5000	10000 A/m	
	mm	W/kg	W/kg	T	T	T	kg/dm³
M210-27A	0,27	2,10	0,85	1,49	1,60	1,70	7,60
M235-35A	0,35	2,35	0,95	1,49	1,60	1,70	7,60
M250-35A	0,35	2,50	1,00	1,49	1,60	1,70	7,60
M270-35A	0,35	2,70	1,10	1,49	1,60	1,70	7,65
M300-35A	0,35	3,00	1,20	1,49	1,60	1,70	7,65
M330-35A	0,35	3,30	1,30	1,49	1,60	1,70	7,65
M250-50A	0,50	2,50	1,05	1,49	1,60	1,70	7,60
M270-50A	0,50	2,70	1,10	1,49	1,60	1,70	7,60
M290-50A	0,50	2,90	1,15	1,49	1,60	1,70	7,60
M310-50A	0,50	3,10	1,25	1,49	1,60	1,70	7,65
M330-50A	0,50	3,30	1,35	1,49	1,60	1,70	7,65
M350-50A	0,50	3,50	1,50	1,50	1,60	1,70	7,65
M400-50A	0,50	4,00	1,70	1,53	1,63	1,73	7,70
M470-50A	0,50	4,70	2,00	1,54	1,64	1,74	7,70
M530-50A	0,50	5,30	2,30	1,56	1,65	1,75	7,70
M530-50HP	0,50	5,30	2,30	1,63	1,71	1,81	7,80
M600-50A	0,50	6,00	2,60	1,57	1,66	1,76	7,75
M700-50A	0,50	7,00	3,00	1,60	1,69	1,77	7,80
M800-50A	0,50	8,00	3,60	1,60	1,70	1,78	7,80
M310-65A	0,65	3,10	1,25	1,49	1,60	1,70	7,60
M330-65A	0,65	3,30	1,35	1,49	1,60	1,70	7,60
M350-65A	0,65	3,50	1,50	1,49	1,60	1,70	7,60
M400-65A	0,65	4,00	1,70	1,52	1,62	1,72	7,65
M470-65A	0,65	4,70	2,00	1,53	1,63	1,73	7,65
M530-65A	0,65	5,30	2,30	1,54	1,64	1,74	7,70
M600-65A	0,65	6,00	2,60	1,56	1,66	1,76	7,75
M600-65HP	0,65	6,00	2,60	1,63	1,72	1,82	7,80
M700-65A	0,65	7,00	3,00	1,57	1,67	1,76	7,75
M800-65A	0,65	8,00	3,60	1,60	1,70	1,78	7,80
M600-100A	1,00	6,00	2,60	1,53	1,63	1,72	7,60
M700-100A	1,00	7,00	3,00	1,54	1,64	1,73	7,65
M800-100A	1,00	8,00	3,60	1,56	1,66	1,75	7,70
M1000-100A	1,00	10,00	4,40	1,58	1,68	1,76	7,80

Figure C.2

APPENDIX D

Parameterization of Coordinates in the 2D model

The model geometry of the 2D model is generated by parameterizing the x and y points in the xy coordinate system. The points are as shown in Figure D.1 with $Stpoint = 0$

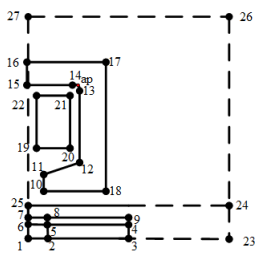

Figure D.1: Coordinate points in the 2D model

Rotor and Magnets

Point 1:

$$x_1 = Stpoint;\ y_1 = Stpoint \tag{D.1}$$

Point 2:

$$x_2 = \frac{W_{core}}{2};\ y_2 = Stpoint \tag{D.2}$$

Point 3:

$$x_3 = x_2 + \left(\frac{W_{magnet}}{2}\right);\ y_3 = Stpoint \tag{D.3}$$

Point 4:

$$x_4 = x_3;\ y_4 = Th_{magnet} - Th_{magnet,layer} \tag{D.4}$$

Point 5:

$$x_5 = x_2;\ y_5 = y_4 \tag{D.5}$$

Point 6:

$$x_6 = Stpoint;\ y_6 = y_5 \tag{D.6}$$

Point 7:

$$x_7 = Stpoint;\ y_7 = Th_{magnet} \tag{D.7}$$

Point 8:

$$x_8 = x_2;\ y_8 = y_7 \tag{D.8}$$

Point 9:

$$x_9 = x_4;\ y_9 = y_7 \tag{D.9}$$

Stator

Point 10:

$$x_{10} = \frac{W_{slotop}}{2};\ y_{10} = Th_{magnet} + l_{gap} \tag{D.10}$$

Point 11:

$$x_{11} = x_{10};\ y_{11} = y_{10} + Hs0 \tag{D.11}$$

Point 12:

$$x_{12} = \frac{W_{slot}}{2};\ y_{12} = y_{11} + Hs1 \tag{D.12}$$

Point 13:

$$x_{13} = x_{12};\ y_{13} = y_{12} + Hs2 \tag{D.13}$$

Point ap:

$$ap_x = R_s \cdot \cos 45;\ ap_y = R_s \cdot \sin 45 \tag{D.14}$$

$$x_{ap} = x_{13} - ap_x;\ y_{ap} = y_{13} + ap_y \tag{D.15}$$

Point 14:

$$x_{14} = x_{13} - R_s;\ y_{14} = y_{13} + R_s \tag{D.16}$$

Point 15:

$$x_{15} = Stpoint;\ y_{15} = y_{14} \tag{D.17}$$

Point 16:

$$x_{16} = Stpoint;\ y_{16} = H_z \tag{D.18}$$

Point 17:

$$x_{17} = \left(\frac{W_{slot}}{2}\right) + \left(\frac{W_{tooth}}{2}\right);\ y_{17} = y_{16} \tag{D.19}$$

Point 18:

$$x_{18} = x_{17};\ y_{18} = y_{10} \tag{D.20}$$

Coils

Point 19:

$$x_{19} = \left(\frac{W_{halfslot} - W_{coil}}{2}\right);\ y_{19} = y_{12} + \left(\frac{HS2 - L_{coil}}{2}\right) \tag{D.21}$$

Point 20:

$$x_{20} = x_{19} + W_{coil};\ y_{20} = y_{19} \tag{D.22}$$

Point 21:

$$x_{21} = x_{20};\ y_{21} = y_{20} + L_{coil} \tag{D.23}$$

Point 22:

$$x_{22} = x_{19};\ y_{22} = y_{21} \tag{D.24}$$

Band

Point 23:

$$x_{23} = W_{2D};\ y_{23} = Stpoint \tag{D.25}$$

Point 24:

$$x_{24} = x_{23};\ y_{24} = y_9 + 0.5 \tag{D.26}$$

Point 25:

$$x_{25} = Stpoint;\ y_{25} = y_{24} \tag{D.27}$$

Region

Point 26:

$$x_{26} = x_{24};\ y_{26} = Th_{stator} + 20 \tag{D.28}$$

Point 27:

$$x_{27} = Stpoint;\ y_{27} = y_{26} \tag{D.29}$$

APPENDIX E

Coordinates for creating stator slot in the 3D model

In the YZ plane, the coordinates of the stator slot can be parameterized for each point in the xyz coordinates as shown in Figure E.1. The corresponding equations for each point are,

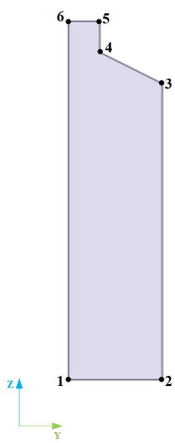

Figure E.1: Coordinates of the slots in x, y and z direction

$$x_1 = 0;\ y_1 = 0;\ z_1 = d_{sy} \tag{E.1}$$

$$x_2 = 0;\ y_2 = \frac{W_{ss}}{2};\ z_2 = d_{sy} \tag{E.2}$$

$$x_3 = 0;\ y_3 = \frac{W_{ss}}{2};\ z_3 = d_{sy} + d_{ss} - Hs1 \tag{E.3}$$

$$x_4 = 0;\ y_4 = \frac{bs0}{2};\ z_4 = d_{sy} + d_{ss} - Hs0 \tag{E.4}$$

$$x_5 = 0;\ y_5 = \frac{bs0}{2};\ z_5 = d_{sy} + d_{ss} + Hs0 + Z_{adj} \tag{E.5}$$

$$x_6 = 0;\ y_6 = 0;\ z_6 = d_{sy} + d_{ss} + Hs0 + Z_{adj} \tag{E.6}$$

In (E.5) and (E.6) an additional length Z_{agj} is added, to ensure proper intersection, which facilitates accurate meshing in the model.

References

[1] J. Edmondson, D. Wyatt, and L. Gear, "Electric motors for electric vehicles 2022–2032 (sample pages)," *IDTechEx, Cambridge, UK, Tech. Rep*, 2022.

[2] F. G. Capponi, G. De Donato, and F. Caricchi, "Recent advances in axial-flux permanent-magnet machine technology," *IEEE Transactions on Industry Applications*, vol. 48, no. 6, pp. 2190–2205, 2012.

[3] C. Jenkins, S. Jones-Jackson, I. Zaher, *et al.*, "Innovations in axial flux permanent magnet motor thermal management for high power density applications," *IEEE Transactions on Transportation Electrification*, vol. 9, no. 3, pp. 4380–4405, 2023.

[4] A. Nakahara, K. Deguchi, S. Kikuchi, and Y. Enomoto, "Comparative electrical design of radial-and axial-flux permanent magnet synchronous machines under space limitation," in *2014 International Conference on Electrical Machines (ICEM)*, IEEE, 2014, pp. 422–428.

[5] V. Rallabandi, O. A. Badewa, B. Ozpineci, and D. M. Ionel, "A comparison of outer rotor radial and axial flux machines for application in electric vehicles," in *2023 IEEE International Electric Machines & Drives Conference (IEMDC)*, IEEE, 2023, pp. 1–5.

[6] D. Slutskiy, S. Basnet, *et al.*, "Comparison of axial and radial flux permanent magnet machines," in *2022 North American Power Symposium (NAPS)*, IEEE, 2022, pp. 1–6.

[7] L. Jiaxin, Z. Chengming, F. Pengrui, M. Yiguang, and Z. Xintong, "A performance comparison of radial flux spm machine and yasa machine," in *2024 IEEE 7th International Electrical and Energy Conference (CIEEC)*, IEEE, 2024, pp. 3264–3269.

[8] R. Tsunata, K. Izumiya, M. Takemoto, J. Imai, T. Saito, and T. Ueno, "Designing and prototyping an axial-flux machine using ferrite pm and round wire for traction applications: Comparison with a radial-flux machine using nd-fe-b pm and rectangular wire," *IEEE Transactions on Industry Applications*, 2024.

[9] M. Gulec and M. Aydin, "Implementation of different 2d finite element modelling approaches in axial flux permanent magnet disc machines," *IET Electric Power Applications*, vol. 12, no. 2, pp. 195–202, 2018.

[10] V. Sankarraman, S. Khalesidoost, D. Talebi, S. M. Seyedi, and M. Gardner, "Scaling an axial flux permanent magnet motor for different electrified aviation applications," in *2023 IEEE Energy Conversion Congress and Exposition (ECCE)*, IEEE, 2023, pp. 1787–1793.

[11] M. Alatalo, *On Finding Optimal Machines and Comparison of Axial and Radial Flux Propulsion Machines*. Chalmers University of Technology. Institutionen för elektroteknik, 2021.

[12] F. Nishanth, J. Van Verdeghem, and E. L. Severson, "A review of axial flux permanent magnet machine technology," *IEEE Transactions on Industry Applications*, vol. 59, no. 4, pp. 3920–3933, 2023.

[13] A. Selema, M. N. Ibrahim, H. Vansompel, and P. Sergeant, "Development of yokeless axial flux machine using 3d-printed shape-profiled core," in *2022 International Conference on Electrical Machines (ICEM)*, IEEE, 2022, pp. 1763–1769.

[14] F. Nishanth, A. D. Goodall, I. Todd, and E. L. Severson, "Characterization of an axial flux machine with an additively manufactured stator," *IEEE Transactions on Energy Conversion*, vol. 38, no. 4, pp. 2717–2729, 2023.

[15] D. Mezher, "Modeling an axial flux machine," M.S. thesis, Chalmers University of Technology. Electrical Engineering, 2021.

[16] SURA-M235-35A. “Material data for sura m235-35a steel.” Accessed:Dec 2024. (), [Online]. Available: https://e-magnetica.pl/database-em/01_Soft/Electrical_steels/Cogent_Newport_2003/NO-11.pdf.

[17] S. T. Lundmark, T. Thiringer, and E. A. Grunditz, “Traction motor 2d models with end winding leakage inductance consideration,” in *2024 International Conference on Electrical Machines (ICEM)*, IEEE, 2024, pp. 1–7.

[18] F. Sahin, “Design and development of a high-speed axial-flux permanent-magnet machine,” Ph.D. dissertation, Technische Universiteit Eindhoven, Electrical Engineering, 2001.

[19] J. H. Potgieter and M. J. Kamper, “Calculation methods and effects of end-winding inductance and permanent-magnet end flux on performance prediction of nonoverlap winding permanent-magnet machines,” *IEEE Transactions on Industry Applications*, vol. 50, no. 4, pp. 2458–2466, 2013.